1-1-2002

Studies of the physical, yield and failure behavior of aliphatic polyketones.

Nicole Renee Karttunen
University of Massachusetts Amherst

STUDIES OF THE PHYSICAL, YIELD AND FAILURE BEHAVIOR OF ALIPHATIC POLYKETONES

A Dissertation Presented

by

NICOLE RENEE KARTTUNEN

Submitted to the Graduate School of the
University of Massachusetts in partial fulfillment
of the requirements for the degree of

DOCTOR OF PHILOSOPHY

February 2002

Department of Polymer Science and Engineering

STUDIES OF THE PHYSICAL, YIELD AND FAILURE BEHAVIOR OF ALIPHATIC POLYKETONES

A Dissertation Presented

by

NICOLE RENEE KARTTUNEN

Approved as to style and content by:

Alan J. Lesser, Chair

Richard J. Farris, Member

H. Henning Winter, Member

Thomas J. McCarthy, Department Head

Polymer Science and Engineering

DEDICATION

To my parents and to Jeremy

ACKNOWLEDGEMENTS

I can honestly say that this degree does not belong to solely to me. It also belongs to those whose help and support throughout my life have made it possible for me to accomplish this achievement. Of course, this would not have been possible without the wonderful guidance of my thesis advisor, Professor Alan J. Lesser. He has been an outstanding advisor in every sense. In every aspect of my graduate career- from coursework to research and job search- he has played an invaluable role. I thank him for this.

I also owe thanks to my thesis committee members, Professors Richard J. Farris and H. Henning Winter. I sincerely appreciate their advice and help with my graduate career. And to the other PSE Department faculty and staff who have taught and assisted me throughout my stay here at UMass, you have made my stay at UMass and the exceptional and I am a better person for it.

During my five years at UMass, I have had the pleasure of working with many wonderful graduate students in the Lesser Research Group as well as other groups. They have been not only my co-workers, but also my friends.

Of course, my family deserves much recognition. My parents, Doug and Sally, and my siblings, Heather and Craig, have always been there for me. Without the support of my family, I would not be where I am today.

And finally, to my fiancé Jeremy Cerasoli: Thank you for you for being my foundation throughout the past five years. You were my support when I doubted myself.

When I needed help or encouragement, you were there for me. I could not have made it without you.

ABSTRACT

STUDIES OF THE PHYSICAL, YIELD AND FAILURE BEHAVIOR OF ALIPHATIC POLYKETONES

FEBRUARY 2002

NICOLE RENEE KARTTUNEN, B.S., MICHIGAN TECHNOLOGICAL UNIVERSITY

M.S., UNIVERSITY OF MASSACHUSETTS AMHERST

PH.D., UNIVERSITY OF MASSACHUSETTS AMHERST

Directed by: Professor Alan J. Lesser

This thesis describes an investigation into the multiaxial yield and failure behavior of an aliphatic polyketone terpolymer. The behavior is studied as a function of: stress state, strain rate, temperature, and sample processing conditions. Results of this work include: elucidation of the behavior of a recently commercialized polymer, increased understanding of the effects listed above, insight into the effects of processing conditions on the morphology of the polyketone, and a description of yield strength of this materials as a function of stress state, temperature, and strain rate.

The first portion of work focuses on the behavior of a set of samples that are extruded under "common" processing conditions. Following this reference set of tests, the effect of testing this material at different temperatures is studied. A total of four different temperatures are examined. In addition, the effect of altering strain rate is examined. Testing is performed under pseudo-strain rate control at constant nominal

octahedral shear strain rate for each failure envelope. A total of three different rates are studied.

An extension of the first portion of work involves modeling the yield envelope. This is done by combining two approaches: continuum level and molecular level. The use of both methods allows the description of the yield envelope as a function of stress state, strain rate and temperature.

The second portion of work involves the effects of processing conditions. For this work, additional samples are extruded with different shear and thermal histories than the "standard" material. One set of samples is processed with shear rates higher and lower than the standard. A second set is processed at higher and lower cooling rates than the standard.

In order to understand the structural cause for changes in behavior with processing conditions, morphological characterization is performed on these samples. In particular, the effect on spherulitic structure is important. Residual stresses are also determined to be important to the behavior of the samples.

Finally, an investigation into the crystalline structure of a family of aliphatic polyketones is performed. The effects of side group concentration and size are described.

TABLE OF CONTENTS

LIST OF TABLES

LIST OF FIGURES

CHAPTER 1

INTRODUCTION

1.1 Biaxial Testing

1.1.1 Rationale

The uniaxial tensile behavior of many polymers has been well characterized. This simple type of testing is important and practical for comparing polymeric materials, but it cannot be extended to predict how a material will behave in multi-axial stress states. Since many applications do involve multiaxial stress states, it is especially important to investigate material behavior under these conditions as well. Pressure vessels, paints and coatings, composites, structural pieces, etc. are all applications that can benefit from studies of complex loading of polymeric materials. Unfortunately, relatively few studies to date have looked into this subject matter. In order to have a more complete characterization, it is also important to consider the effects of strain rate and temperature. These variables have significant influence on the yield behavior as well, and can be a significant factor in the behavior of a polymer during use.

Not only are the conditions during use of importance, but also the conditions during processing. Polymers today are utilized in a wide range of products. In the manufacturing of these products, various processing conditions may be used. As an example, parameters such as temperature or shear rate used for processing a given polymer may need to be altered in order to manufacturer a different part using that same

material. The effects of altering these conditions can be significant in terms of mechanical properties, barrier properties, etc., as a result of changes in the material structure. It is therefore quite relevant to consider these effects when examining the behavior of polymeric materials.

This thesis begins with an investigation into the multi-axial behavior of hollow cylindrical specimens of a new aliphatic polyketone terpolymer that are processed under a standard set of extrusion conditions. The investigation continues by examining the effects of test temperature and strain rate on the behavior of the terpolymer. Two existing approaches- continuum and thermal activation- are then combined in order to model the yield strength as a function of stress state, strain rate and temperature.

The thesis proceeds with an examination of the effect of processing conditions on the behavior of the aliphatic polyketone. In this portion of work, two samples are extruded with different shear rates and two samples are extruded with different cooling rates. The effects of the processing conditions on the behavior are then compared with effects on the morphology of the material. Specifically, residual stresses, crystallinity, orientation, crystallite size, thermal behavior and spherulitic structure are characterized.

Finally, as an extension of the aforementioned morphological studies, results from work dealing with a family of aliphatic polyketones are presented. In this case, samples with varied chemical compositions are characterized and compared. Morphological details such as crystal structure, crystallinity, lamellar thickness, etc. are presented as a function of side group concentration and size.

1.1.2 Methods of Biaxial Testing

There are a variety of methods that have been used for testing materials in complex stress states. As a means of introduction, a few of the more common methods and their limitations will briefly be discussed here.

One method of biaxially testing a material is the so-called "blister" testing of films. In this method, a film is sealed against a flat surface with a fluid inlet allowing the flow of gas or liquid between the flat surface and the film. This creates a "blister" and the stresses can be calculated from the measured fluid pressure and sample geometry. This method is limited by the geometry of the grip template as to the stress states that can be applied. A separate template is required for each stress state. Testing is also limited to stress states that are tensile in both principal directions. Early work in this type of stressing is discussed by Hopkins[1]. In this study, nitrogen gas is used to biaxially load compression-molded polyethylene (PE) films. Results indicate that the complex stressing can significantly affect the material behavior. For example, it is found that PE that fails at 300-500% strain in uniaxial tension fails at only 30% strain under biaxial tension. In addition, the latter failure is brittle in nature. In the case of a different PE with higher molecular weight, a film loaded in uniaxial tension is able to draw to ~600% strain before failing. However, this material reaches only ~200% strain before failing under biaxial loading conditions. Clearly, the state of stress affects the behavior of the films in this study.

Others[2,3] report the results of blister testing performed on nylon. Biaxial test results are compared to previous results of nylon fibers under uniaxial loading

conditions. The results indicate that while the yield stress under both uniaxial and equibiaxial conditions are the same, the post yield behavior is different for the two different loading conditions. The stress following yield decreases for the biaxially loaded films, indicating some sort of strain softening, but remains constant for the case of uniaxial loading.

More recent work with this type of loading is reported for linear low density poly(ethylene) (LLDPE) films[4]. This study focuses on the deformation behavior and neck formation within uniaxially and biaxially loaded films. The deformation behavior is found to relate to the direction of maximum principal loading and its relation to the machine direction (direction of slight orientation) of the blown films.

A second method for biaxial testing involves testing "cruciform" specimens[5,6]. In this method loads are applied to four "arms", which are usually thicker in cross-section than the center gauge region. A similar method is biaxial stretching on a "tenter frame" apparatus. These methods allow a range of stress states within the tensile-tensile quadrant to be interrogated. However, stress states involving compressive loading are not tested with this method. Due to the procedural difficulties associated with this method, published results are not common.

Another biaxial testing method involves the internal pressurization of hollow cylindrical specimens. The pressurization results in a state of biaxial tension. With the superposition of an axial load, a wide range of stress states can be applied to the specimens. The stress states attained with this type of loading must be tensile in the circumferential direction, but may be either tensile or compressive in the axial direction.

Any stress state within this range may be applied to a sample without geometric constraints. This is the method utilized in this work. Previous work with this type of testing system has been performed by a few others[7-14] and these are described in more detail in the following sections (1.1.3-1.1.5). The purpose of this is to acquaint the reader with various procedural details and important observations resulting from these studies. This review also serves to distinguish the present research from previous studies.

1.1.3 Hollow Cylinder Testing of Glassy Polymers

Many studies that have investigated the multiaxial yield behavior of polymers have focused on glassy polymers. A well-known study of poly(methyl methacrylate) (PMMA) is that of Sternstein and Ongchin[8]. In this work, samples are machined from cast PMMA hollow cylinders. The study focuses on crazing and shear yielding in the material and a variety of stress states in the tensile-tensile quadrant are examined for both portions. The results indicate that the yield behavior follows a modified von Mises type of criterion, and therefore the pressure dependence of the yield strength. In this study of glassy PMMA only one set of test conditions (temperature and strain rate) is investigated.

Another investigation is that of Carapellucci and Yee[9] on the yielding of slightly anisotropic polycarbonate cylinders. Specimens are loaded axially and silicone oil is used to pressurize the cylinders internally. The study does not include the effect of test rate, but does consider two different test temperatures and different degrees of anisotropy. Results show that the level of plastic flow varies with applied stress state.

More recent reports by Kody and Lesser[10,11] describe isotropic epoxy systems, elucidating the effects of strain rate, temperature, as well as molecular architecture on the yield and fracture behavior. In their work, hollow cylinders are loaded axially in either tension or compression and nitrogen gas is used for pressurization. Again, pressure dependence of yield strength is observed. The stress state is found to influence the yield strength and the failure mode.

1.1.4 Hollow Cylinder Testing of Thermoplastic Polymers

Only a few studies consider thermoplastic materials under complex loading conditions[12,13, 14]. One of these[12] describes the deformation behavior of nylon-6 and amorphous PMMA under uniaxial and biaxial loading. Samples are cut and machined from commercially available tubes and are tested in tension, torsion, simultaneous tension and torsion, tension followed by torsion, or torsion followed by tension. Water is used as the pressurizing fluid. It is found that failure mode is dependent upon the stress. In addition, the generalized stress at failure is found to be insensitive to the loading path (e.g., tension followed by torsion or torsion followed by tension). No effects of temperature or loading rate are included in the study and only a limited number of stress states are examined.

Another study[13] describes the elastic and yield behavior of slightly anisotropic polyethylene. Extruded tubes are tested at room temperature under a constant octahedral shear stress rate of 1.78 MPa/min along all loading paths. In this case, air is used as the pressurizing fluid. Yield is defined as the 0.3% offset in the octahedral shear stress versus octahedral shear strain curve. Effects of temperature, test rate and degree of

orientation are not considered. In addition, only stress states in the tensile-tensile quadrant are considered. Because the reported results focus on the yield response, it is not clear if samples are tested until failure. No mention of failure modes of the samples is made.

Another study[14] focuses on the yield behavior of highly oriented polypropylene tubes in which different degrees of orientation are produced by die drawing prior to testing. Testing is performed under maximum principal strain rate control at room temperature. Strain rates are between 120 and 200 s^{-1} and the yield point is defined as the 0.5% offset in the equivalent stress versus equivalent strain curve. While different levels of orientation are included in the study, effects of temperature or test rate are not considered. Again, only stress states that are tensile in both principal directions are investigated and no mention is made of failure mode as a function of stress state.

1.1.5 Distinction from Previous Studies

While the works cited above all involve biaxial testing, there are clearly variations in procedure, focus, etc. The scope of this theses work is distinct from the aforementioned studies. Samples are brought to failure as opposed to a specified yield point. The present work also includes various temperature, strain rate and processing conditions. Some of the previous studies have been conducted on either isotropic or highly oriented specimens. Because processing techniques such as extrusion, injection molding, etc., typically induce a small degree of orientation it is appropriate to study mildly anisotropic materials. The present investigation is performed on extruded pipe, as received from the resin supplier. A wide range of stress states can be applied to

specimens of the same geometry by controlling the ratio between the axial load and internal pressure, avoiding the need for a variety of geometries to look at a variety of stress states. Moreover, by maintaining a constant nominal octahedral shear strain rate for all stress states within a failure envelope, the rate effects between envelopes can be compared.

To summarize, slightly anisotropic thermoplastic hollow cylinders under a wide range of biaxial loading conditions are investigated. The effects of both temperature and strain rate during testing are determined. Finally, the effects of cooling rate and shear rate during processing are studied. These testing and processing variables are described in more detail in their respective chapters.

1.2 Aliphatic Polyketones

1.2.1 Rationale

Engineering thermoplastics are being used at an increasing rate in a variety of products. This fact in itself makes the full characterization of such materials significant. This research provides the opportunity to look more closely at the properties and behavior of not only an engineering thermoplastic, but also one that is commercially new, giving added interest to the work. Prior to this study, only basic uniaxial tensile tests and limited fracture toughness results have been reported for aliphatic polyketones[15-17]. With this research the behavior of this type of engineering polymer subjected to biaxial loading conditions is elucidated. A new method for describing the yield strength as a function of stress state, temperature and strain rate is described. Other mechanical properties and the morphology of this material are also characterized. Finally, the effect of molecular architecture, particularly side group size and concentration, on the crystalline morphology of the material is examined.

1.2.2 Material Information

Aliphatic polyketones are a family of polymers that have recently become commercially available[15]. This class of polymers has characteristics that make it an attractive material for engineering and commodity applications. It has strength comparable to engineering polymeric materials[18,19] such as Nylon 6.6 (PA 6.6), polycarbonate (PC), polyethylene terepthalate (PET) and polyoxymethylene (POM) and

stiffness similar to PA 6.6, PA 12[20] and acrylonitrile-butadiene-styrene (ABS)[16,19]. It has very good chemical resistance, and is particularly resistant to fuels[16,17,19,21,22]. Water absorption is low[16,17,19,21-24], and barrier properties are quite good[16]. Tribologically, it has been shown to have improved properties over nylon and polyacetal[20].

While aliphatic polyketones have become available commercially within the last five years or so, they have been in development for several decades. In the early stages of development, aliphatic polyketones consisted of random units of carbonyl and ethyl groups[25]. Beginning in the 1980's new catalysts were used in the synthesis of these polymers[26-29]. The catalysts resulted in the perfect alternation of carbonyl and ethyl units. These polymers were difficult to process because the melt temperature and degradation temperature were relatively close together, however, it was found that polymerization with small amounts of propylene could reduce the melt temperature while leaving the degradation temperature unaffected. Thus, the window of processability for the polymer was improved. Synthesis with other olefins such as butylene was found to produce similar effects. The general formula for this class of polymers is shown in Figure 1.1. R groups are typically ethyl, propyl or butyl groups (CH_2CH_2, CH_2CHCH_3 or $CH_2CHCH_2CH_3$)[30]. With R= ethyl, the material is termed a copolymer. With R=propyl or butyl, the material is termed a terpolymer. The synthesis of this polymer has the benefit of using cheap and abundant raw materials (carbon monoxide, ethylene and possibly propylene or butylene) and high yield under moderate temperature and pressure conditions.

The polymer that is utilized in the multi-axial testing study is Carilon® aliphatic polyketone. This is the grade that was made commercially available by Shell Chemical Company in 1996. The chemical formula is the same as in Figure 1.1 with R= CH_2CHCH_3 and m:n is 14:1.

For analysis on the effect of chemical composition, films produced under the trademark Ketonex® are utilized. The chemical formula is the same as described in Figure 1.1, with R groups being one of the following: CH_2CH_2, CH_2CHCH_3 or $CH_2CHCH_2CH_3$. Within this family of polymers, the concentrations of these groups are also varied. Details are listed in Table 1.1 and in Chapter 6.

R group	Substitution Level (Mol%)	T_m (°C)	Molding Temperature (°C)
CH_2CH_2	100	252	255
CH_2CHCH_3	2.0	248	270
CH_2CHCH_3	6.6	223	245
CH_2CHCH_3	8.8	215	230
CH_2CHCH_3	10.0	209	230
CH_2CHCH_3	14.6	198	220
$CH_2CHCH_2CH_3$	4.4	229	250
$CH_2CHCH_2CH_3$	5.8	225	245
$CH_2CHCH_2CH_3$	7.6	214	230
$CH_2CHCH_2CH_3$	10.0	210	230
$CH_2CHCH_2CH_3$	12.0	203	220

Table 1.1: Compositions of aliphatic polyketones studied as films.

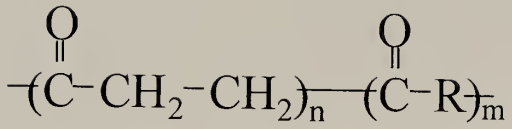

Figure 1.1: Chemical structure of aliphatic polyketones. R group may be ethyl, propyl or butyl (CH_2CH_2, CH_2CHCH_3 or $CH_2CHCH_2CH_3$, respectively).

CHAPTER 2

EFFECT OF STRESS STATE ON FAILURE MODE

2.1 Background

Various studies have considered the importance of state of stress on the failure behavior of materials. Several of these are described in Chapter 1. Here, results pertaining specifically the effect of stress state on failure mode are reviewed. In Hopkins'[1] study on polyethylene film, it is found that uniaxial stressing results in ductile behavior, while biaxial stretching results in brittle behavior. In another study[9] on the biaxial loading of polycarbonate hollow cylinders, it is found that all of the specimens fail in a ductile manner except one that had been tested under condition in which the axial stress is 1.7 times that of the circumferential stress. While the brittle behavior is attributed to excessive aging during thermal treatment, no explanation is given as to why the other specimens are not affected in a similar fashion. Another study[10] finds that the ductile to brittle transition at constant temperature is a function of the mean stress and is therefore is dependent upon the state of stress. More recent work[4] has been performed on polymer films loaded biaxially. While samples in this study are not brought to failure, it is determined that the deformation behavior is dependent upon the relation between the directions of maximum principal stress and film orientation. If the two directions are coincident, then homogeneous deformation occurs. If the directions do not

coincide, heterogeneous deformation is observed. From results such as these, it is clear that the stress state applied to a material has an effect on the way that material behaves. This matter is therefore one of interest in this thesis.

2.2 Material and Sample Preparation

The material tested is a semi-crystalline aliphatic polyketone terpolymer. Shell Chemical Company has recently introduced this engineering thermoplastic under the trademark Carilon®. The structure of the polymer consists of perfectly alternating units of carbon monoxide and ethylene, with a small proportion of the ethylene units substituted with propylene units (approximately 6 mol %). Thus, the structure is as shown in Figure 1.1 with R=CH_2CHCH_3 and m:n of 14:1. All hollow cylinder testing described in this thesis is performed on material of this composition.

The material examined in this portion of work is denoted as the "MSMC" material (moderate shear rate, moderate cooling rate) since it is processed under these general types of conditions. Unfortunately, specific details on the processing conditions cannot be made due to proprietary reasons.

Samples of the polyketone material are received in the form of extruded hollow cylinders from the manufacturer. The approximate dimensions for the cylinders are: external diameter of 22 mm and wall thickness of 1.9 mm. These dimensions allow thin-walled hollow cylinder theory to be utilized (thickness less than 8 times the diameter[31]), simplifying the analysis. Test specimens are cut at 15 cm lengths from the received material. This length has been calculated to be sufficient to neglect gripping

effects in the center region of the cylinders during testing. The calculation procedure is described in a separate paper by Bekhet et al.[32].

The specimen gripping system designed for the samples is shown in Figure 2.1. For each specimen, metal inserts are placed into the ends of a hollow cylinder, and compression fittings placed around the cylinder. The fitting "seals" the specimen for pressurization. At each end the specimen is secured to a pipe fitting, which is then threaded into steel cylinders. The steel cylinders are clamped into grips attached to a tension-torsion machine. The upper steel cylinder is tapped to allow internal pressurization of the specimens. Nylon cord is inserted into the hollow cylinders to reduce the compressible volume.

In addition to the hollow cylindrical samples, standard ASTM D-638[33] dog-bone samples are utilized for preliminary characterization. These samples are injection molded bars and are used as received from the manufacturer, without additional treatment or conditioning.

2.3 Experimental

2.3.1 Preliminary Uniaxial Testing

Preliminary tensile testing is performed on injection molded bars. This is performed in accordance with ASTM standards[33] in an Instron 1123 tensile testing machine. Extensometers are attached to samples in order to measure the strain. Crosshead speed controls the nominal strain rate. This testing is performed in order to

obtain values for tensile modulus and Poisson's ratio as well as for comparison with data from hollow cylinder uniaxial testing data.

2.3.2 Biaxial Testing Procedure

All testing on hollow cylinders is performed under pseudo strain rate control. It is desired to keep the nominal octahedral shear strain rate, $\dot{\gamma}^{oct}$, constant for all stress states. This provides the consistency necessary to evaluate strain rate effects for the studies on the different stress states. The method for calculating this value is described in section 2.3.3, equation 2.12. Testing is carried out in an Instron 1321 tension-torsion machine that has been modified for the biaxial testing described here, Figure 2.2. The grips used during testing have been designed to ensure alignment of the sample during testing. Nitrogen gas is used as the pressurizing fluid. A Tescom ER3000 pressure regulator is utilized to control the internal pressure of the specimens during testing. Both the regulator and the tension-torsion machine are controlled externally with a personal computer and programming written with LabVIEW software. The test program allows the operator to specify a stress state, which is held constant throughout the test procedure as the sample is loaded until failure. The program also allows for independent control of the shear strain rate during testing. In addition, the sample is enclosed within a chamber designed around the test equipment. This chamber not only provides a safety barrier, it also allows the operator to control the temperature at which testing is performed. This aspect is described in more detail in Chapter 3.3.2.

To summarize, the testing apparatus allows for testing under a range of stress states, from axial compression to biaxial tension, utilizing a single specimen geometry.

The testing apparatus and programming also allow the operator to have independent control of stress state, strain rate and temperature during the testing procedure. Again, all testing is performed under pseudo strain rate control with a constant nominal octahedral shear strain rate. The theory behind this testing method is described in the following paragraphs.

When a thin walled hollow cylinder is subjected to an internal pressure, p, and an axial load, Q, the following stresses are produced in the axial and circumferential directions:

$$\sigma_z = \frac{Q}{\pi Dt} + \frac{pD}{4t} \tag{2.1}$$

$$\sigma_\theta = \frac{pD}{2t} \tag{2.2}$$

Where σ_z and σ_θ are the principal stresses in the axial and circumferential directions, D is the mean diameter and t is the cylinder thickness. Radial stresses are considered negligible. In the absence of applied torsion, the octahedral shear stress, τ^{oct}, and hydrostatic stress, σ_m, can therefore be written as follows:

$$\tau^{oct} = \frac{1}{3}\sqrt{(\sigma_z - \sigma_\theta)^2 + (\sigma_z)^2 + (\sigma_\theta)^2} \tag{2.3}$$

$$\sigma_m = \frac{1}{3}(\sigma_z + \sigma_\theta) \tag{2.4}$$

The principal strain values may also be determined. As it is reasonable to expect an extruded pipe to display transverse isotropy, this case will be considered. In cylindrical coordinates, Hooke's law for a transversely isotropic material, neglecting shear terms, may be written as:

$$\begin{Bmatrix} \sigma_r \\ \sigma_\theta \\ \sigma_z \end{Bmatrix} = \begin{bmatrix} C_{rr} & C_{r\theta} & C_{rz} \\ C_{r\theta} & C_{rr} & C_{rz} \\ C_{rz} & C_{rz} & C_{zz} \end{bmatrix} \begin{Bmatrix} \varepsilon_r \\ \varepsilon_\theta \\ \varepsilon_z \end{Bmatrix} \tag{2.5}$$

where C_{rr}, $C_{r\theta}$, C_{rz}, and C_{zz} are 4 of the 5 independent material coefficients, and ε_z, ε_θ and ε_r are the strains in the axial, hoop and radial directions, respectively. Note that for a transversely isotropic material the remaining independent coefficient relates the shear stresses to the strains. In this study samples have only been loaded in the principal directions, hence this coefficient has not been employed. Shear components are thus not within the scope of this study.

2.3.3 Compliance Value Determination

During testing, the loads are measured directly. However, because samples are brought to failure, sometimes catastrophically, it is not possible to directly measure strain via the usual methods. For this reason, the strains are calculated from the measured loads and material constants. The material constants are first measured via a series of tests of different stress states within the small strain region. The stress states investigated are: axial tension, circumferential tension, pure shear, and equibiaxial tension. In these tests, one extensometer is attached to the tube to measure axial strain and second extensometer is modified to measure the hoop strain, Figure2.3. The modification involves attaching wire to the clips of the extensometer and wrapping the wire around the diameter of the cylinder. Rather than measuring an axial extension, the extensometer reads a change in circumference. With the extensometers, strain data are obtained from the linear elastic region in order to determine the stiffness matrix, and subsequently the

compliance matrix using the procedure detailed in the following paragraphs. As a reiteration, extensometers are not attached to any of the specimens that are tested to failure.

In uniaxial tension, σ_z is the only applied stress. Thus, the following equations are obtained from Hooke's law:

$$\sigma_r = 0 = C_{rr}\varepsilon_r + C_{r\theta}\varepsilon_\theta + C_{rz}\varepsilon_z \tag{2.6}$$

$$\sigma_\theta = 0 = C_{r\theta}\varepsilon_r + C_{rr}\varepsilon_\theta + C_{rz}\varepsilon_z \tag{2.7}$$

$$\sigma_z = C_{rz}\varepsilon_r + C_{rz}\varepsilon_\theta + C_{zz}\varepsilon_z \tag{2.8}$$

Similar equations may also be written for other states of stress. With these equations, the stiffness matrix, **C**, can be determined. Inversion of the matrix yields the compliance matrix, **S**, from which the principal strains may be calculated using Hooke's law:

$$\varepsilon_r = S_{r\theta}\sigma_\theta + S_{rz}\sigma_z \tag{2.9}$$

$$\varepsilon_\theta = S_{rr}\sigma_\theta + S_{rz}\sigma_z \tag{2.10}$$

$$\varepsilon_z = S_{rz}\sigma_\theta + S_{zz}\sigma_z \tag{2.11}$$

where S_{ij} are components of the compliance matrix. These equations are for the case of a transversely isotropic material in the absence of shear. Again, radial stresses are considered negligible.

Consistent with linear viscoelastic behavior, it is decided to keep the nominal octahedral shear strain rate constant during testing. The octahedral shear strain rate, $\dot{\gamma}^{oct}$, is calculated from equation 2.12:

$$\dot{\gamma}^{oct} = \frac{1}{3}\sqrt{(\dot{\varepsilon}_r - \dot{\varepsilon}_\theta)^2 + (\dot{\varepsilon}_\theta - \dot{\varepsilon}_z)^2 + (\dot{\varepsilon}_z - \dot{\varepsilon}_r)^2} \tag{2.12}$$

where, $\dot{\varepsilon}_r$, $\dot{\varepsilon}_\theta$ and $\dot{\varepsilon}_z$ are the radial, circumferential and axial strain rates. These values are calculated from the applied stress rates as follows:

$$\dot{\varepsilon}_r = S_{r\theta}\dot{\sigma}_\theta + S_{rz}\dot{\sigma}_z \tag{2.13}$$

$$\dot{\varepsilon}_\theta = S_{rr}\dot{\sigma}_\theta + S_{rz}\dot{\sigma}_z \tag{2.14}$$

$$\dot{\varepsilon}_z = S_{rz}\dot{\sigma}_\theta + S_{zz}\dot{\sigma}_z \tag{2.15}$$

where $\dot{\sigma}_z$ and $\dot{\sigma}_\theta$ are the stress rates in the axial and hoop directions and S_{ij} are the material compliance values described previously.

2.3.4 Strain Scaling Procedure

The equations discussed above, derived from Hooke's Law, are valid only in the linear elastic regime, although the testing performed in this study extends into the non-linear region. To account for this non-linearity, the strains are assumed to scale with the displacement, δ, with scale factors obtained from the linear portion of plots of the strains calculated using equations (2.9-2.11) as a function of crosshead displacement. Figure 2.4 is an example of such a plot for the case of uniaxial tension. Therefore, the experimental principal strain values, ε_i', are calculated as:

$$\varepsilon_r' = m_r\delta \tag{2.16}$$

$$\varepsilon_\theta' = m_\theta\delta \tag{2.17}$$

$$\varepsilon_z' = m_z\delta \tag{2.18}$$

where m_r, m_θ and m_z are the slopes of the plot of ε_r, ε_θ and ε_z (respectively) versus δ. Strain values calculated in this manner for the case of uniaxial tenison compare well with

those measured with extensometers for the case of axial tension in tensile bars (Figure 2.5).

2.4 Results and Discussion

2.4.1 Compliance and Stiffness Values

Table 2.1 indicates the values determined for the compliance and stiffness terms for the MSMC material. Both the compliance and stiffness matrices are determined to be positive-definite. The method used in this determination is described, for example, in Ting[34]. The values for tensile modulus and Poisson's ratio calculated from the compliance values are presented in Table 2.2. They compare well with those from tensile bar measurements, indicating that the method of measurement is satisfactory. Differences could be due to the fact that different procedures were used to produce the samples (extrusion and injection molding).

2.4.2 Biaxial Testing Results

Samples are tested at room temperature (20°C) at an octahedral shear strain rate of 0.05 min^{-1}. Figure 2.6 plots the octahedral shear yield stress, τ_y^{oct}, as a function of the mean stress, σ_m. In studying the yield behavior of various polymers, other investigators[10,11] have found a linear relationship between τ_y^{oct} and σ_m. Such a linear dependence, with the slope referred to as the coefficient of internal friction, indicates a modified von Mises type of behavior. Our data does not show this type of relationship, however. While τ_y^{oct} appears to be dependent upon the pressure, a linear dependence is not clear. Rather, the relationship between yield stress and pressure appears to be

not clear. Rather, the relationship between yield stress and pressure appears to be convoluted due to processing effects that have introduced anisotropy in both the stiffness and yield behavior. Others[9,35] have previously suggested that a linear relationship as described above does not exist in the case of anisotropic polymers. For such reasons, a more suitable way to present the data is in the form of circumferential yield stress versus axial yield stress (Figure 2.7).

Figure 2.8 presents some of the failed specimens with the dashed lines indicating the respective loading paths (slope = σ_z/σ_θ). Macroscopically, a wide range of ductility is observed for this material depending on the stress state applied to the sample. For example, specimens tested with a compressive axial stress component appear quite ductile. With the exception of uniaxial tension, as the axial component becomes tensile the failures appear to become more brittle. This is evident since much energy is dissipated through the creation of new surface area rather than irreversible damage. As an example, for the stress state in which the axial component is twice that of the circumferential component, the specimen is shattered into pieces that could be reassembled together to regain the original shape. The failure is clearly brittle. In other stress states, the mode of failure is not so clear from visual inspection. The case of equal axial and circumferential applied stress components is one such case. In this specimen, both irreversible deformation and creation of new surface area can be observed, which indicates both ductile and brittle characteristics. For this reason, a zero-slope condition in the octahedral shear stress versus volumetric strain curve is chosen as the criteria for ductile or brittle failure: ductile yield is assigned when a zero-slope condition in the

volumetric strain, ε_v, versus octahedral shear stress, τ_y^{oct}, data is achieved while samples that do not achieve a zero slope condition are assigned as brittle. These quantities can be calculated from equation 2.3 and the following equation:

$$\varepsilon_v = \varepsilon_r + \varepsilon_\theta + \varepsilon_z \tag{2.19}$$

Figure 2.9 illustrates the volumetric strain versus octahedral shear stress response for the MSMC material tested in various stress states applied at the same nominal octahedral shear strain rate of 0.05 min^{-1} at 20°C. As expected, at higher positive values of ε_v, the yield stress value is reduced. It is also evident from this figure that ductile yield behavior, as determined by a zero slope condition in the curve, was not always realized. Curves that do not display a slope of zero are indicated by dashed lines, and the failures are considered brittle. However, the brittle response does not correspond to the highest level of volumetric strain. It is typically observed that the more constrained stress states (i.e., those with the highest dilatational component) are most likely to promote brittle type failures, while yielding is associated with a deviatoric material response. The fact that our observations do not follow this trend is believed to be associated with imposed residual stresses, and is discussed further in Chapter 5.6.6 in the comparison of processing condition effects.

The specimen shown in Figure 2.8 which is loaded under the condition σ_z/σ_θ=2 (and specimens not pictured here, but loaded under conditions of σ_z/σ_θ=1.5, 1.75, 2.0, 3.0, 3.5) indicates a brittle failure. Such brittle failures showed little evidence of irreversible deformation. As mentioned previously, similar brittle behavior was observed by Carapellucci and Yee[9] in a study of polycarbonate cylinders for a sample

loaded under conditions with $\sigma_z/\sigma_\theta = 1.7$. In that study, there was no report of any other samples tested within the range of stress states for which our specimens demonstrated brittle behavior.

Figure 2.10 plots the axial and circumferential stress data, differentiating between ductile and brittle behavior.

It is noted that the yield strength in axial compression (~57 MPa) is below the calculated static buckling stress for a specimen of this geometry (~210 MPa). It is also noted that the dynamic buckling stress may be lower than this, and is determined to be as low as ~140 MPa. This is still much greater that the stresses reached during compressive loading in this study. The method for calculating the buckling stresses can be found in the reference by Lindberg[36].

C_{rr} (MPa)	3977
C_{rz} (MPa)	1502
$C_{r\theta}$ (MPa)	212
C_{zz} (MPa)	2895
S_{rr} (MPa^{-1})	3.23×10^{-4}
S_{rz} (MPa^{-1})	-1.97×10^{-4}
$S_{r\theta}$ (MPa^{-1})	5.72×10^{-5}
S_{zz} (MPa^{-1})	5.70×10^{-5}

Table 2.1: Compliance and stiffness values determined for the MSMC material from initial low-strain hollow cylinder testing at 20°C.

Determined from:	E (MPa)	ν
Tensile bar	1818	.36
Compliance values	1607	.41

Table 2.2: Tensile modulus and Poisson's ratio values determined from uniaxial tensile tests performed on standard tensile bars and as calculated from the compliance values presented in Table 2.1.

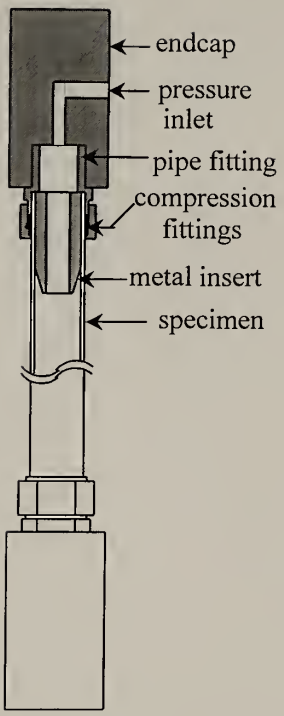

Figure 2.1: Schematic of specimen gripping system.

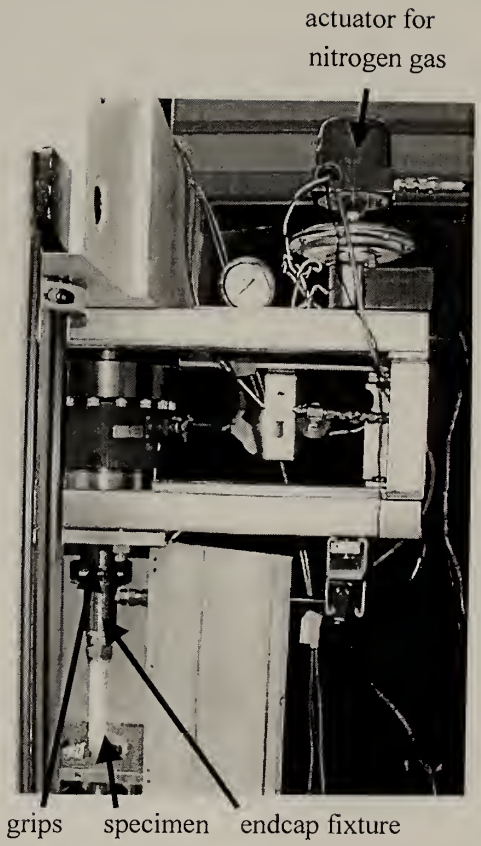

Figure 2.2: Image of tension/torsion machine modified for biaxial testing. Important features are indicated with arrows.

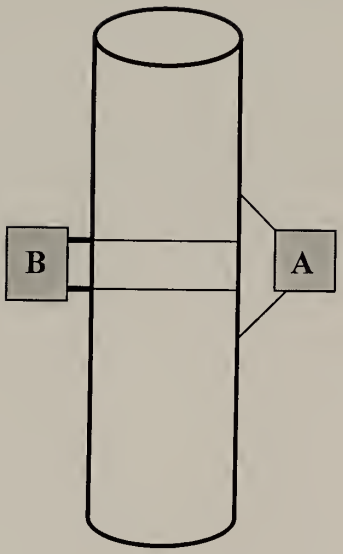

Figure 2.3: Schematic of set-up for stiffness value determination. One extensometer (A) measures axial strain, a second (B) measures circumferential strain.

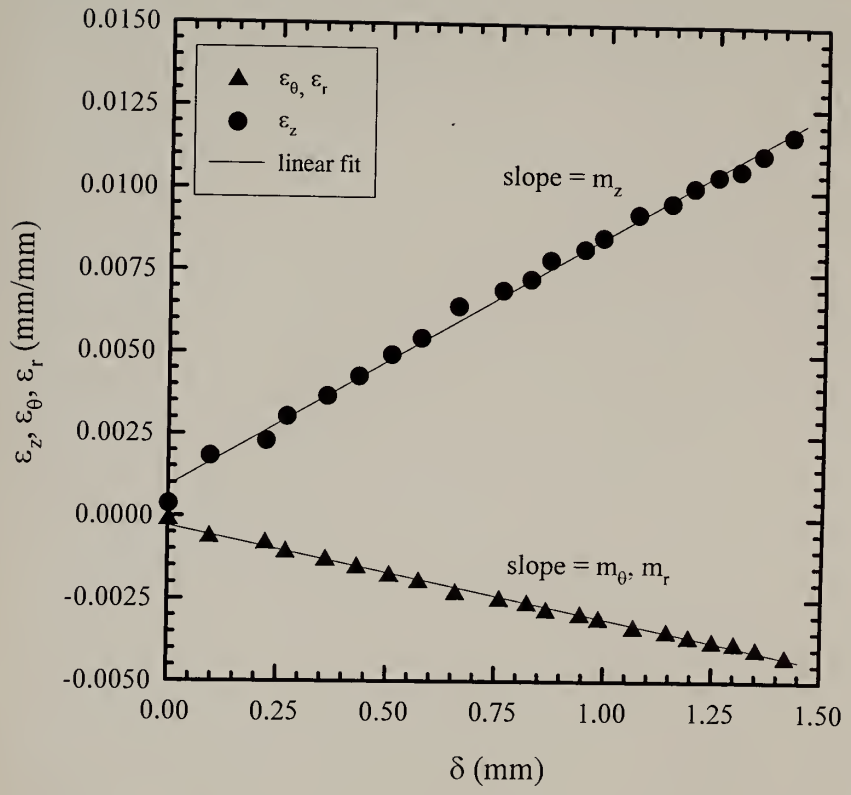

Figure 2.4: Plot of strain components ε_r, ε_z and ε_θ (equations 4.9-4.11) versus crosshead displacement, δ, for MSMC material. Line indicates linear least-squares fit.

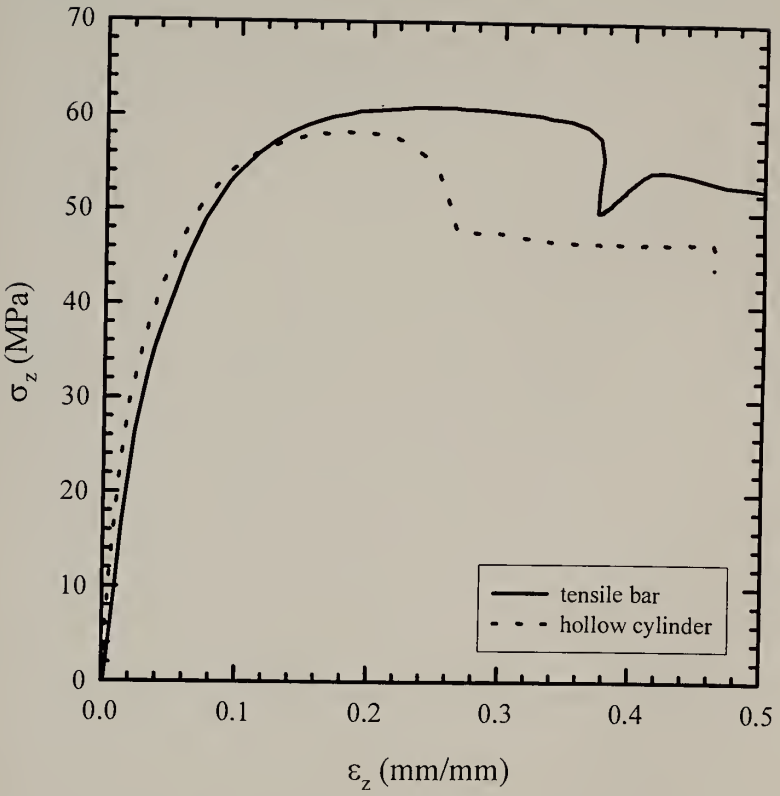

Figure 2.5: Plot of axial stress, σ_z, versus axial strain values calculated from scaling method (equations 2.16-2.18) compared with those measured with extensometers in uniaxial tensile tests.

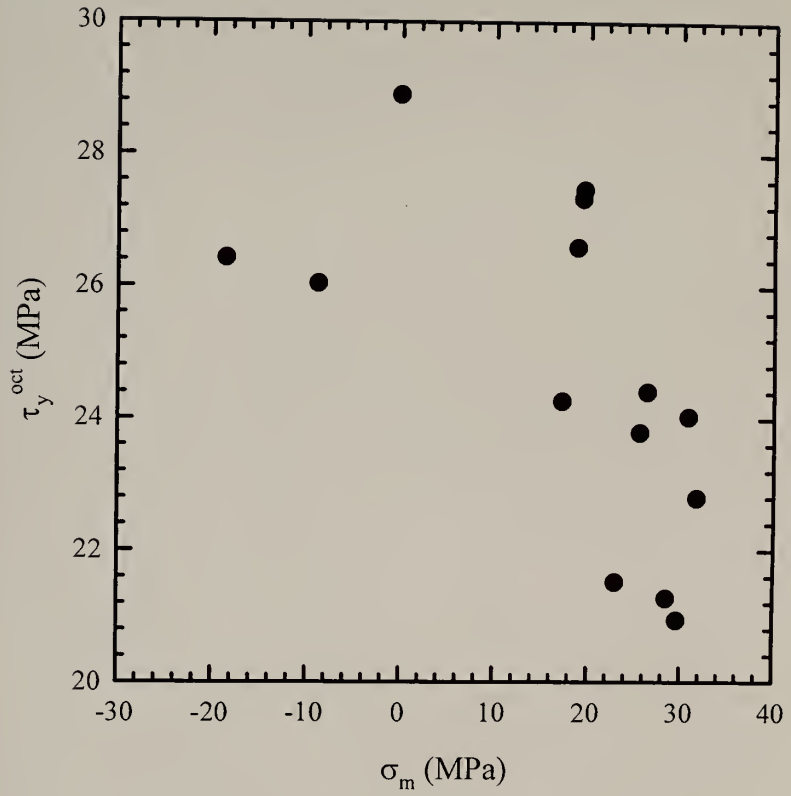

Figure 2.6: Octahedral shear stress at yield, τ_y^{oct} versus mean stress, σ_m, for MSMC material.

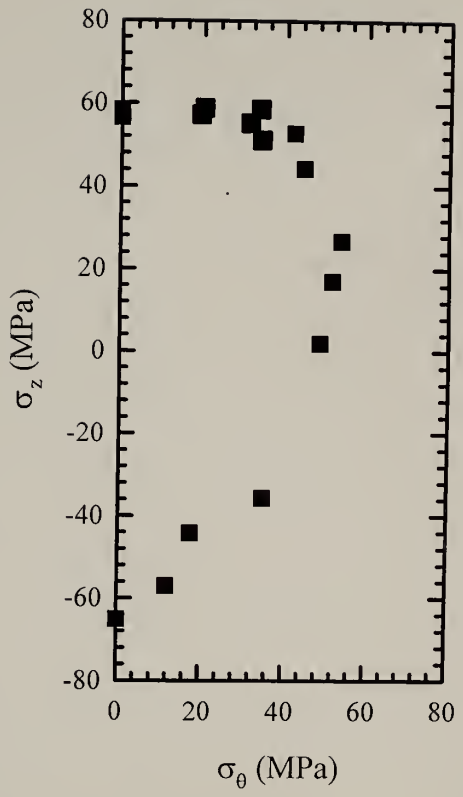

Figure 2.7: Axial stress, σ_z, versus circumferential stress, σ_θ, for MSMC material. Values are taken at yield or failure if no yielding occurs.

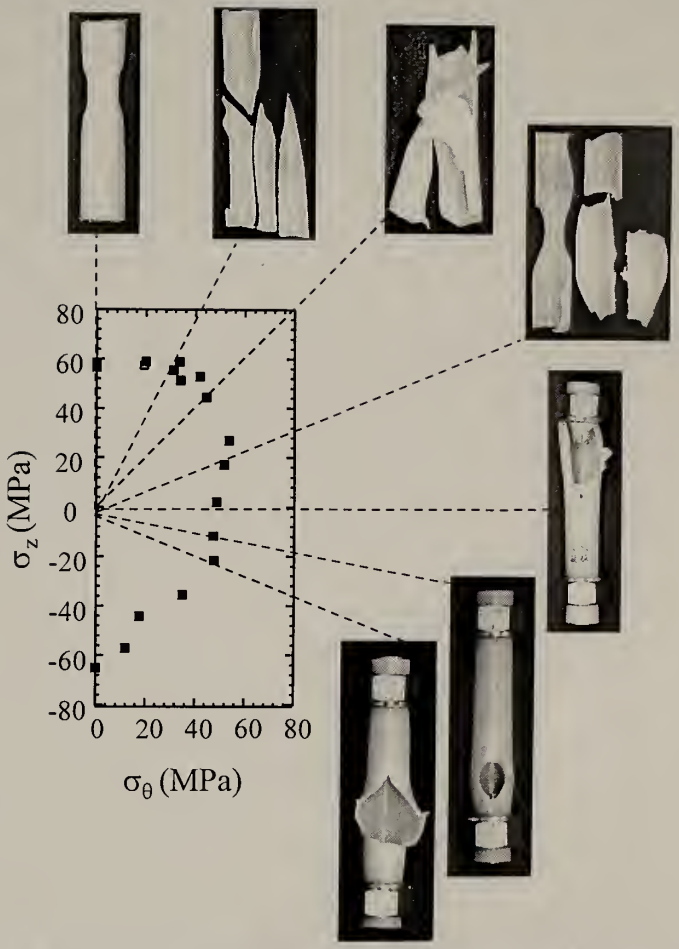

Figure 2.8 Axial stress, σ_z, versus circumferential stress, σ_θ, for MSMC material with dashed lines indicating the corresponding failed specimen for selected stress states.

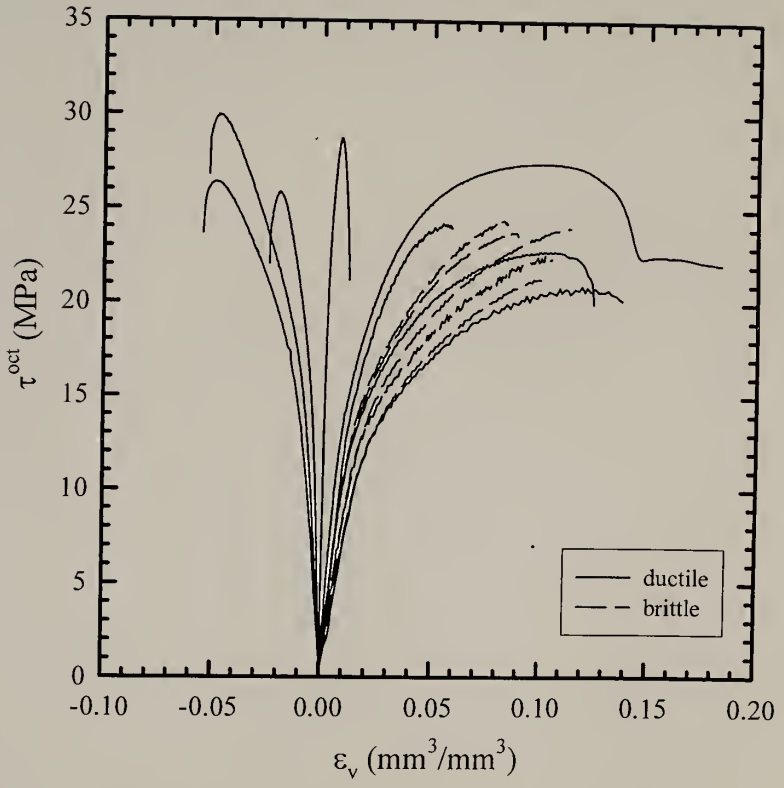

Figure 2.9: Octahedral shear stress, τ^{oct} versus volumetric strain, ε_v, for MSMC material. Solid lines represent ductile failures, dashed lines indicate brittle failures.

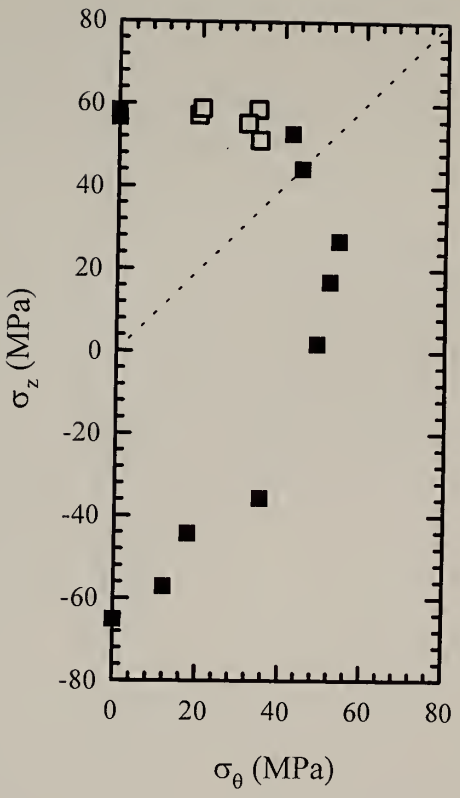

Figure 2.10: Axial stress, σ_z, versus circumferential stress, σ_θ, for MSMC material. Solid symbols represent ductile yield and hollow symbols represent brittle failure. Dashed line indicates the stress state of equi-biaxial tension.

CHAPTER 3

EFFECT OF TEST TEMEPERATURE AND STRAIN RATE

3.1 Background

Testing conditions strongly influence the properties that are measured for a given material. Typically, the trends that are observed with strain rate are: increase in yield strength and modulus and decrease in yield strain with increasing strain rate. With regard to increasing test temperature, the trends are the opposite: decrease in yield strength and modulus, increase in yield strain with increase in temperature. In terms of failure behavior, it is typically observed that polymers become more ductile with either increasing temperature or decreasing strain rate.

3.2 Material

The material tested in this portion of work is the same as that described in the Chapter 2.2. All sample preparation procedures are also performed as described previously.

3.3 Experimental

3.3.1 Uniaxial Testing

Preliminary tensile testing is performed on injection molded bars. This is performed in accordance with ASTM standards[33]. Extensometers are attached to samples in order to measure the strain. Crosshead speed controls the nominal strain rate.

Testing is performed at various extension rates and temperatures in order to identify any trends in properties and behavior. An Instron Eurotherm oven is utilized in order to perform tests at constant temperature.

3.3.2 Biaxial Testing

Hollow cylindrical specimens tested in one portion of this work are tested at different temperatures. This is made possible by the chamber, mentioned in Chapter 2.3.2 and shown in Figure 2.2, that encloses the specimen during testing. For test temperatures above room temperature (50 and 80°C) the chamber is equipped with heating pads on two of the walls and a port that blows heated nitrogen gas into the chamber. A temperature controller with attached thermocouple measures and maintains the temperature at the desired level. Prior to testing, specimens are conditioned in a separate oven at the desired temperature for 30 minutes. Once gripped in the testing apparatus, the specimen rests until the temperature within the chamber has equilibrated. Testing then begins in the manner described in Chapter 2.3.2.

For testing at 0°C, a liquid nitrogen tank is attached to the port previously utilized for heating purposes. In this case, the temperature controller regulates a solenoid valve that allows the nitrogen to flow into the chamber. Specimens are placed in sealed plastic bags and placed in an ice-water bath for 60 minutes to bring them to the appropriate temperature prior to testing. Again, once the specimen is gripped within the testing apparatus, testing begins only after the temperature within the chamber has equilibrated.

Small strain tests to measure the compliance values, as described in Chapter 2.3.2, are also performed on the hollow cylinders at 0, 50 and 80°C in addition to those

done at 20°C. This is necessary as these values are used to calculate the strain and strain rate values. The stiffness and compliance values are listed in Table 5.1.

Testing was also performed at 20°C at octahedral shear strain rates of 0.005, 0.05 and 0.5 min^{-1}. The test program allows the control of the strain rate during testing. The test procedure is otherwise the same as described in Chapter 2.3.2.

3.4 Uniaxial Test Results

Figure 3.1 shows the effect of strain rate on the yield strength during uniaxial tensile testing of the injection molded bars. The increase in yield strength with rate is typical behavior. Similarly, Figure 3.2 indicates an increase in tensile modulus with strain rate. At the same rates, a decrease in percent strain at yield in observed, Figure 3.3. Again, this is typical behavior that would be expected for this type of material. It is observed that the increase in yield strength is rather small. Over 3 orders of magnitude of strain rate, the strength at yield varies by only a few megapascals.

Uniaxial tensile tests are also performed at 0, 20, 50 and 80°C. A decrease in yield strength and modulus with increasing temperature is observed (Table 3.2). This is also shown in separate studies on this material[15,37-39]. The uniaxial tensile data at these temperatures seem to be in good agreement with the uniaxial tensile data from other studies[15,39]. It should be noted, however, that different specimen geometries and processing conditions were used in each of these studies.

For all rate and temperatures examined here, the material behaves in a ductile manner when tested in uniaxial tension. This is even observed at 0°C, which is below

the reported glass transition temperature. Large amounts of energy can be absorbed by the polyketone due to the ability to form a stable neck upon drawing.

3.5 Biaxial Test Results

3.5.1 Rate Effects on Yield Strength and Failure Mode

The yield stresses in the axial and circumferential directions for the cylinders tested at =0.005, 0.05, and 0.5 min^{-1} at 20°C are plotted in Figure 3.4. In this figure, solid and hollow symbols represent ductile and brittle failures, respectively, determined by the criterion described in Chapter 2.4.2. An increase in yield strength with strain rate is evident, as expected. Similar to the uniaxial testing results, this difference is not very large. While the strain rate varies over two orders of magnitude, the yield strength increases by only a few megapascals. Additionally, the cylinders' sensitivity to strain rate appears to be greater in the circumferential direction than the axial direction. This difference in yielding in the axial and hoop directions is attributed to the anisotropy introduced during extrusion of the test specimens.

At all rates the observed failures for hollow cylinders are predominantly ductile. However, brittle behavior is consistently observed for the case of $\sigma_z/\sigma_\theta=2$ and similar stress states. Figures 3.5 and 3.6 illustrate the stress-strain curves and the observed failures for specimens subjected to this stress state ($\sigma_z/\sigma_\theta=2$) at different octahedral shear strain rates. Using the criterion described in Chapter 2.4.2, the octahedral shear stress/volumetric strain curves indicate that these failures are brittle. Macroscopically, the samples also appear to have failed in a very brittle manner and appear quite similar to each other. Likewise, the rate seems to have little effect on the failure mode in the other

stress states examined. At both the higher and lower rates, the failed specimens appear quite similar to those shown in Figure 2.8 for the moderate rate.

3.5.2 Temperature Effects on Yield Strength and Failure Mode

The test temperature appears to affect the yield strength of the polymer more significantly than the strain rate. The hoop and axial stresses at yield for specimens tested at 20, 50 and 80°C are plotted in Figure 3.7. It is interesting to note that the effect of strain rate is more pronounced in the hoop direction, while the effect of temperature is much greater in the axial direction. It is believed that this is due to the anisotropic character of the material and, in particular, the morphology of the amorphous phase. The amorphous orientation induced during the extrusion process can alter the internal energy of the material through entropic considerations. Thus, one should expect that testing the material at different temperatures would not produce similar results as testing the material at different rates in this case.

Specimens tested at 50 and 80°C behave in a ductile manner for all stress states studied. Interestingly, neck formation is observed for the stress state ($\sigma_z/\sigma_0=2$) that, at 20°C, results in brittle behavior at all rates (Figure 3.8). The necks produced at this stress state are of larger diameter than the necks produced in axial tension as a result of the constraint on the material due to internal pressurization.

At 0°C, failure is typically brittle with specimens fracturing into many small pieces. As this is below the reported glass transition temperature of approximately 12°C, brittle behavior was expected. A small amount of irreversible deformation is evident in the case of circumferential tension, however. Another exception is the state of axial

compression, for which ductile yield is observed. The circumferential and axial stresses at yield for specimens tested at 0, 20, 50 and 80°C are plotted in Figure 3.9.

Finally, it is not believed that conditioning the samples at higher temperatures has significant effect on the crystallinity of the samples. The temperatures used in this study are significantly below the melting temperature of the material (225°C). It is known that this material undergoes a crystal transformation at approximately 100-115°C[40,41], however, differential scanning calorimetry work has not shown any significant features in the temperature range studied here. Additionally, the crystallization of this material is known to be very rapid[42]. It not expected that much difference in crystallinitywould arise from different preparation conditions.

3.6 Summary

With respect to yield strength, the effects of rate and temperature under biaxial loading conditions are similar to those under uniaxial loading conditions. However, while the failure mode at all temperatures and strain rates in uniaxial tension are ductile, as indicated by the propagation of a stable neck, failures in biaxial stress states are strongly dependent upon the stress state and temperature. At 0°C, below the reported T_g, brittle failures are mainly observed, except for the case of axial compression. At 20°C, slightly above T_g, mixed failure behavior is observed. At 50 and 80°C, significantly above T_g, all failures are ductile. The failure mode under biaxial loading conditions is not noticeably affected by the shear strain rates examined here at 20°C.

	0°C	20°C	50°C	80°C
C_{rr} (MPa)	4095	3977	1410	1384
C_{rz} (MPa)	1416	1502	764	756
$C_{r\theta}$ (MPa)	456	212	-379	-320
C_{zz} (MPa)	3832	2895	1565	1466
S_{rr} (MPa^{-1})	2.80×10^{-4}	3.23×10^{-4}	2.04×10^{-3}	2.06×10^{-3}
S_{rz} (MPa^{-1})	-1.05×10^{-4}	-1.97×10^{-4}	-1.72×10^{-3}	-1.82×10^{-3}
$S_{r\theta}$ (MPa^{-1})	5.30×10^{-6}	5.72×10^{-5}	4.18×10^{-3}	1.47×10^{-3}
S_{zz} (MPa^{-1})	3.39×10^{-4}	5.70×10^{-5}	2.32×10^{-3}	2.56×10^{-3}

Table 3.1: Stiffness (C) and compliance (S) values determined for MSMC material at various temperatures.

	Carilon® tensile bars		Carilon® hollow cylinders		Kalay and Bevis[39]		Danforth et al.[15]	
T (°C)	σ_y (MPa)	E (GPa)	σ_y (MPa)	E (GPa)	σ_y (MPa)	E (GPa)	σ_y (MPa)	E (GPa)
0	71	N/A	N/A	2.56	N/A	N/A	64.7	N/A
20 [23]	59	1.4	60.9	1.61	[59.3]	[1.83]	[62]	[1.7]
50	53.5	.98	47.3	1.06	N/A	N/A	N/A	N/A
80	46.3	.69	41.4	0.89	47.7	1.1	N/A	N/A

Table 3.2: Yield stress, σ_y, and tensile modulus, E, at various temperatures. Data collected from various sources as indicated.

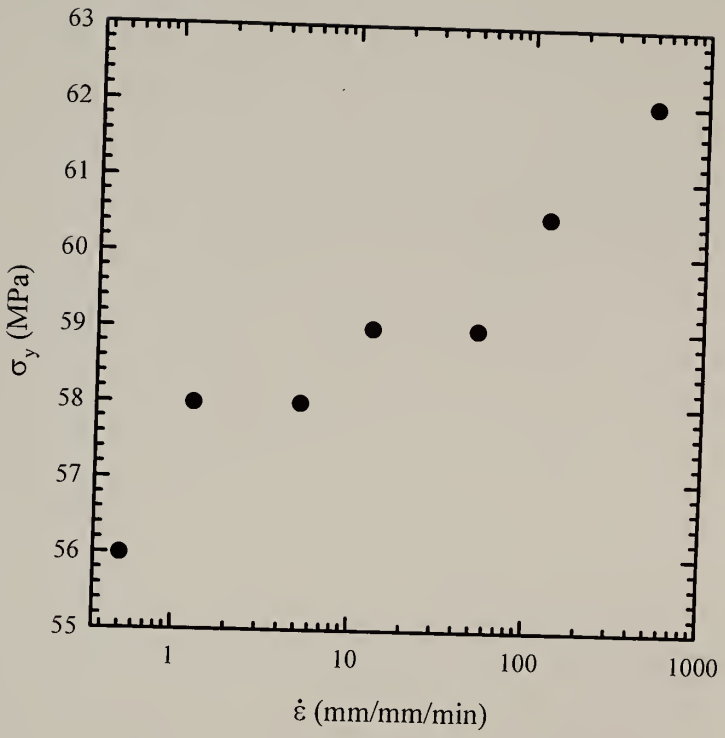

Figure 3.1: Yield stress, σ_y, as a function of strain rate, $\dot{\varepsilon}$, for uniaxial tensile tests performed on tensile bars.

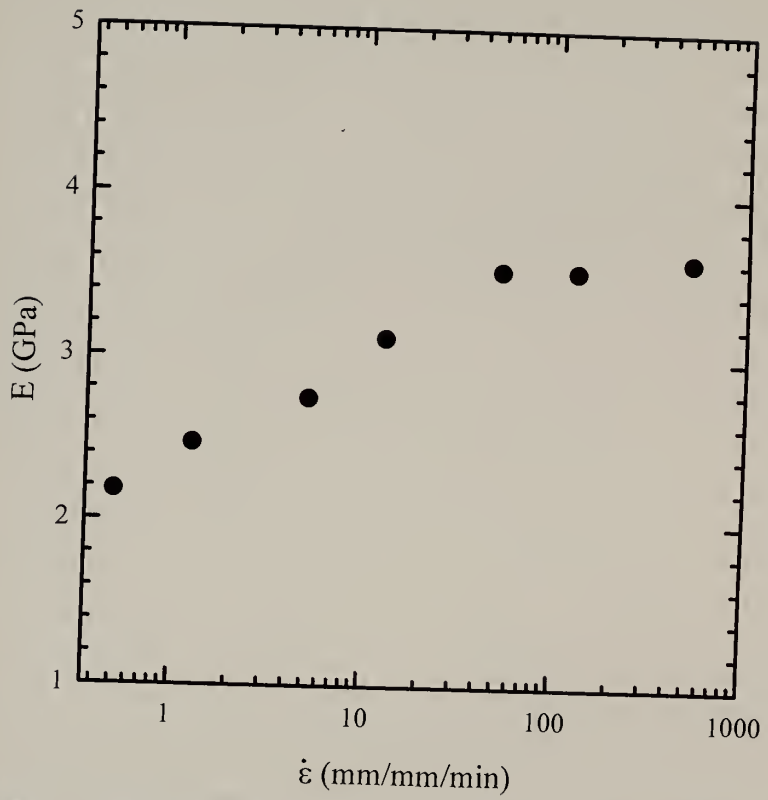

Figure 3.2: Tensile modulus, E, as a function of strain rate, $\dot{\varepsilon}$, for uniaxial tensile tests performed on tensile bars.

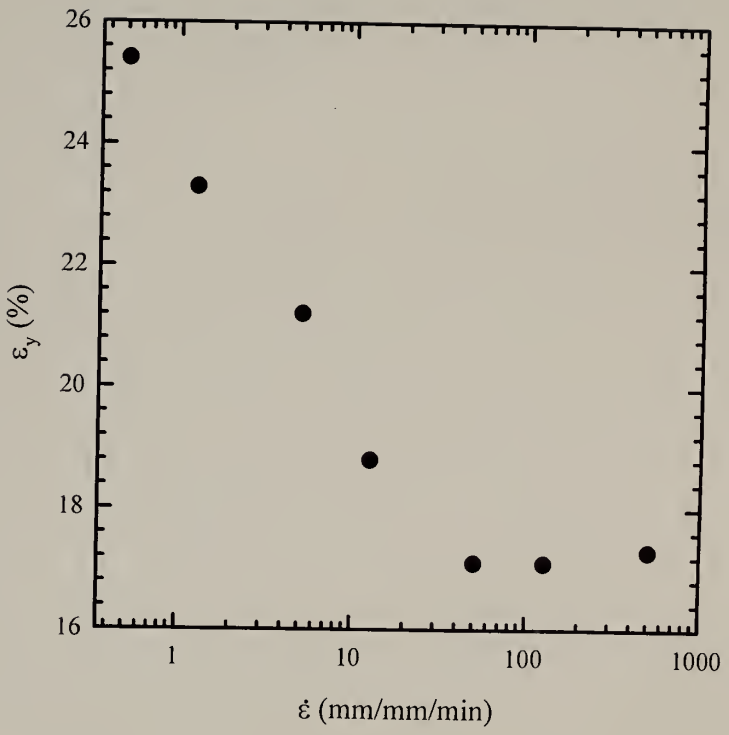

Figure 3.3: Strain at yield, ε_y, as a function of strain rate, $\dot{\varepsilon}$, for uniaxial tensile tests performed on tensile bars.

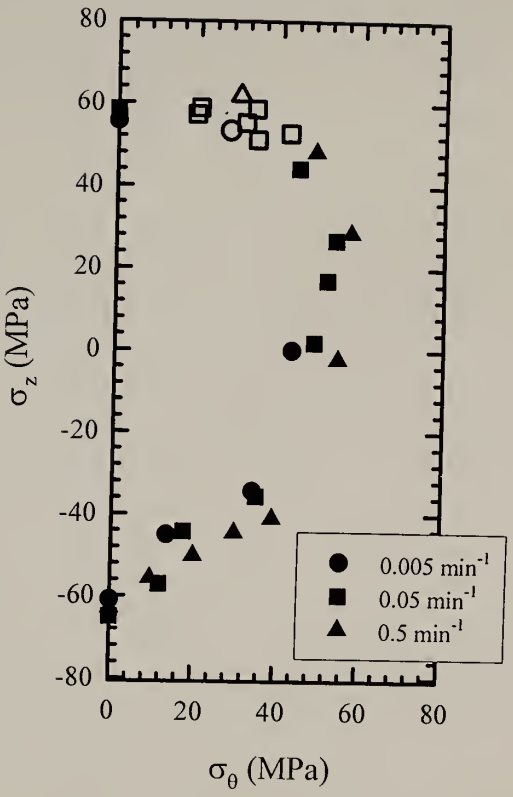

Figure 3.4: Circumferential stress, σ_θ, versus axial stress, σ_z, for MSMC material tested at nominal octahedral shear strain rates of 0.005, 0.05 and 0.5 min^{-1}. Hollow symbols represent brittle failure and solid symbols represent ductile failure.

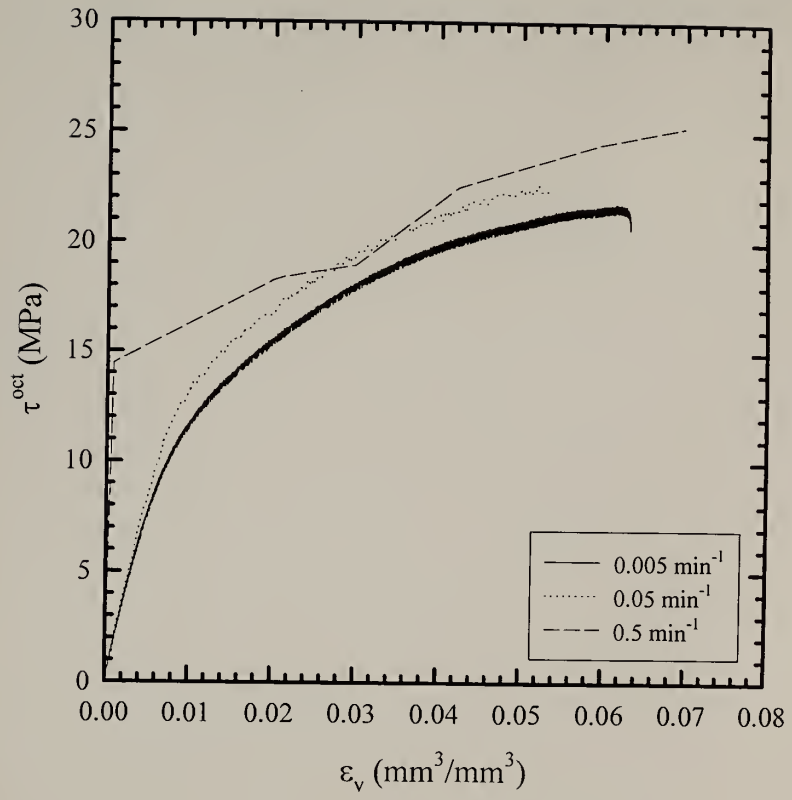

Figure 3.5: Volumetric strain, ε_v, versus octahedral shear stress, τ^{oct}, for MSMC material tested at nominal octahedral shear strain rates of 0.005, 0.05 and 0.5 min^{-1}. The stress state is such that the axial stress is twice the value of the circumferential stress.

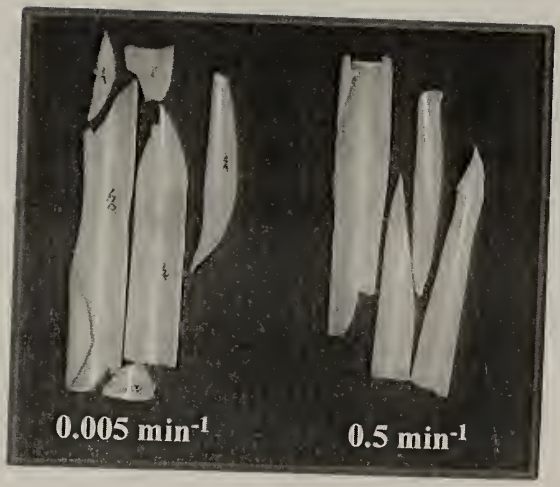

Figure 3.6: Images of failed MSMC material tested at nominal octahedral shear strain rates of 0.005 and 0.5 min^{-1}. The stress state is such that $\sigma_z/\sigma_\theta=2$.

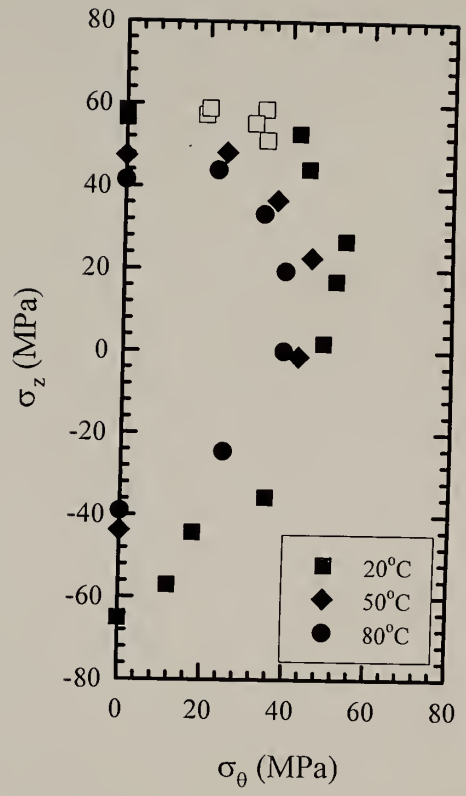

Figure 3.7: Circumferential stress, σ_θ, versus axial stress, σ_z, for MSMC material tested at 20, 50 and 80°C. Solid symbols represent ductile failure, hollow symbols represent brittle failure.

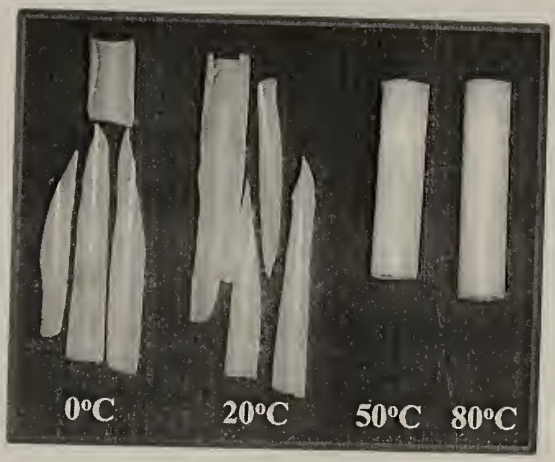

Figure 3.8: Images of samples tested under equibiaxial loading conditions at 0, 20, 50 and 80°C. The stress state is such that $\sigma_z/\sigma_\theta=2$.

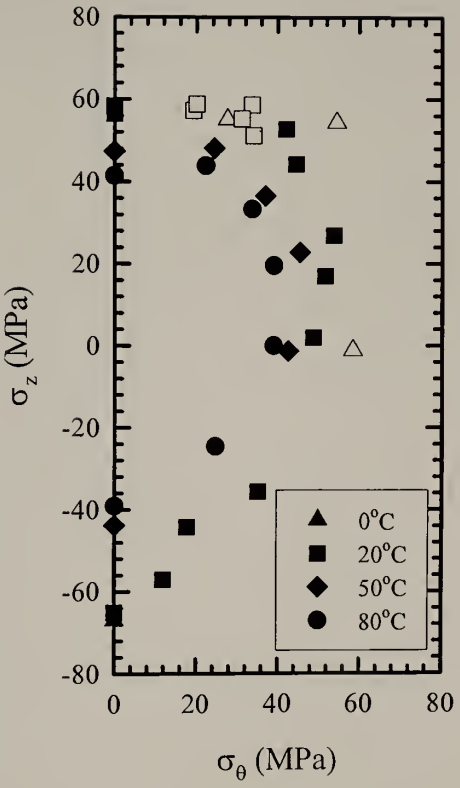

Figure 3.9: Circumferential stress, σ_θ, versus axial stress, σ_z, for MSMC material tested at 0, 20, 50 and 80°C. Solid symbols represent ductile failure, hollow symbols represent brittle failure.

CHAPTER 4

MODELING TEMPERATURE AND RATE EFFECTS

4.1 Background

The importance of modeling the yield behavior of materials is evident by the number of studies that have considered this subject. Clearly, the ability to predict the capacity of a material to withstand a specified loading condition has great practical importance. Many efforts at modeling begin with classical works such as that by von Mises[43] for isotropic materials (or as modified by Hill[44] for anisotropic metals). Both of these continuum level criteria consider the yield stress of the material to be independent of pressure. For polymers, however, pressure dependence must be taken into account. Work by Sternstein and Ongchin[8], for example, shows that behavior of poly (methyl methacrylate) follows a von Mises type behavior modified to include pressure effects. In addition to pressure, the effects of temperature and strain rate on the behavior of polymeric materials must be considered in an appropriate criterion.

Many criteria to date have considered the case of isotropic glassy polymers. Yield criteria for amorphous glassy polymers are compared by Quinson et al.[45]. The study looks at the behavior of three different polymers in axial compression, axial tension, simple shear, and plane strain compression. The data is compared with predictions from von Mises and Tresca type criteria, both modified to include pressure dependence. It is found that both criteria are satisfactory under certain conditions.

Testing is performed at different temperatures, but a single strain rate is used. Other studies, such as that by Carapellucci and Yee[9] have looked at anisotropic glassy polymers. In the investigation, von Mises and Hill criteria are modified to account for the pressure dependence of the polymer. The criteria are compared with yield strength data from biaxial testing at two temperatures. Good agreement to experimental data is found at 25°C but not at –40°C. While tests are performed at two different temperatures, the stress rate was maintained constant for all tests. Hoffman[46] proposes a criterion for the brittle failure of orthotropic materials. The criterion is based on that of Hill, but is modified to include pressure dependence. Theoretical predictions are made for the uniaxial tensile and compressive yield strengths as a function of the angle between the orientation and loading directions. Predictions fit well with experimental data, but the model cannot account for changes in rate or temperature.

Some authors have looked at the yielding of composite materials. One such criterion is for the anisotropic strength of unidirectional or laminated composites[47]. The model predictions are compared to the yield stress measured at various angles relative to the filament direction. Good agreement is found. Again, the effects of rate and temperature are not considered in the analysis. Tsai and Wu also[48] describe a criterion for the strength of anisotropic materials, filament composites in particular. Their criterion considers the Bauschinger effect and multi-axial stresses, but does not consider the effects of rate or temperature on the yield stress.

More relevant to the current investigation are studies that have considered anisotropic semi-crystalline polymers. Early work in this area includes a von Mises type

criterion modified to include effects of anisotropy and a "built-in" compressive stress in the draw direction[49]. The study compares model predictions for drawn amorphous poly(ethylene terepthalate) with uniaxial yield and shear stress values measured experimentally at various angles to the draw direction. Good fitting is found, but again, the effects of rate or temperature are not considered.

In an independent study, Caddell et al.[35] developed a criterion, similar to those of Stassi-Dalia[50] and Hoffman[46] for pressure dependent anisotropic materials. The criterion was developed in the following form:

$$H(\sigma_x-\sigma_y)^2+F(\sigma_y-\sigma_z)^2+G(\sigma_z-\sigma_x)^2+2N\tau_{xy}{}^2+2L\tau_{yz}{}^2+2M\tau_{zx}{}^2 +K_x\sigma_x+K_y\sigma_y+K_z\sigma_z=1 \qquad (4.1)$$

where σ_x, σ_y and σ_z are the normal stresses in the principal directions of anisotropy; τ_{xy}, τ_{yz} and τ_{zx} are the shear stresses; H, F and G are parameters related to the normal stresses; L, M and N are related to the shear stresses; and the parameters K_x, K_y and K_z account for the pressure dependence. These parameters are defined as follows:

$$H+G=\frac{1}{C_xT_x} \qquad (4.2)$$

$$F+H=\frac{1}{C_yT_y} \qquad (4.3)$$

$$G+F=\frac{1}{C_zT_z} \qquad (4.4)$$

and

$$K_x=\frac{C_x-T_x}{C_xT_x} \qquad (4.5)$$

$$K_y = \frac{C_y - T_y}{C_y T_y} \tag{4.6}$$

$$K_z = \frac{C_z - T_z}{C_z T_z} \tag{4.7}$$

where C_i and T_i represent the absolute values of the uniaxial compressive and tensile strengths, respectively, in the reference directions x, y and z. This criterion has been shown to fit reasonably with experimental data of polymers such as polypropylene[14,35], poly(vinyl chloride)[35] and polyethylene[13]. While the model was developed for pressure dependent and anisotropic materials, the equations reduce to the appropriate form for isotropic ($T_x=T_y=T_z$, $C_x=C_y=C_z$) or pressure independent ($C_i=T_i$) materials.

The studies described above consider the yield phenomenon at the continuum level. Other studies look at yielding on the molecular level. Robertson[51] presents a model for the flow of glassy polymers based on the biasing of chain conformations due to the application of a shear stress. The effects of temperature and strain rate are included in the model. In a later paper, Argon[52] describes the temperature, pressure, and strain rate dependence of the flow stress of glassy polymers. In the theory, local strain is produced by motion of molecular kinks.

In a more recent article, Lesser and Kody[11] develop a model for the yielding of isotropic glassy polymers. The investigation elucidates the yield and failure response of epoxy systems under multi-axial stress states, including the effects of rate, temperature

and molecular architecture. This generalized model combines the continuum and molecular approaches.

In energetic approaches, yielding is considered to be a thermally activated shear stress induced phenomenon. Important properties of the material are the activation energy, ΔH and activation volume, ν:

$$\Delta H = \frac{\nu}{2}\left(\frac{T\sigma_{yo} - T_o\sigma_y}{T - T_o}\right) \tag{4.8}$$

$$\nu = \frac{2RT}{\sigma_y - \sigma_{yo}} \ln\left(\frac{\dot{\varepsilon}}{\dot{\varepsilon}_o}\right) \tag{4.9}$$

where R is the gas constant, T is the temperature, and the subscript "o" indicates the value in a reference state (see, for example,[53]). Here, σ_y indicates the yield stress, not the stress in the y-direction as in equation 4.1.

The present study focuses on the yield criteria developed by Caddell et al.[35] for anisotropic pressure dependent materials. Under isotropic conditions, the model reduces to the modified von Mises criterion, which has been found to describe the effect of stress state on the yield response of many polymeric materials. This model is chosen since the material under investigation is oriented from the extrusion process and the generalization that the Caddell model provides is also of practical value in terms of application to other materials. In this chapter, the Caddell model is extended in order to determine the effects of temperature and strain rate through an energetic criterion. Therefore, a continuum level and a molecular level criterion are combined.

The model predictions are then compared with the yield strength data presented in Chapters 2 and 3.

4.2 Combination of Continuum Level and Thermal Activation Approaches

The present analysis begins with the continuum level yield criterion developed by Caddell et al.[54] for anisotropic and pressure dependent materials. For the present case of a transversely isotropic material loaded in 2 principal directions, equation 4.1 can be rewritten in the following form using cylindrical coordinates:

$$\left(\sigma_z^{\,2} - \sigma_z\sigma_\theta\right)\left(\frac{1}{C_z T_z}\right) + \sigma_z\left(\frac{C_z - T_z}{C_z T_z}\right) + \sigma_\theta\left(\frac{C_\theta - T_\theta}{C_\theta T_\theta}\right) + \sigma_\theta^{\,2}\left(\frac{1}{C_\theta T_\theta}\right) - 1 = 0 \qquad (4.10)$$

where the z-axis is along the direction of orientation and θ is the circumferential direction. Note that both C_i and T_i are temperature and rate dependent.

Axial and circumferential stress data from the biaxial tests at different temperatures and rates are plotted in Figures 3.4 and 3.9. Using equation 4.10, a non-linear minimization is performed with the data from all stress states in order to determine the best-fit values for the uniaxial tensile and compressive strengths in the principal directions. This is done for each rate and temperature and is used to develop the "reference state" curve (T_o=20°C and $\dot{\gamma}_o^{\,oct}$=0.05 min^{-1}). Therefore, this represents the continuum level approach in the present analysis.

As stated previously, in molecular level models important properties of the material are the activation energy, ΔH and activation volume, v. The best-fit uniaxial data is used to determine these values for the polyketone from the following equations:

$$\Delta H = \frac{\nu}{2}\left(\frac{T\sigma_{yo}^{u} - T_o\sigma_y^{u}}{T - T_o}\right) \tag{4.11}$$

$$\nu = \frac{2RT}{\sigma_y^{u} - \sigma_{yo}^{u}} ln\left(\frac{\dot{\varepsilon}}{\dot{\varepsilon}_o}\right) \tag{4.12}$$

These equations are similar to equations 4.8 and 4.9. Again, R is the gas constant, T is the temperature, and the subscript "o" indicates the value in a reference state. Reference state conditions are T_o=20°C and $\dot{\gamma}_o^{oct}$=0.05 min^{-1} in this study. Here, σ_y^{u} refers to the uniaxial yield stress in a principal direction, not the stress in the y-direction as in equation 4.1. The factor of 2 results from writing the equations in terms of uniaxial rather than shear stresses ($\tau_y = \sigma_y/2$). The results obtained using the best-fit uniaxial strength values are presented in Table 4.1. Using these values, the values for activation energy and activation volume for the cases of axial tension, hoop tension, and axial compression were calculated. The calculated activation parameters are listed in Table 4.1. Once the values for ν and ΔH have been calculated, they can be utilized as "shift factors" for a yield locus to predict the biaxial yield strengths at different rates or temperatures, as described below.

The absolute values of stress are typically used in determining the activation energy and volume. However, in order to achieve the appropriately signed value of shift in the case of axial compression, the negative value for the activation volume was used in the following analysis. This is due to the convention of indicating tensile stresses as positive and compressive stresses as negative in value.

The modeling procedure begins with the use of the continuum model in the form of equation 4.10. Next, best-fit data from the continuum level model are used in determining the thermal activation parameters. Continuing with the molecular level contribution, rearranging equation 4.12 we have:

$$\sigma_y^u = \sigma_{yo}^u + \frac{2RT}{v} \ln \frac{\dot{\varepsilon}}{\dot{\varepsilon}_o} \tag{4.13}$$

The second term on the right side of the equation is the shift in the principal yield stress as a function of strain rate for the case of uniaxial loading in that principal direction. As the stress state is changed, from uniaxial to biaxial, the value of the principal strength at yield also changes. It is assumed that the value for the shift changes in proportion with the percent change in principal yield strength as the stress state changes. This is corrected for as follows:

$$\sigma_y = \sigma_{yo} + \left(\frac{2RT}{v} \ln \frac{\dot{\varepsilon}}{\dot{\varepsilon}_o} \right) \frac{\sigma_{yo}}{\sigma_{yo}^u} \tag{4.14}$$

Since biaxial stress states are now considered, the stress values σ_y and σ_{yo} in the above equation are the yield strength in a principal direction, but not necessarily a uniaxial yield strength. Therefore, the superscript "u" has been removed (with the exception of the normalizing term). This type of normalization also ensures that the ratio of stresses, and thus the stress state, will not change due to the shifting procedure.

For the case of constant rate but changing temperature, equation 4.10 may be rearranged to produce:

$$\sigma_y^u = \left[\frac{\sigma_{yo}^u}{T_o} + \frac{2 \cdot \Delta H}{v} \left(\frac{T_o - T}{T_o T} \right) \right] T \tag{4.15}$$

This equation represents the case of uniaxial loading in a principal direction. To account for the change in yield stress with stress state, it is rewritten as:

$$\sigma_y = \left[\frac{\sigma_{yo}}{T_o} + \frac{2 \cdot \Delta H}{\nu} \left(\frac{T_o - T}{T_o T} \right) \frac{\sigma_{yo}}{\sigma_{yo}^u} \right] T \tag{4.16}$$

Again, the superscript "u" has been removed from the equation, with the exception of the normalizing term. Equations 4.14 and 4.16 can then be combined into one equation for the yield stress as a function of rate and temperature:

$$\sigma_y = \sigma_{yo} \frac{T}{T_o} + \frac{2}{\nu} \frac{\sigma_{yo}}{\sigma_{yo}^u} \left[RT \ln \frac{\dot{\varepsilon}}{\dot{\varepsilon}_o} + \Delta H \left(1 - \frac{T}{T_o} \right) \right] \tag{4.17}$$

Because the testing for this thesis is performed at a constant nominal octahedral shear strain rate, equation 4.17 is rewritten in terms of this. The factor for converting axial strain rate to octahedral shear strain rate cancels out of the equation. Conversion from axial stress to octahedral shear stress could also be made easily, but since data presented in this thesis is plotted as principal stresses such a conversion was not made. The final form used in the present analysis is:

$$\sigma_y = \sigma_{yo} \frac{T}{T_o} + \frac{2}{\nu} \frac{\sigma_{yo}}{\sigma_{yo}^u} \left[RT \ln \frac{\dot{\gamma}^{oct}}{\dot{\gamma}_o^{oct}} + \Delta H \left(1 - \frac{T}{T_o} \right) \right] \tag{4.18}$$

This equation describes a linear relation between the shifted yield stress and temperature. The relation between the shifted yield stress and the natural log of the octahedral shear strain rate is also linear.

4.3 Comparison of Model Predictions and Experimental Results

Using the "best fit" values for the principal tensile and compressive strengths (Table 4.1) at T_o=20°C and a rate of $\dot{\gamma}_o^{oct}$=0.05min^{-1} along with equation 4.10, a yield locus curve is constructed (Figure 4.1). This curve is then shifted according to equation 4.18 to predict the yield locus for different rates and temperatures. A comparison of the model predictions with experimental data is shown in Figures 4.2 and 4.3. The model appears to predict the biaxial yield strengths quite well.

The experimental data show that perhaps the effect of temperature is more pronounced in the axial direction, and also that the effect of rate is greater in the circumferential direction (as mentioned in Chapter 3). The model does not predict this trend. According to model results, the effects of rate and temperature are nearly equal for axial and circumferential tension, and greatest for the case of axial compression.

Because this model utilizes only uniaxial strength values, and the activation energy and volume as determined from uniaxial data, it may be possible to predict the yield locus of many different polymers quite readily. Different yield criteria could be used to form the "reference" yield locus, and because the shifting equations are general, the model could be applicable to isotropic or pressure independent materials as well. Experimental support for this is not pursued in this study. In the current study, the loading directions are coincident with the principal directions of anisotropy. However, this does not have to be the case. Transformation formulas could be applied if loaded in different directions.

Since the samples do not indicate significant anisotropy, it is questioned whether or not an anisotropic model is necessary. To answer this question, a model for isotropic, pressure-dependent materials[55] is used to predict the axial and circumferential stress at yield based on the best-fit uniaxial data obtained in a manner similar to that used for the anisotropic model. With the isotropic model, the best-fit tensile and compressive yield strengths are 52.7 MPa and 61.1 MPa, respectively. This data is plotted with the experimental data and the anisotropic model predictions at the reference state conditions in Figure 4.4. From this it is determined that the anisotropic model is indeed the appropriate one for this case.

	Axial Tension	Hoop Tension	Axial Compression
Yield Strength at 20°C, 0.05 min^{-1} (MPa)	55.3	49.3	61.2
Yield Strength at 50°C (MPa)	46.9	39.6	45.4
Yield Strength at 80°C (MPa)	39.9	36.8	42.5
Yield Strength at 20°C, 0.005 min^{-1} (MPa)	55.2	47.1	62.2
Yield Strength at 20°C, 0.5 min^{-1} (MPa)	59.9	54.3	67.1
Activation Energy (kJ/mol/s)	316	453	422
Activation Volume (m^3/mol/s)	4.70×10^{-3}	7.11×10^{-3}	4.59×10^{-3}

Table 4.1: Best-fit uniaxial strength values and activation parameters calculated there from.

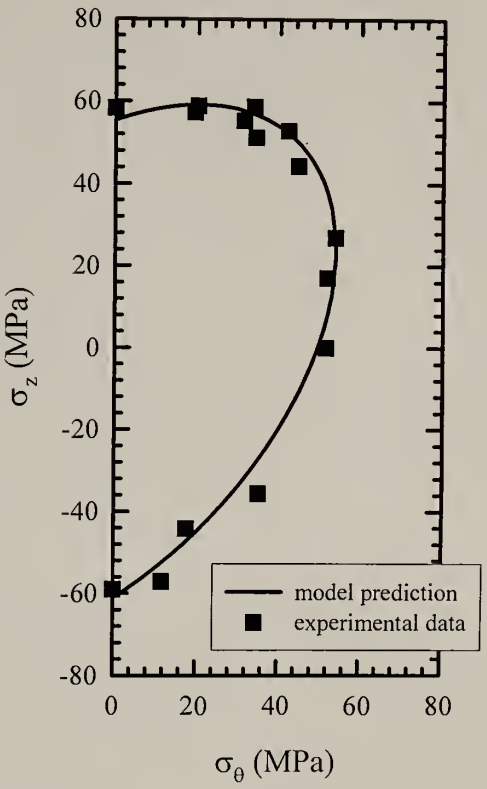

Figure 4.1: Yield locus curve constructed with best-fit uniaxial strength values from Table 4.1.

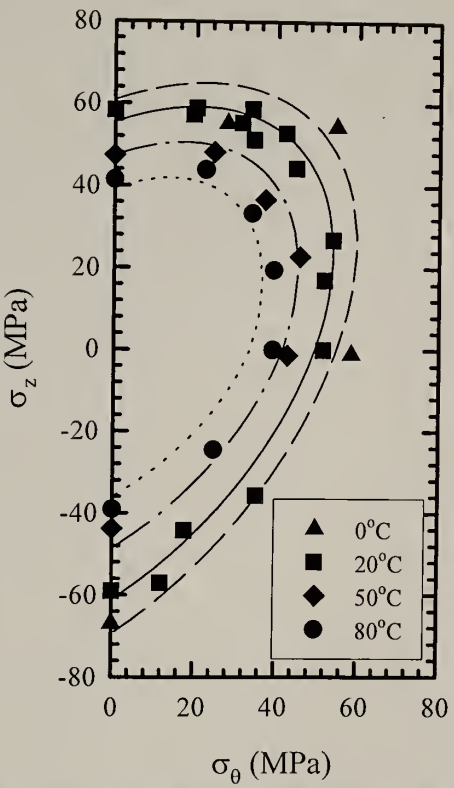

Figure 4.2: Yield locus curves shifted for temperature according to activation parameters from Table 4.1. Symbols represent experimental data and lines represent model predictions.

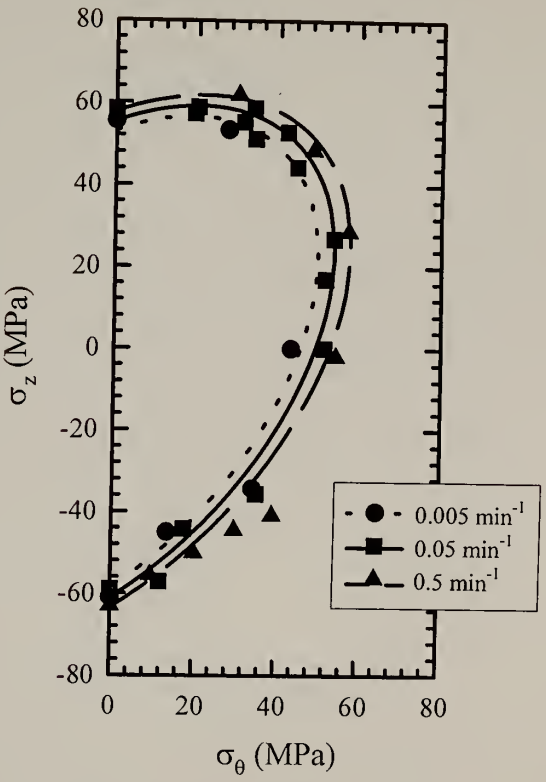

Figure 4.3: Yield locus curves shifted for octahedral shear strain rate according to activation parameters from Table 4.1. Symbols represent experimental data and lines represent model predictions.

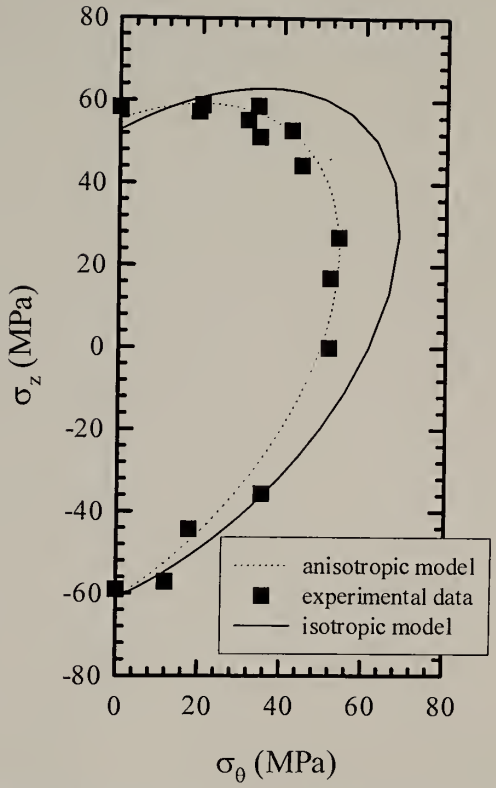

Figure 4.4: Comparison of experimental data with isotropic[55] and anisotropic[35] pressure-dependent yield models.

CHAPTER 5

EFFECT OF PROCESSING CONDITIONS

5.1 Background

It is well known that processing conditions can influence the final properties of polymers. Shear stress, crystallization temperature, cooling rate, etc. are all relevant to the properties of the end product. Such processing parameters can influence, for example, the degree of orientation, impart residual stresses, and alter the degree of crystallinity. These physical changes can, in turn, affect the yield strength, stiffness, ductile-to-brittle transition, fracture toughness and so on. These issues become extremely important for materials that are sensitive to processing conditions. Slight changes in mold conditions or part design can have detrimental effects on the part performance. In this chapter, we present the effects that alterations in the extrusion shear rate and thermal history have on the yield and failure mode of the aliphatic polyketone terpolymer.

It has been found in various studies that the shear rate is one processing parameter that can dramatically influence the properties and behavior of a material. In an injection molding study conducted on polyethylene terepthalate (PET)[56], as the injection speed is increased, the tensile and flexural strengths are found to decrease. However, the effect on the crystallinity and modulus is not clear. It is also known that shear stress can increase crystallization kinetics[57], and induce preferred orientation during

crystallization. Extremely high shear rates can also lead to degradation of the polymer. These effects can certainly influence the final material behavior.

Similarly, the thermal history can significantly affect the properties of polymers through its effect on the crystalline structure and free volume. In the same study by Mathew[56], it is found that increasing cooling rate leads to an increase in the yield and flexural strength of PET. A separate study[58] on isotactic polypropylene (iPP) also shows that increasing cooling rate leads to increased yield strength as well as increased elongation at break. Additionally, the ductile-to-brittle transition temperature is found to decrease with increasing cooling rate. Note that the method used to measure this transition is not clear. In this case, the modulus is reported to change only slightly, though the trend is to increase. A more recent study of polypropylene (PP)[59] also finds that increases in cooling rate lead to increased yield strength and more ductile behavior. On the other hand, in this study of PP the modulus is found to increase initially and then decrease with increasing cooling rate.

It is of interest to relate changes in behavior to structural changes within the polymer. In the study by Greco[58], the increases in yield strength and elongation at break are accompanied by decreases in lamellar thickness and spherulite diameter. Earlier work on polyethylene[60] indicates an increase in impact strength with cooling rate, which is connected to a decrease in spherulite size. In contrast, a separate study[61] on the effect of nylon 66 spherulite size, altered by the addition of a nucleating agent, finds that variation in spherulite size affects neither the impact, hardness, fatigue, nor creep properties. The decrease in spherulite size is found to increase the yield strength and

modulus and decrease the percent elongation. These results are found not to be a result of foreign particles alone.

In other studies[62,63], increases in impact strength with cooling rate of polycarbonate have been linked with residual stresses. These stresses may be induced during processing due to the inability of the material to contract while cooling and are independent of induced orientations. While residual compressive stresses have been found to increase toughness, residual tensile stresses are believed to promote brittle failures.

With regard to the specific polymer which is investigated here, it has previously been determined that the cooling procedure used during processing can affect properties. This has been found for barrier properties[64] and speculated to be related to changes in crystallinity and crystal size[22]. It is therefore expected that differences in properties due to cooling rate may also be detected in this study as well.

The purpose of this portion of work is to examine the effects that various extrusion conditions have on the yield and failure response of an aliphatic polyketone terpolymer. Testing is again performed under biaxial loading conditions in order to elucidate the effect of stress state. Additionally, physical characterization of the different samples is performed in order to link these effects to morphological changes and residual stresses resulting from the process conditions.

5.2 Material

The chemical formula for this aliphatic polyketone is the same as has been described in Chapter 2 and as shown in Figure 1.1 with R=propyl. However, the

processing conditions have been altered for this portion of the study. Five separate samples are prepared under different extrusion condition. As a basis for comparison, the first sample is extruded under "standard" conditions, i.e., conditions typical for this material. This material is designated as the "moderate shear rate, moderate cooling rate" (MSMC) sample and is the material discussed in the earlier chapters. Two samples are processed at either a higher or lower extrusion rate than the MSMC sample. These materials are designated as "high shear rate, moderate cooling rate" (HSMC) and "low shear rate, moderate cooling rate" (LSMC) samples. The final two samples are cooled at rates higher and lower than the standard and are designated as the "moderate shear rate, high cooling rate" (MSHC) and "moderate shear rate, low cooling rate" (MSLC) samples. Due to proprietary reasons, further details about the processing conditions were not provided by the manufacturer. However, the conditions represent practical limits over which this material can be processed, therefore resulting in the range of properties most likely to be observed in commercial applications.

The initial intent was to extrapolate process conditions and thereby the morphology of the MSMC material with the morphologies of the additional four samples, however, it will later be shown that this was not the case. This was likely due to the fact that the MSMC material was processed at a different site than the other four samples. Accordingly, other variations beyond processing parameters were likely. It is important to keep this in mind when comparing the samples in this chapter.

5.3 Experimental

5.3.1 Biaxial Testing

The sample preparation and testing procedures are the same as is described in Chapter 2. Again, compliance values are determined for each sample using the method described in Chapter 2.3.3. These values, presented in Table 5.1, are used in the strain and strain rate calculations.

5.3.2 Crystallinity

In order to determine the crystallinity of the materials, calorimetry work is performed. This is carried out in a DuPont 2910 DSC at a scanning rate of 10°C/min. Calculations are based on a crystalline heat of fusion of 227 J/g[65]. In another set of experiments, DSC scans are run on the MSLC and MSHC samples at a heating rate of 2°C/min.

The densities of the materials are determined via density gradient column consisting of carbon tetrachloride and heptane. The density values are then used as a second means of determining the crystallinity of the samples by utilizing the following equations:

$$\phi_v = \frac{\rho_s - \rho_a}{\rho_c - \rho_a} \tag{5.1}$$

$$\phi_m = \frac{\rho_c}{\rho_s}\phi_v \tag{5.2}$$

where ϕ_v and ϕ_m are the percent crystallinity by volume and mass, respectively, and ρ_s, ρ_a and ρ_c are the density values of the sample, amorphous phase and crystalline phase,

respectively. Values for ρ_a and ρ_c are taken from Lommerts et al.[66] (ρ_a = 1.21 g/cm^3, ρ_c = 1.297 g/cm^3). The value of the crystalline density is for the β crystalline phase of the polyketone, as this is the dominant crystal phase for the terpolymer [40,66,67].

5.3.3 Crystalline Orientation

Wide-angle X-ray diffraction (WAXD) is used in determination of crystalline orientation in the as-received samples. Pinhole collimated monochromatic CuK_α radiation is used. Patterns are collected on a Brucker GADDS detection system.

5.3.4 Overall Orientation

Attenuated total reflection infrared (ATR-IR) spectroscopy is also used to characterize sample orientation. A Perkins Elmer System 2000 FT-IR instrument is used with a KRS crystal. The polarization is maintained in the vertical position, and spectra are obtained with the sample axial direction oriented parallel and perpendicular to the polarizer direction. Because all samples have rounded surfaces, sections with flat surfaces must be cut. This is done with an optical microtome on samples that are chilled with liquid nitrogen. The direction of the cut is parallel with the extrusion direction. The peak height value at 1690 cm^{-1} is recorded in both parallel and perpendicular orientations. This peak corresponds to the carbonyl stretching band[68] and therefore corresponds to a vibration perpendicular to the chain. The value for the average angle between the extrusion direction and local molecular chain axis, θ, is calculated for each sample from the orientation function, f:

$$f = \frac{3\langle \cos^2 \theta \rangle - 1}{2} \tag{5.3}$$

and also:

$$f = \frac{(R-1)(R_o+2)}{(R+2)(R_o-1)} \tag{5.4}$$

where R is the dichroic ratio of the absorbance values with parallel and perpendicular sample orientation, $A_{\parallel}$ and $A_{\perp}$ respectively:

$$R = \frac{A_{\parallel}}{A_{\perp}} \tag{5.5}$$

and R_o is the dichroic ratio for perfect uniaxial order:

$$R_o = 2\cot^2 \phi. \tag{5.6}$$

In the equation above, ϕ is the angle between the chain axis and the transition moment of the vibration that is under consideration. See, for example, Koenig[69]. For the analysis performed here, it is assumed that the transition moment of the carbonyl stretching band is 90° to the chain axis. Therefore, R_o is approximated to be zero.

5.3.5 Spherulitic Structure

Scanning electron microscopy is carried out on a JEOL 35 SEM at 20kV. To prepare samples, sections are cut from the hollow cylinders in a manner that allows examination of the spherulitic structure along the length of the cylinder as well as through the wall thickness. This surface is indicated in Figure 5.1. The desired surface is then cut smooth on a Reichert ultracut FC4 cryo-microtome utilizing liquid nitrogen as the cooling fluid. To provide topographical contrast, the samples are etched in a

potassium permanganate/phosphoric acid etch. This procedure was developed specifically for this polymer and is described in detail elsewhere[37]. The etched samples are then mounted and gold-coated in a Polaron ES100 sputter coater.

5.3.6 Thermal Transitions

Dynamic mechanical thermal analysis (DMTA) is carried out on a Rheometrics Mark IV DMTA. All tests are performed in single-cantilever bending mode at a frequency of 1 Hz and dynamic strain of 0.05%. Samples are cut from the cylindrical samples on a wafer saw with the cut direction parallel to the axial direction. Samples with thickness of ~2mm are used in order to minimize curvature in the specimens due to the cylindrical geometry. All samples were gripped to a torque value of 30 cm-N.

5.3.7 Residual Stresses

Residual stress calculations are made following a method described by Clutton and Williams[70]. The cylindrical samples are cut into sections of different lengths. Length-wise slices are removed from each section so that relaxation is able to occur. Because the glass transition temperature, T_g, of the material is close to room temperature, the samples are heated at 100°C for 1 hour to put the samples more significantly above the T_g and to allow relaxation to occur more rapidly. Measurement of the ring closure allows for the determination of the stresses present in the as-processed material, as described in the reference and as summarized here briefly. Following the model, measurements of the ring-closure, δ_0, plotted against a specimen dimension function,

F(βL), for each sample. These values are calculated from specimen dimensions and material properties as follows:

$$\delta_\theta = -\pi(D_o - D_f) \tag{5.7}$$

$$F(\beta L) = \frac{2[\cosh(\beta L) - \cos(\beta L)]}{\beta L[\sinh(\beta L) - \sin(\beta L)]} \tag{5.8}$$

$$\beta^4 = 12\frac{(1-\nu^2)}{D_o{}^2 h^2} \tag{5.9}$$

In the equations above, D_o is the initial diameter, D_f is the diameter after relaxation, L is the length of the cylinder, ν is Poisson's ratio and "t" is the cylinder wall thickness. The slope, m, and intercept, c, are determined for each of the plots. Values for residual stress are then calculated for each sample using the equations below:

$$\sigma_z = -\frac{Etm}{\pi\nu D_o{}^2} \tag{5.10}$$

$$\sigma_\theta = -\frac{Ehc}{\pi D_o{}^2} \tag{5.11}$$

where E is the tensile modulus. Note that this method assumes a linear stress profile in the material and the stresses determined are the residual stresses on the bore of the pipe specimen. This is an approximation of the actual stress distribution which allows for simplification of the analysis. The values for Poisson's ratio (0.40) and Young's modulus (1.40 GPa) are obtained from the previously performed standard tensile tests (ASTM D-638), which were carried out at 20°C at an extension rate of 50 mm/min (see Chapter 23.1).

5.4 Effect on Yield Strength

Figures 5.2 and 5.3 show the axial stress, σ_z, versus circumferential stress, σ_θ, data for all samples, allowing the direct comparison of the yield strength of samples processed under the various conditions. These biaxial test results indicate that the processing conditions- shear rate and cooling rate- have very little effect, if any, on the yield strength of the various samples. This was unexpected, as several other studies[56,58,59] have found increases in yield strength with increased cooling rate. In addition, increased shear rate is expected to result in greater level of axial orientation, causing increased strength in that direction.

5.5 Effect on Failure Behavior

Similar to the MSMC materials described in Chapter 2, the additional 4 materials display a range of ductility depending on the stress state, Figures 5.4-5.8. Again, the mode of failure is not clear from visual inspection. For this reason, the zero-slope condition in the octahedral shear stress versus volumetric strain curve is chosen as the criteria for ductile or brittle failure. Again, ductile failure is characterized by achievement of a slope value of zero in the volumetric strain versus octahedral shear stress curve and brittle failure is characterized as non-achievement. These stress/strain curves are plotted in Figures 5.9-5.13.

Using the above criteria, the yield locus of each material in Figures 5.4-5.8 is divided into the regions that result in ductile failures or brittle failures. The solid and hollow symbols represent ductile and brittle failures, respectively. Comparatively, the size and location of the brittle region for the high, moderate and low shear rate materials

are quite similar. Thus, the shear rate appears to have little effect on the ductile-brittle transition of this material. In contrast, the cooling rate dramatically influences the ductile-brittle behavior. As the cooling rate decreases, the size of the brittle regime significantly increases.

It is surprising to note that in all materials brittle failures occur in stress states that are essentially axial tension with a slight amount of internal pressure. In axial tension, ductility is clearly observed as illustrated by the formation of a necked region. Curiously, when the state of stress applied to a sample is the more demanding state of equi-biaxial tension, which is achieved with an even greater level of internal pressurization, ductile failures are observed in 4 of the 5 materials. This is contrary to what would be expected since this stress state results in the highest levels of volumetric strain, and would therefore be the most likely to produce a brittle response. In our study, the slowly cooled MSLC material is the only sample that displays brittle behavior in this stress state of equi-biaxial tension.

In order to explain the observed ductility under equi-biaxial loading and the increased brittle response of the MSLC material, morphological characterization was performed. Details are presented in the following section.

5.6 Morphological Characterization

5.6.1 Crystallinity

Crystallinity measurements are made via differential scanning calorimetry as well as density gradient column. DSC scans for the different extrusion rates are plotted in

Figure 5.14 and for the different cooling rates in Figure 5.15. Crystallinity and melt temperature data from DSC and density and crystallinity values calculated from density gradient column are presented in Table 5.2. The agreement between the crystallinity values determined from the two methods is quite good. No significant change in crystallinity between samples is detected, except perhaps a slightly higher value for LSMC.

From the DSC results, it is also noticed that there is no significant difference in T_m between the samples or in the shape or width of the melting peaks. Qualitatively, this indicates similar values for the lamellar thickness or crystalline perfection for the samples. These results indicate that alterations in either the extrusion or cooling rate have little effect on the crystalline phase of this material.

Since the mechanical behavior of this material does not change appreciably with change in shear rate, it is not surprising that few differences are observed. However, it might be expected that the crystallinity of a slowly cooled material be higher than a rapidly cooled sample. Similarly, the degree of crystalline perfection and lamellar thickness would be expected to be greater. To study this more closely, a second set of DSC runs was made on the MSLC and MSHC materials at a heating rate of 2°C/min, Figure 5.16. Again, no significant difference is found between the peaks or crystallinity values of the samples. In a previous study on this material, a cylindrical sample was ground into a powder, melt pressed and quenched in liquid nitrogen[67]. The degree of crystallinity for this sample was determined to be 31%, compared to 34% for a sample cut directly from the hollow cylinder. Thus, the quenching process does not greatly

affect the crystallinity of this material. Since the cooling conditions used in processing of the hollow cylinder samples are not expected to be as severe as this, it seems reasonable that no differences in crystallinity are observed here.

It might also be expected that more tie molecules would be present in the MSHC material than in the MSLC material. This would result in greater ductility in comparison with the MSLC material, as observed. However, increased numbers of tie molecules should also lead to greater strength, which is not observed. Also, considering the rapid crystallization kinetics of the material[42,71] and the fact that the crystallinity values for the MSLC and MSHC materials are equivalent, it is not expected that segregation is more complete in one sample than the other.

5.6.2 Crystalline Orientation

WAXD patterns were obtained for all samples in the "as-received" condition. The diffraction patterns for the samples extruded at different rates are presented in Figure 5.17. The diffraction patterns for the samples processed with different cooling rates are presented in Figure 5.18. No significant crystalline orientation is detected in any of the samples. These patterns are obtained with the beam direction through the thickness of the cylinder. Patterns with the beam along the axial and tangential directions, though not presented here, are similar. Also, patterns obtained on the outer "skin" layer indicate no crystalline orientation and appear similar to those in Figures 5.17 and 5.18.

For this material, the main diffraction peak is observed at $2\theta \sim 22^{o}$. The width of this peak for each sample is compared in Figures 5.19-20. It can be seen from these figures that the peak widths are essentially equivalent. This indicates that the relative

crystallite size for each sample is also equivalent. Thus, the WAXD results, similar to DSC, indicate that the process conditions have no measurable effect on the crystalline phase of this material.

It was expected that some variation in crystalline phase orientation would be observed between the samples processed at different shear rates. However, this was not the case. Apparently very little, if any, orientation was present in the samples when crystallization initiated. This may mean that very little orientation was developed during melt flow, an observation also made by others[72] in the case of isotactic polypropylene. In that study, wide-angle X-ray scattering was performed on static and flowing melts in order to observe the changes in the scattering patterns due to shear-induced orientation. However, no differences were found between the static and flowing melts, indicating no presence of shear-induced structure.

5.6.3 Overall Orientation

This material is approximately 65% amorphous and therefore the amorphous phase is expected to play a significant role in the material behavior. To account for the presence of and possible orientation of this phase, ATR-IR spectra are analyzed for each sample. While the phrase "amorphous orientation" may seem like an oxymoron, it is used within the context that "crystalline" suggests long-range order, and that the amorphous component may have orientation within short range. The spectra obtained for the samples oriented parallel and perpendicular to the polarization direction indicate several differences between samples. Figures 5.21-25 indicate the spectra for the five

samples. The carbonyl peak which is analyzed is indicated in Figure 5.21 (MSMC material).

From the peak height values, an average angle of chain orientation is calculated for each sample. This angle is relative to the extrusion direction. Results are presented in Table 5.3. The results indicate no significant level of orientation. The MSHC and HSMC samples show orientation angles closer to the extrusion direction, as would be expected. Since no crystalline orientation is observed from the WAXD results, the detected orientation is assumed to be in the amorphous phase. Again, the results do not give insight to the increase in the size of the brittle regime of the MSLC sample compared to the other samples. However, neglecting the MSMC material (as explained previously) it does appear that the higher cooling rates and shear rates tend to preferentially orient the amorphous regions toward the axial direction.

5.6.4 Spherulitic Structure

Electron micrographs for the MSMC, MSLC and MSHC materials are presented in Figure 5.26. It is clear that the spherulite size in the MSMC material is much larger than in the other materials. This had originally been unexpected, as the morphology of this material was expected to be bound by the MSLC and MSHC materials. This is explained by the fact that the MSMC material was processed at a separate location and time than the other 4 samples, as described previously. Therefore, other variables may be affecting the morphology (different polymer batch, stabilizer package, etc.). Because of this, it is not accurate to include this material in the comparison of the effects of

processing conditions on the morphology of the aliphatic polyketone. It is, however, still possible to compare the remaining four samples.

Figure 5.27 indicates the micrographs for the MSLC, MSHC, HSMC and LSMC materials at the same magnification. From these, a difference in the MSLC morphology is identified. In this case, the spherulitic structure is rather distinct, allowing one to more readily identify individual spherulites than for the remaining three materials. In the case of the latter, the spherulitic structure appears to be highly tangled or intertwined, making identification of individual spherulites more difficult. This could be partly responsible for the observed brittle behavior of the MSLC material.

5.6.5 Thermal Transitions

As described previously, reported values for glass transition temperature for this material are in the 10-15°C range[18,65]. Because testing at 20°C is only slightly above this reported value, slight changes in the actual T_g value could impact the material behavior. Therefore, it is questioned if the processing conditions could affect this transition value or not. To determine if this is a factor in the brittle behavior of the MSLC material dynamic mechanical thermal analysis (DMTA) is performed. Representative plots of tan δ as a function of temperature are shown in Figures 5.28 and 5.29. Others[38] have assigned the peaks at ~180, 40, and -80°C as the α,β, and γ transitions. The β transition is the glass transition. Glass transition temperatures are tabulated in Table 5.4. From these results it is clear that T_g for these materials is higher than the reported values. It is also observed that the transition is rather broad, spanning

roughly a 50°C temperature range. This is significant since testing was performed within this transition region at 20°C- within this transition region.

It was expected that the more brittle MSLC material would have a slightly higher T_g than the other materials. However, within statistical error, the samples all appear to have similar T_g values, Figure 5.30. Therefore, this transition probably had little effect on the difference in behavior of the samples.

5.6.6 Residual Stresses

The data used in calculating the residual stress values are plotted in Figures 5.31 and 5.32. The residual stress values for each sample are presented in Table 5.5. Note that these are tensile rather than compressive stresses, which would be negative values. For all samples, the residual stress in the circumferential direction is significant, whereas the residual stress in the axial direction is quite low. As would be expected, the level of residual stress is greater in the rapidly cooled MSHC material than in the slowly cooled MSLC material. There is no significant change in residual stress with extrusion rate.

During testing, the applied stresses are superposed upon the existing residual stresses. Therefore, the actual stress state is the combined effect of residual and applied stresses. While Figures 5.2 and 5.3 indicate only the applied stresses, Figures 5.33 and 5.34 indicate the effect of shifting our data to include the calculated residual stresses. Again, the dashed line indicates the condition of equibiaxial tension, for which brittle behavior was expected but for which ductile behavior was observed. It is observed that, after this adjustment, the failures that are determined to be brittle do indeed correspond to equi-biaxial tension (and stress states about this one) as is expected. Thus, the

observed brittle behavior in less demanding applied stress states appears to be accounted for as a result of residual stresses.

5.7 Summary

Multi-axial testing was performed on hollow cylindrical samples of an aliphatic polyketone terpolymer that had been extruded with different shear and cooling rates. The morphological characteristics looked at include crystallinity, lamellar thickness, crystalline orientation, overall orientation, morphology and glass transition temperature. The effects of shear rate on the mechanical behavior and morphological characteristics are negligible. The cooling rate, on the other hand, has significant effect on the yield behavior of this material. The slowly cooled material displays more brittle behavior than the standard or rapidly cooled sample. While no significant changes in the crystalline phase or glass transition temperature with cooling rate are detected by the techniques used, a more defined spherultic structure is observed for the sample cooled at a lower rate.

Ductile behavior was observed for the loading condition of equibiaxial tension for all samples but the slowly cooled material. This is in contrast to what was expected, since this stress state is the most demanding. The observation seems to be explained by the presence of residual stresses, which effectively shift the stress state felt by the material.

	MSMC	HSMC	LSMC	MSLC	MSHC
C_{rr} (MPa)	3977	3081	2597	3531	2713
C_{rz} (MPa)	1502	1310	1122	1391	1096
$C_{r\theta}$ (MPa)	212	18	58	53	68
C_{zz} (MPa)	2895	2871	2672	2529	2247
S_{rr} (MPa^{-1})	3.23×10^{-4}	4.26×10^{-4}	4.89×10^{-4}	3.87×10^{-4}	4.81×10^{-4}
S_{rz} (MPa^{-1})	-1.97×10^{-4}	-2.40×10^{-4}	-2.45×10^{-4}	-2.68×10^{-4}	-2.85×10^{-4}
$S_{r\theta}$ (MPa^{-1})	5.72×10^{-5}	9.95×10^{-5}	9.52×10^{-5}	9.97×10^{-5}	1.03×10^{-4}
S_{zz} (MPa^{-1})	5.50×10^{-5}	5.67×10^{-5}	5.80×10^{-4}	6.90×10^{-4}	7.23×10^{-4}

Table 5.1: Stiffness (C) and compliance (S) values determined for samples processed under different conditions.

Sample	Density (g/cm^3)	T_m (°C)	Crystallinity			
			DSC (mass%)		density column (volume %)	density column (mass %)
			10°C/min	2°C/min		
MSMC	1.240	225	34	-	34	37
HSMC	1.240	224	33	-	34	37
LSMC	1.240	224	35	-	36	38
MSLC	1.240	223	33	38	34	37
MSHC	1.240	223	33	39	34	37

Table 5.2: DSC and density gradient column data for hollow cylinder samples processed under different conditions.

Sample	Orientation Angle (degrees)
MSMC	46
HSMC	37
LSMC	45
MSLC	44
MSHC	35

Table 5.3: Orientation angles as determined from ATR-IR spectra.

Sample	Mean T_g (^oC)
MSMC	32.3
HSMC	34.8
LSMC	31.4
MSLC	38.0
MSHC	36.4

Table 5.4: Mean T_g values determined by DMTA.

Sample	Circumferential Stress (MPa)	Axial Stress (MPa)
MSMC	15.7	1.7
HSMC	16.9	0.2
LSMC	16.5	0.5
MSLC	16.8	0.6
MSHC	18.6	0.8

Table 5.5: Residual stress values calculated for each sample.

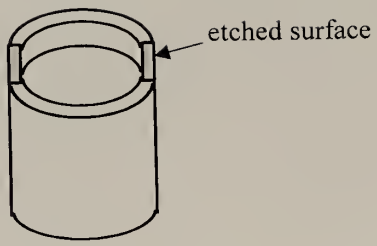

Figure 5.1: Schematic of surface that is microtomed and etched for examination with SEM.

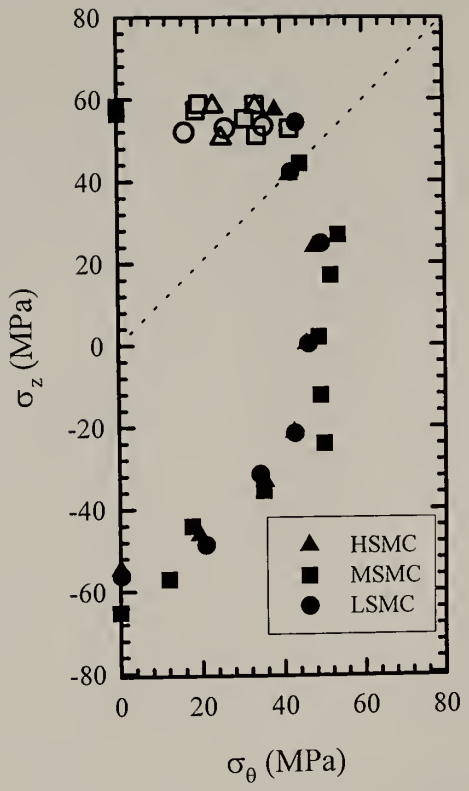

Figure 5.2: Circumferential stress, σ_θ, versus axial stress, σ_z, for material extruded at various shear rates.

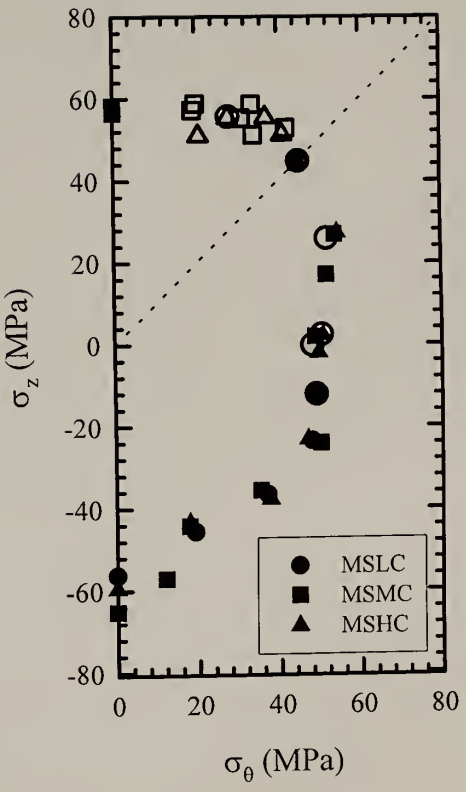

Figure 5.3: Circumferential stress, σ_θ, versus axial stress, σ_z, for material extruded at various cooling rates.

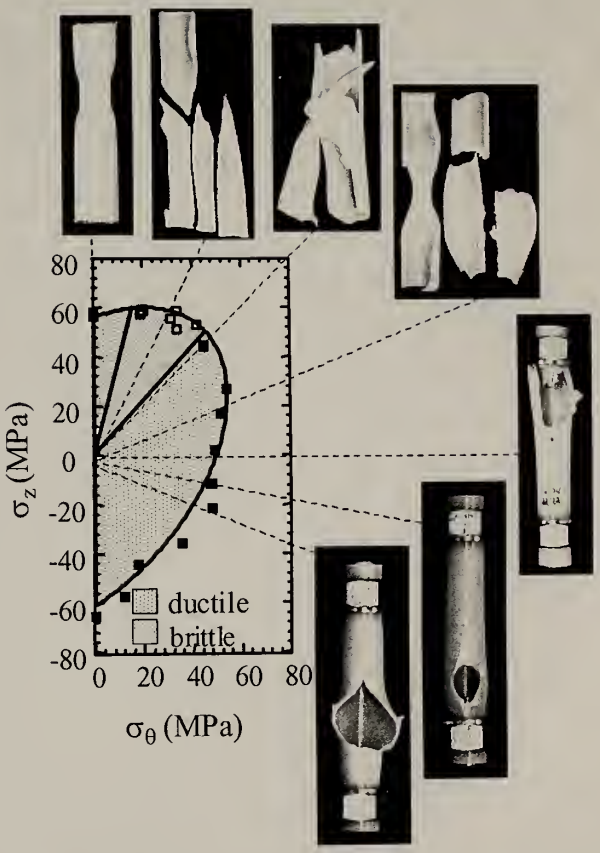

Figure 5.4: Schematic of circumferential stress, σ_θ, versus axial stress, σ_z, for MSMC material with images of failed specimens for the corresponding loading paths. Ductile and brittle regions are indicated by the different shadings. Solid and hollow symbols represent ductile and brittle failures, respectively.

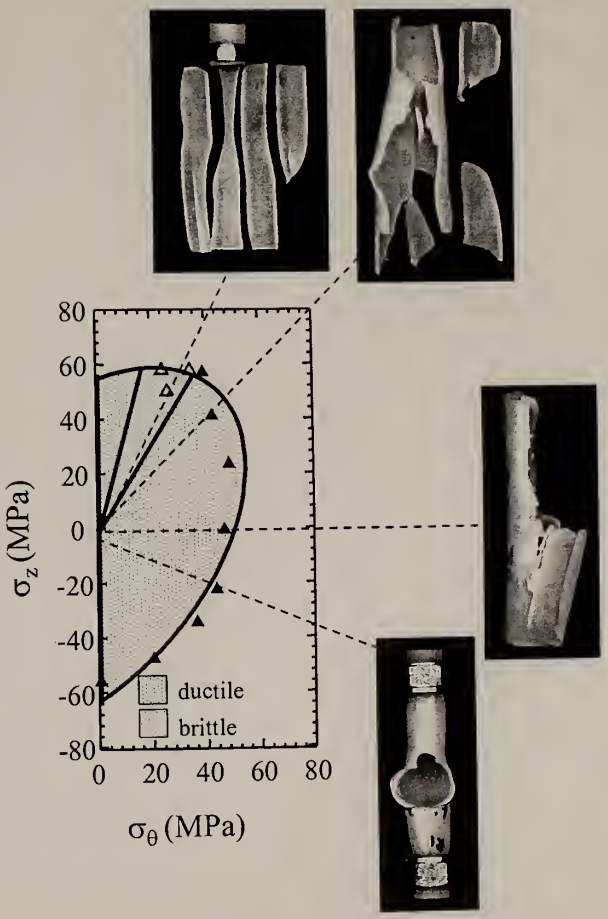

Figure 5.5: Schematic of circumferential stress, σ_θ, versus axial stress, σ_z, for HSMC material with images of failed specimens for the corresponding loading paths. Ductile and brittle regions are indicated by the different shadings. Solid and hollow symbols represent ductile and brittle failures, respectively.

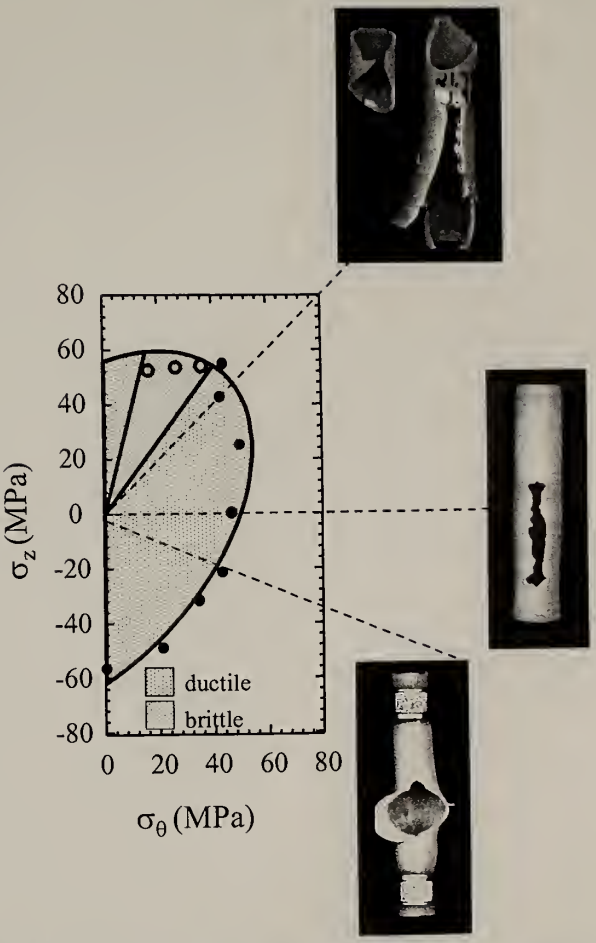

Figure 5.6: Schematic of circumferential stress, σ_θ, versus axial stress, σ_z, for LSMC material with images of failed specimens for the corresponding loading paths. Ductile and brittle regions are indicated by the different shadings. Solid and hollow symbols represent ductile and brittle failures, respectively.

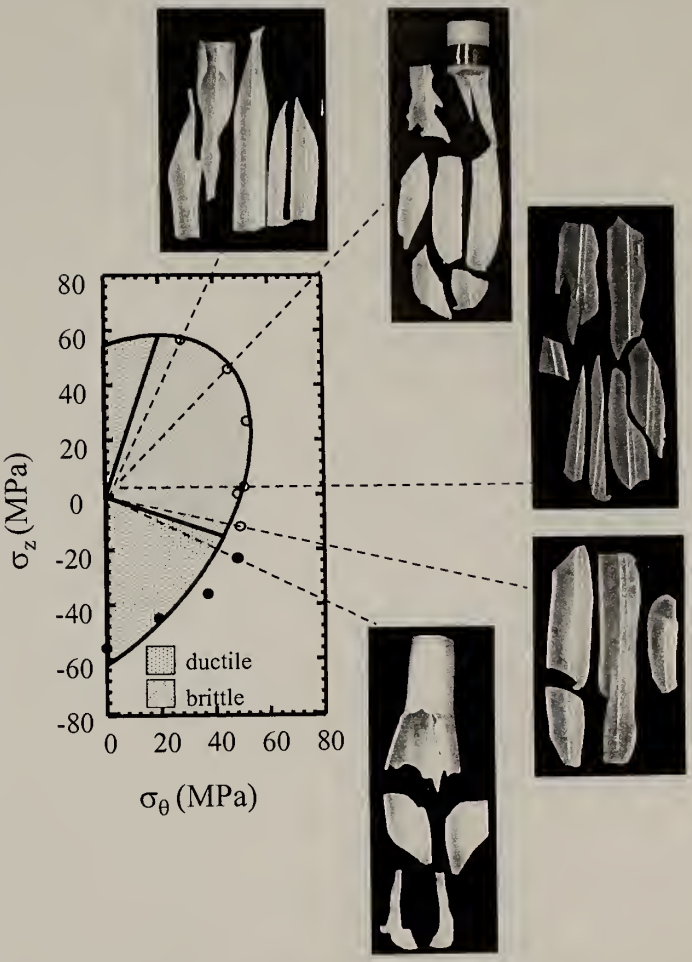

Figure 5.7: Schematic of circumferential stress, σ_θ, versus axial stress, σ_z, for MSLC material with images of failed specimens for the corresponding loading paths. Ductile and brittle regions are indicated by the different shadings. Solid and hollow symbols represent ductile and brittle failures, respectively.

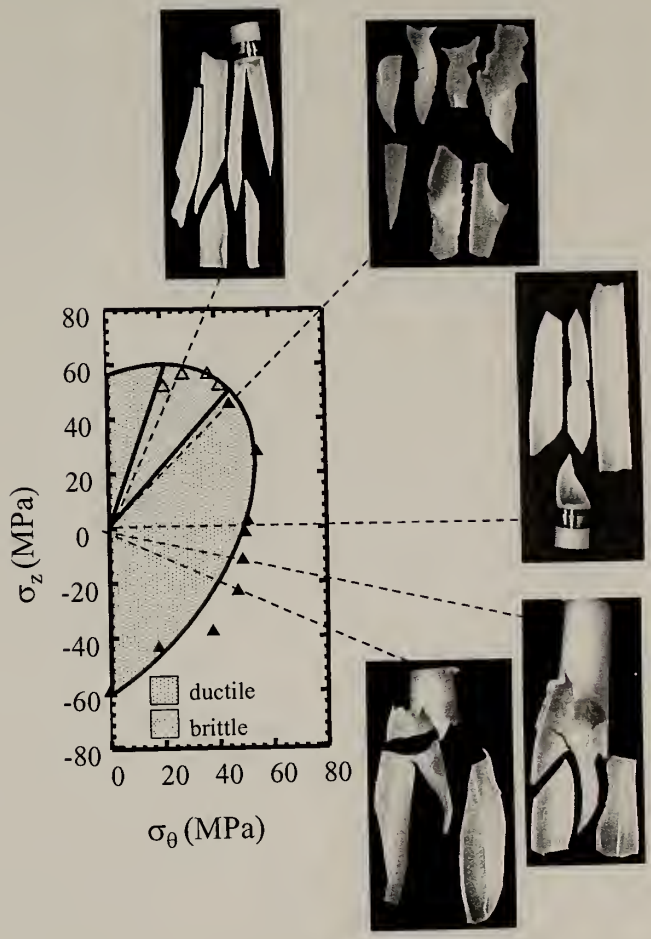

Figure 5.8: Schematic of circumferential stress, σ_θ, versus axial stress, σ_z, for MSHC material with images of failed specimens for the corresponding loading paths. Ductile and brittle regions are indicated by the different shadings. Solid and hollow symbols represent ductile and brittle failures, respectively.

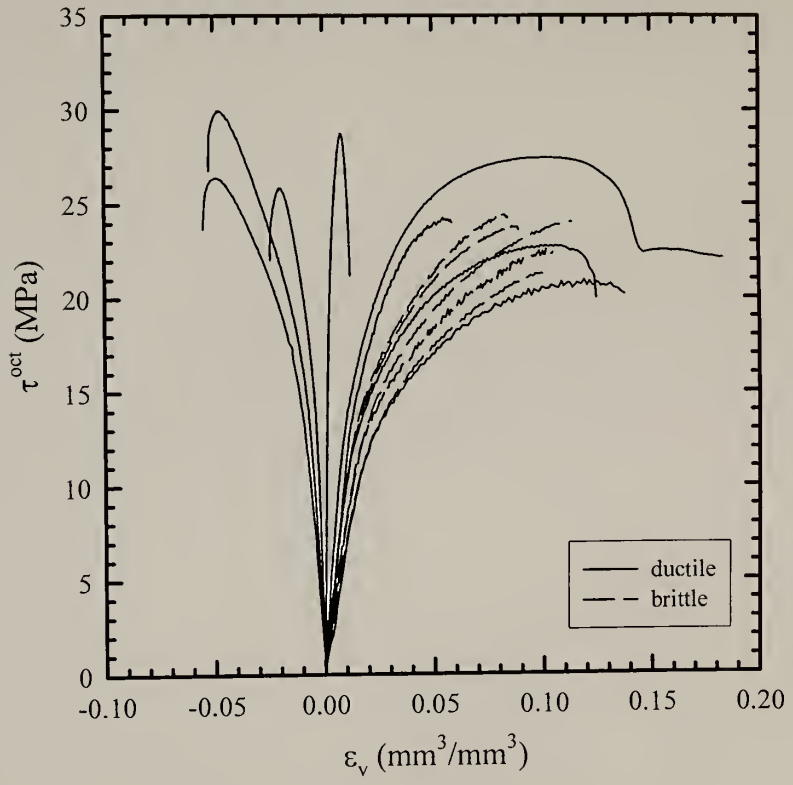

Figure 5.9: Octahedral shear stress, τ^{oct}, versus volumetric strain, ε_v, for MSMC material tested at 20°C and a nominal octahedral shear strain rate of 0.05 min^{-1}.

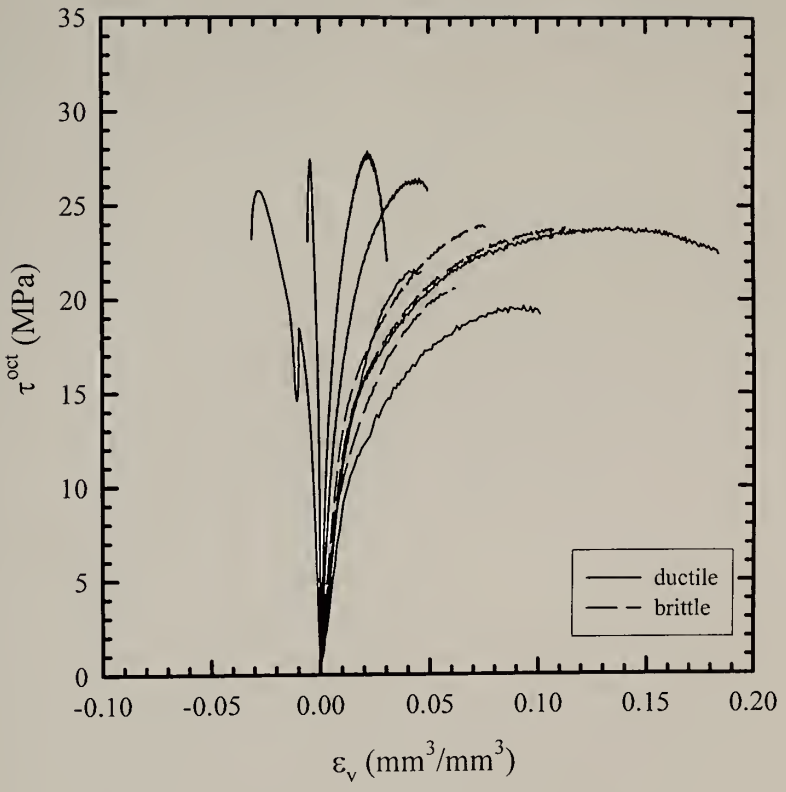

Figure 5.10: Octahedral shear stress, τ^{oct}, versus volumetric strain, ε_v, for HSMC material tested at 20°C and a nominal octahedral shear strain rates of 0.05 min^{-1}.

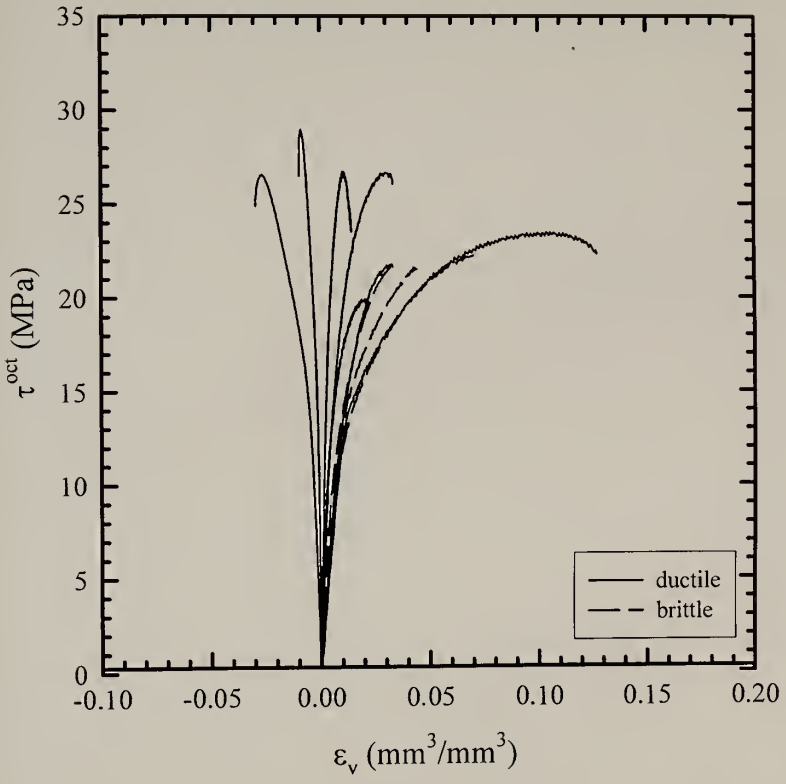

Figure 5.11: Octahedral shear stress, τ^{oct}, versus volumetric strain, ε_v, for LSMC material tested at 20°C and a nominal octahedral shear strain rate of 0.05 min^{-1}.

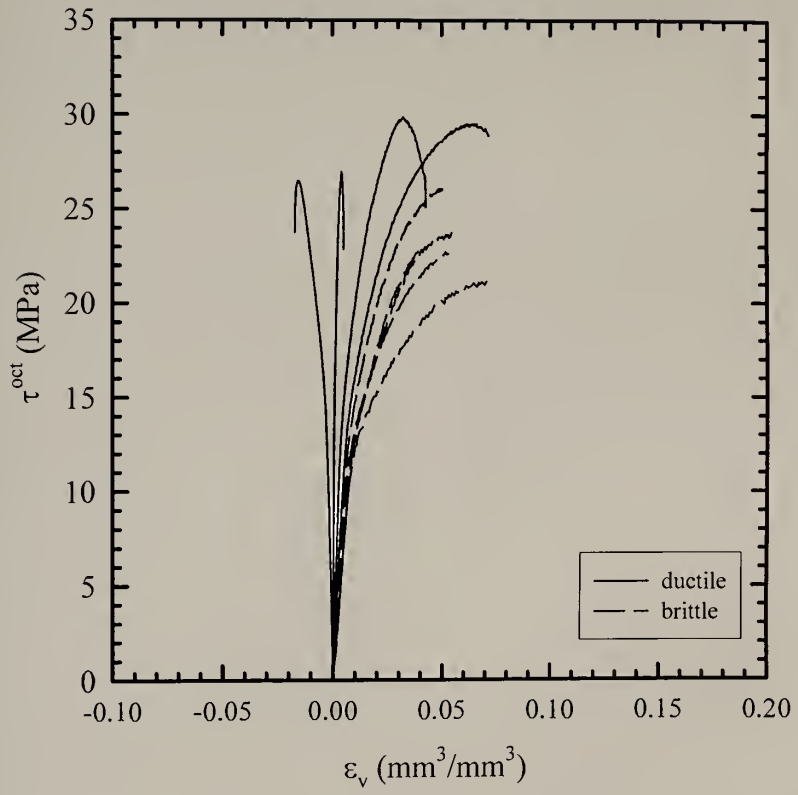

Figure 5.12: Octahedral shear stress, τ^{oct}, versus volumetric strain, ε_v, for MSLC material tested at 20°C and a nominal octahedral shear strain rate of 0.05 min^{-1}.

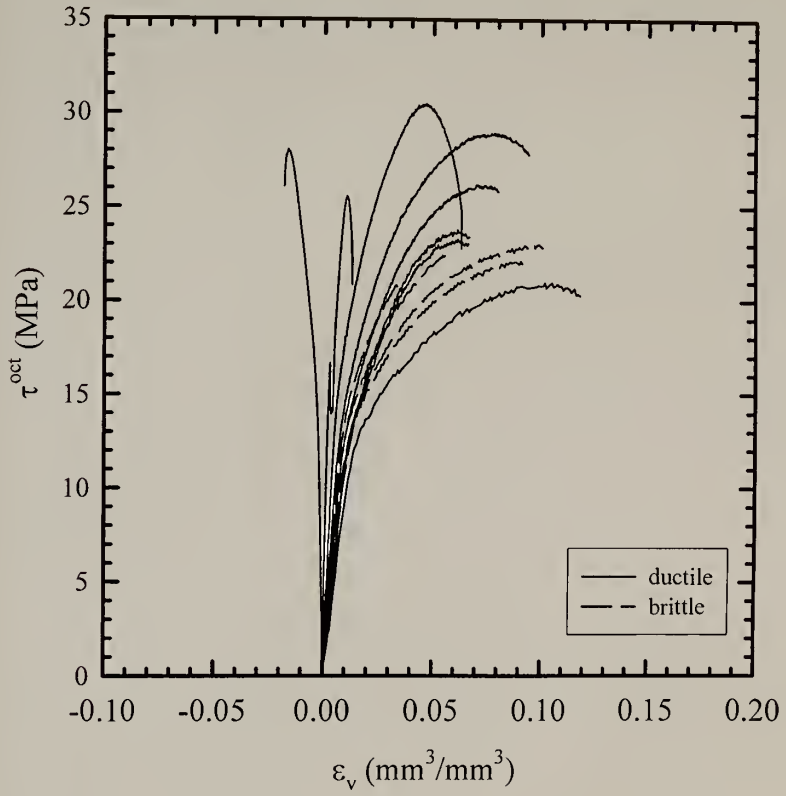

Figure 5.13: Octahedral shear stress, τ^{oct}, versus volumetric strain, ε_v, for MSHC material tested at 20°C and a nominal octahedral shear strain rate of 0.05 min^{-1}.

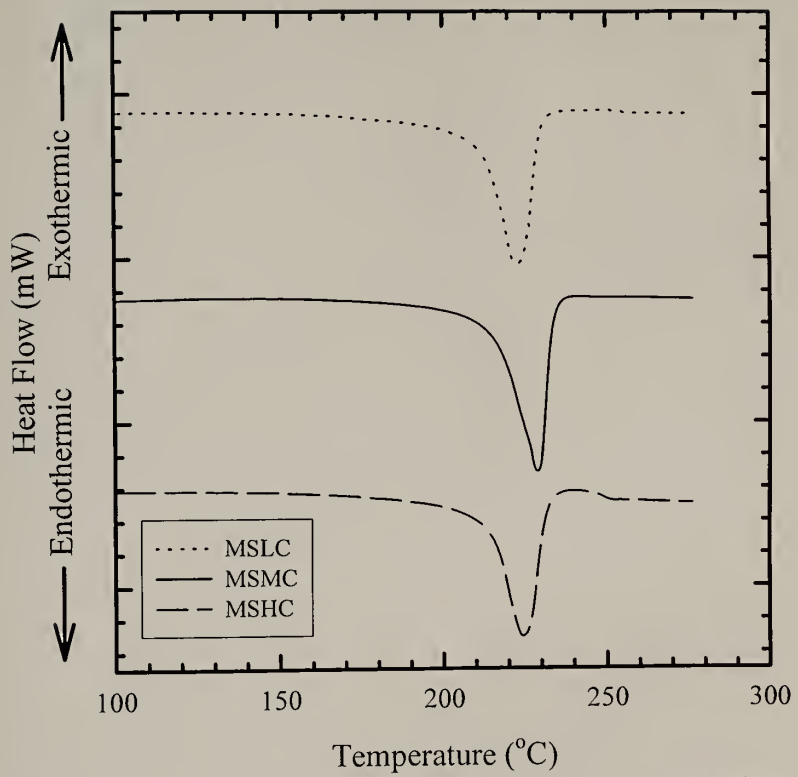

Figure 5.14: Representative DSC curves for materials extruded with different shear rates.

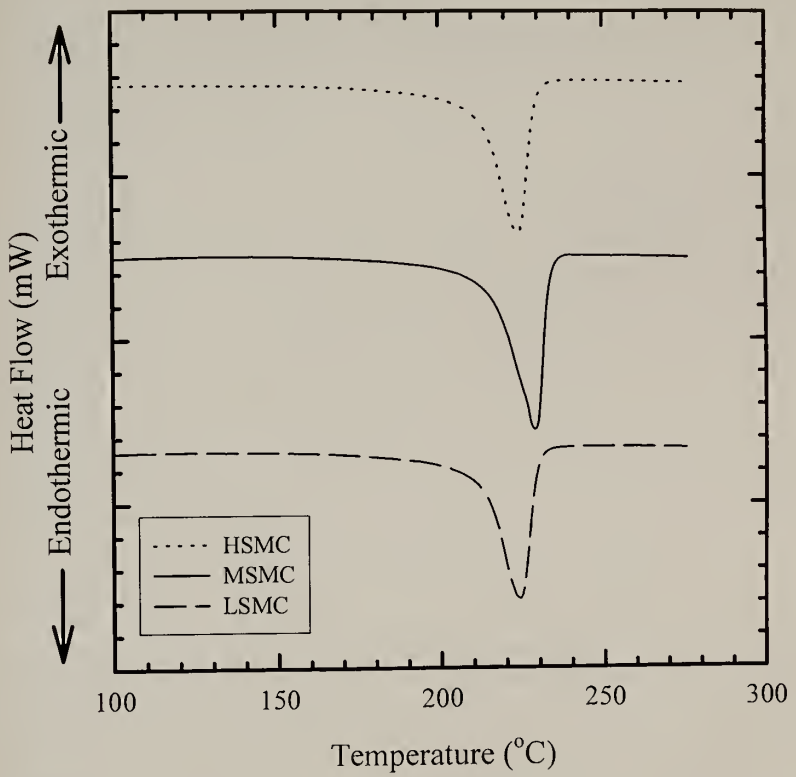

Figure 5.15: Representative DSC curves for materials extruded with different cooling rates.

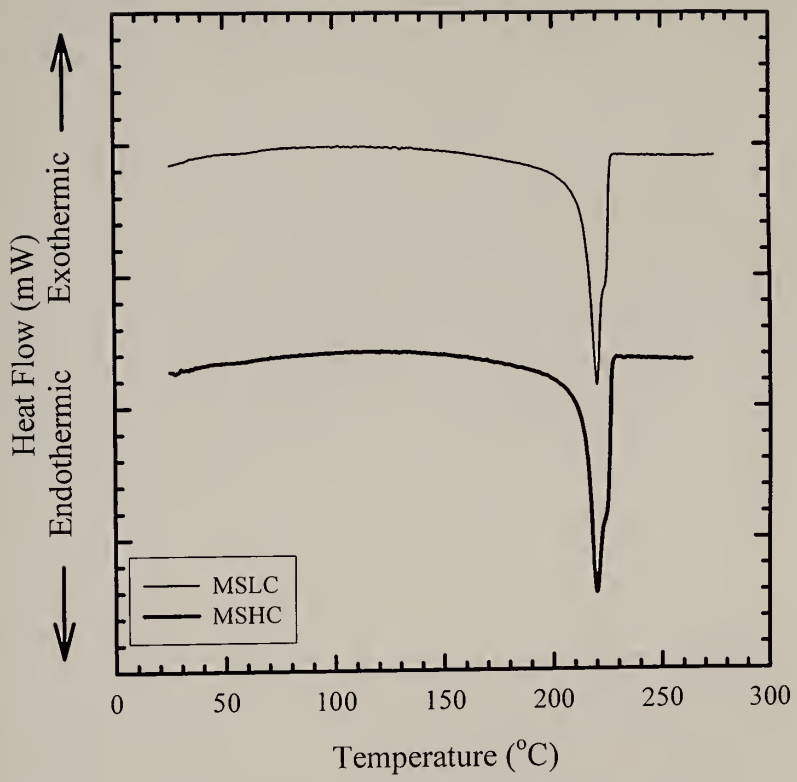

Figure 5.16: Representative DSC curves for MSLC and MSHC materials tested at a heating rate of 2°C/minute.

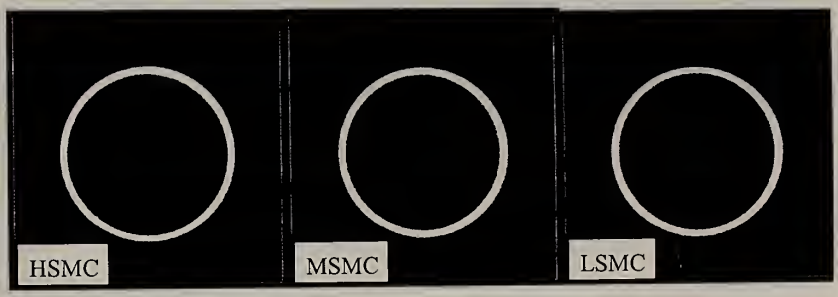

Figure 5.17: Wide-angle X-ray diffraction patterns for the samples processed at different shear rates. Beam direction is through the radial direction of the cylinders.

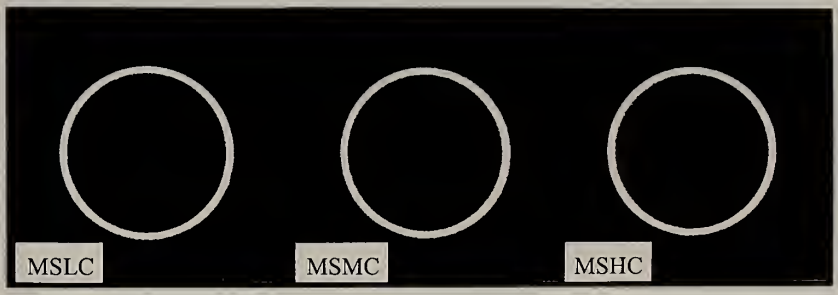

Figure 5.18: Wide-angle X-ray diffraction patterns for the samples processed at different cooling rates. Beam direction is through the radial direction of the cylinders.

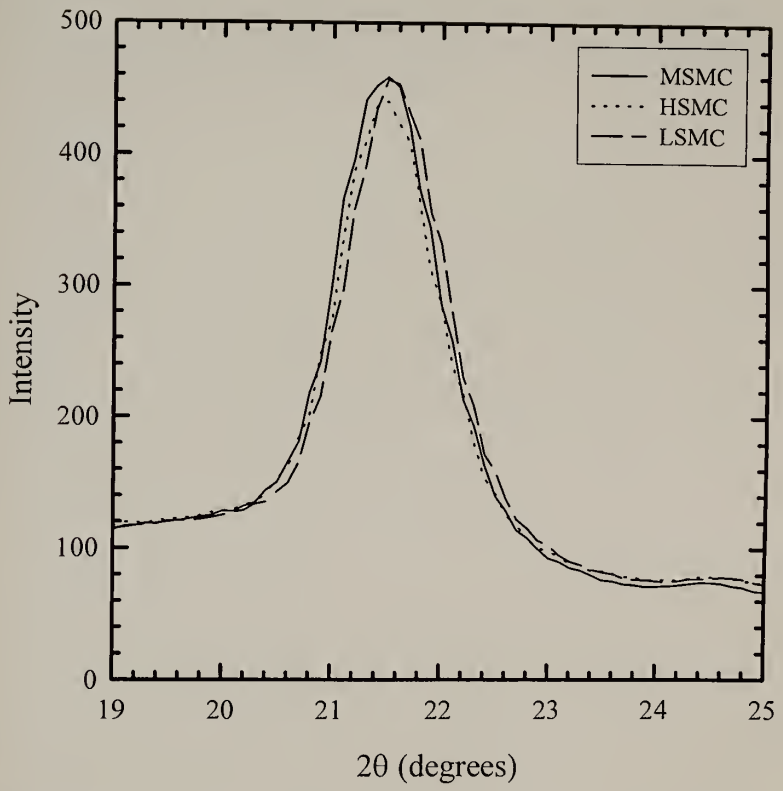

Figure 5.19: Main diffraction peak of the materials processed at different shear rates.

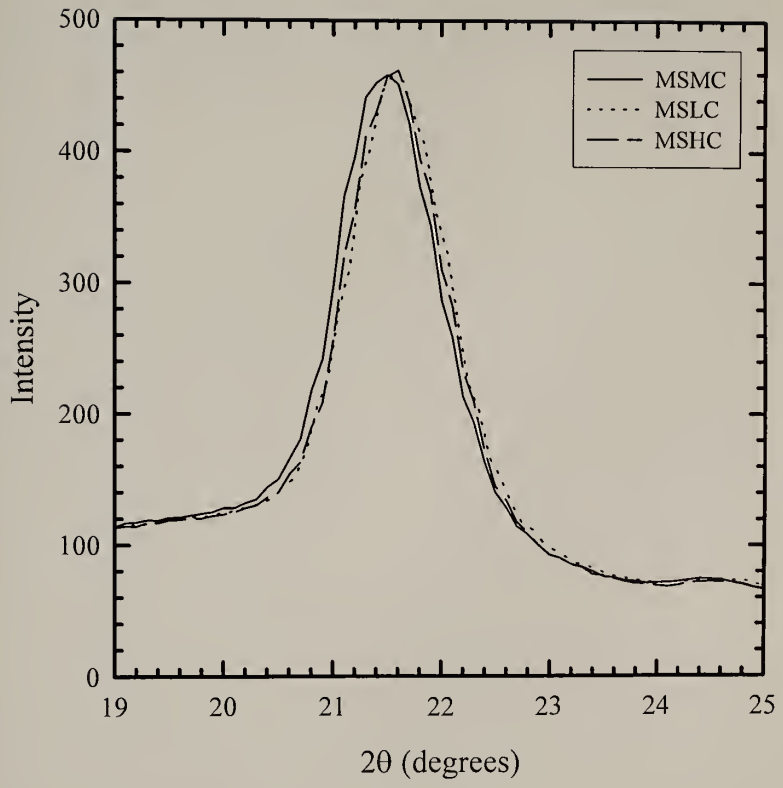

Figure 5.20: Main diffraction peak of the materials processed at different cooling rates.

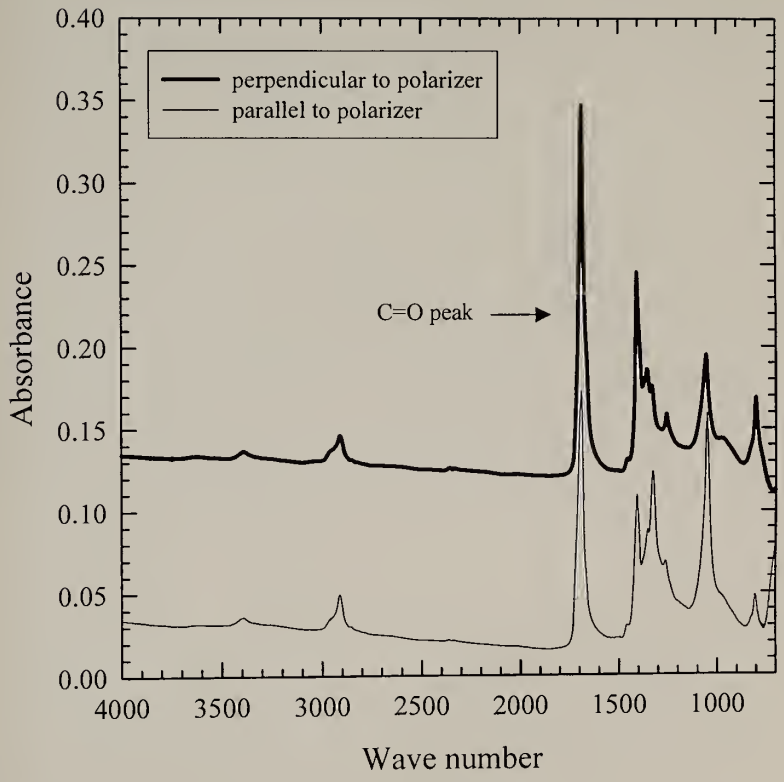

Figure 5.21: Infrared spectra for the MSMC with the extrusion direction oriented parallel and perpendicular with respect to the polarizer. Arrow indicates the peaks used in the analysis.

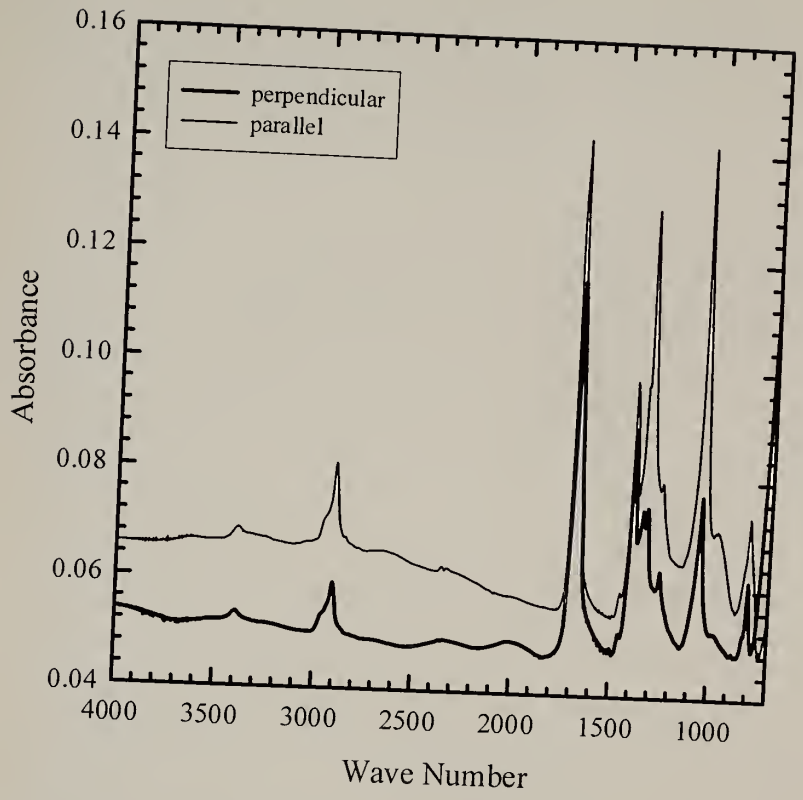

Figure 5.22: Infrared spectra for the HSMC with the extrusion direction oriented parallel and perpendicular with respect to the polarizer. Arrow indicates the peaks used in the analysis.

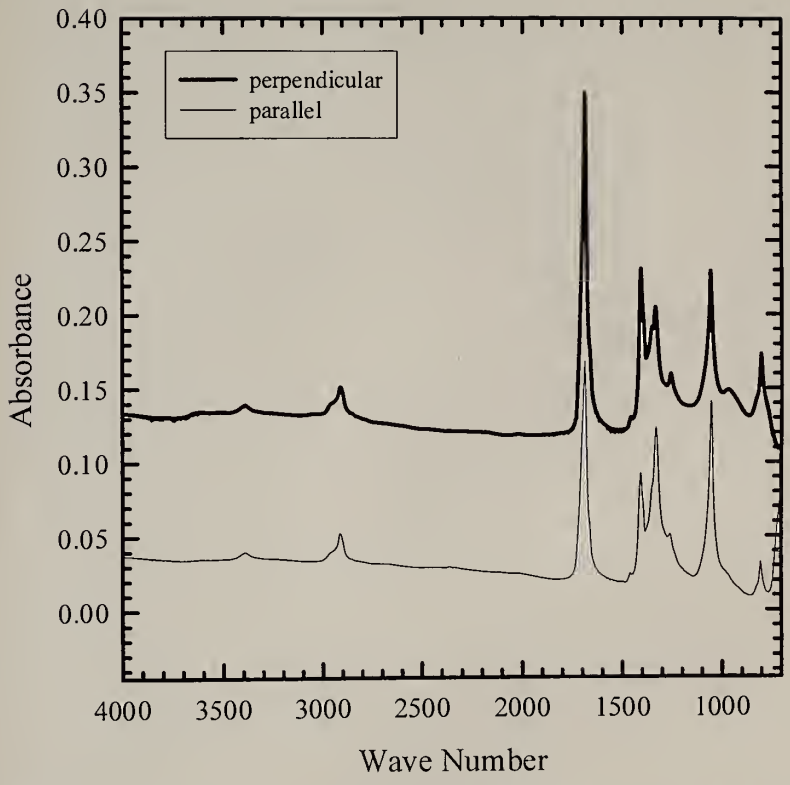

Figure 5.23: Infrared spectra for the LSMC with the extrusion direction oriented parallel and perpendicular with respect to the polarizer. Arrow indicates the peaks used in the analysis.

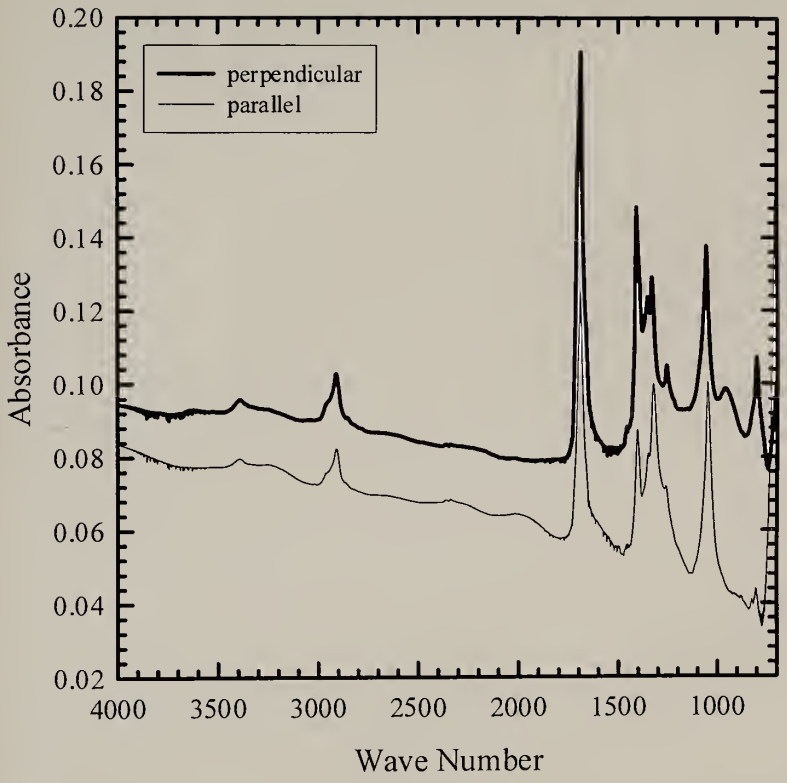

Figure 5.24: Infrared spectra for the MSLC with the extrusion direction oriented parallel and perpendicular with respect to the polarizer. Arrow indicates the peaks used in the analysis.

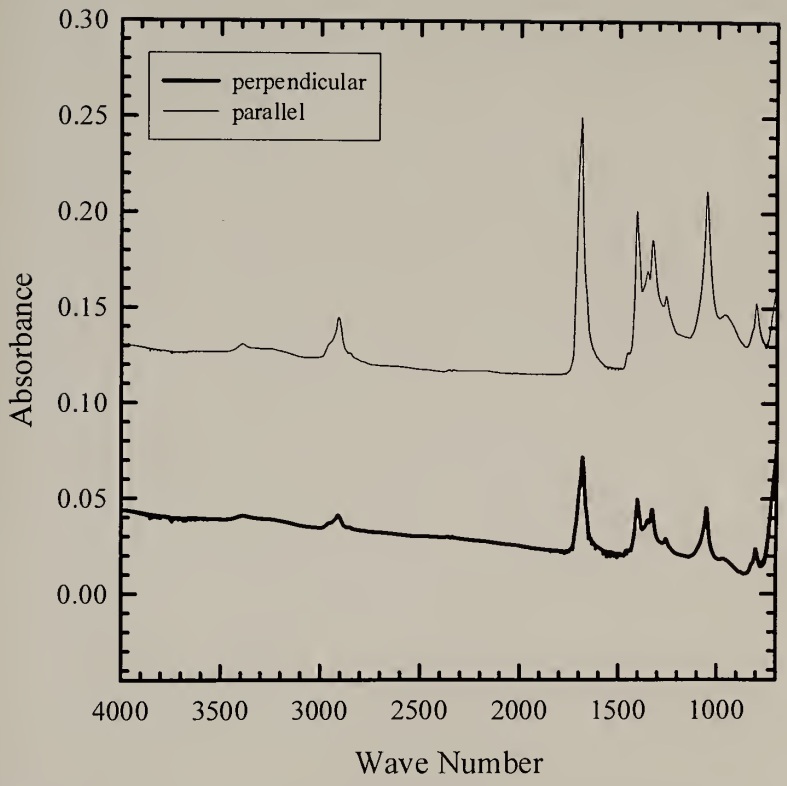

Figure 5.25: Infrared spectra for the MSHC with the extrusion direction oriented parallel and perpendicular with respect to the polarizer. Arrow indicates the peaks used in the analysis.

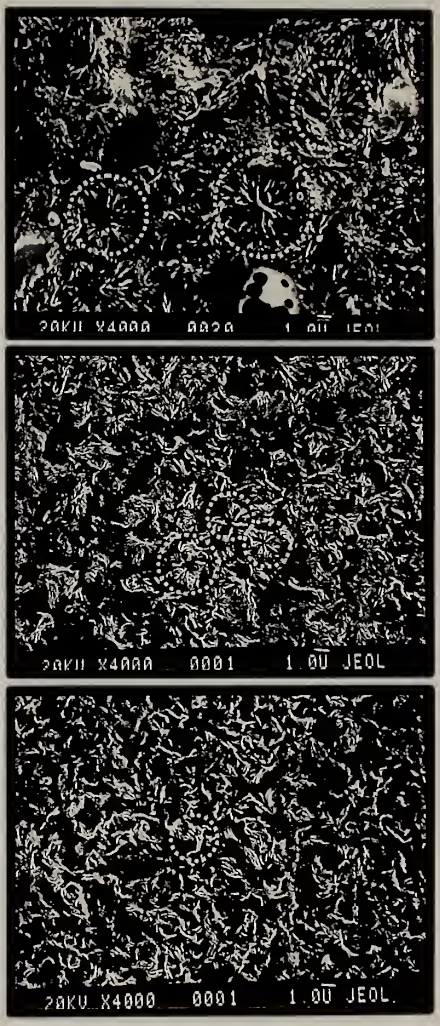

Figure 5.26: Electron micrographs for the MSMC, MSLC and MSHC samples.

Figure 5.27: Electron micrographs for the HSMC, LSMC, MSLC and MSHC samples.

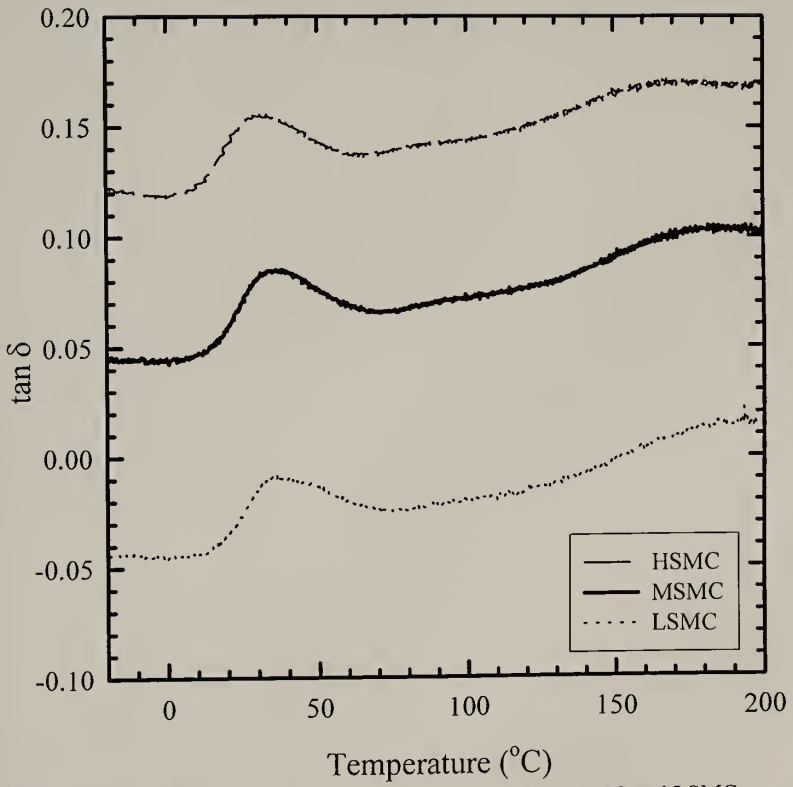

Figure 5.28: Representative DMTA spectra for the MSMC, HSMC and LSMC samples.

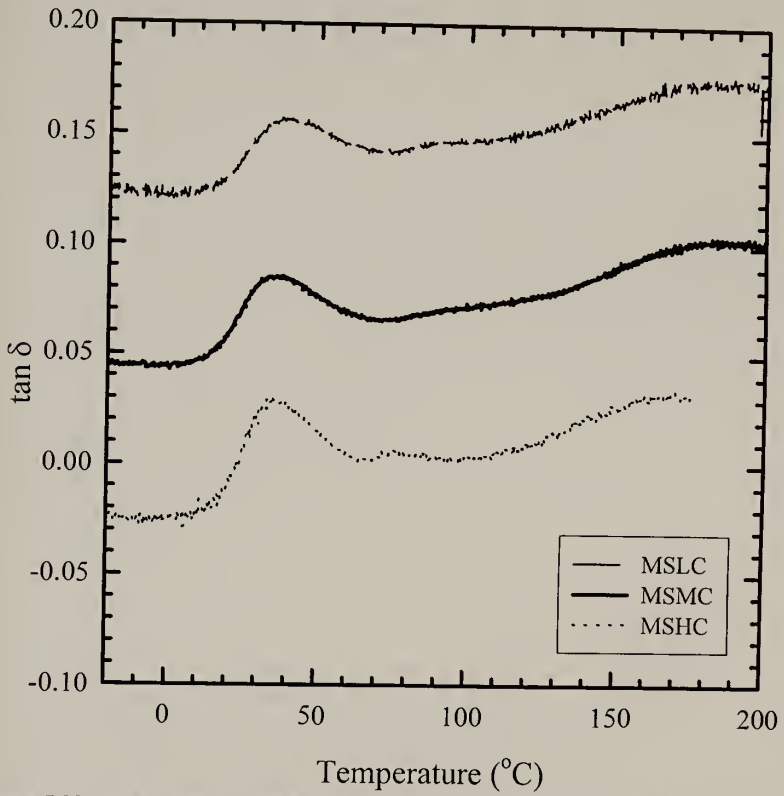

Figure 5.29: Representative DMTA spectra for the MSMC, MSLC and MSHC samples.

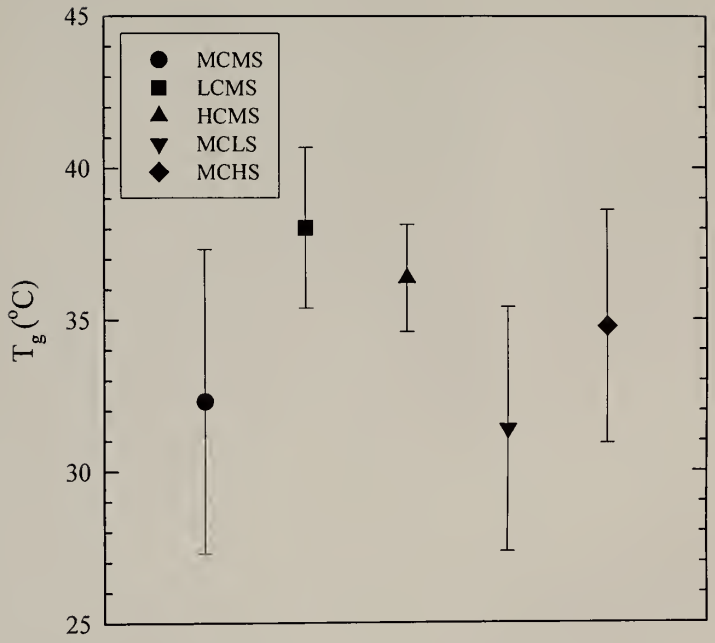

Figure 5.30: Mean value of glass transition temperature for each sample with error bars indicating maximum and minimum values.

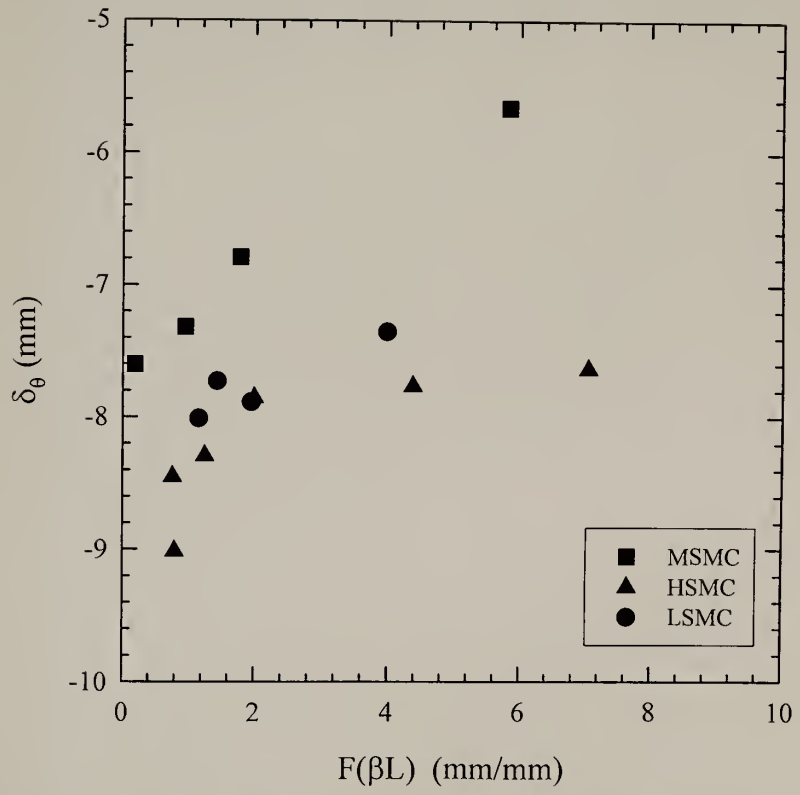

Figure 5.31: Data used in determining the residual stresses imparted to samples processed at different shear rates. Data plotted as diameter change (δ_θ) versus the geometric function (F(βL)).

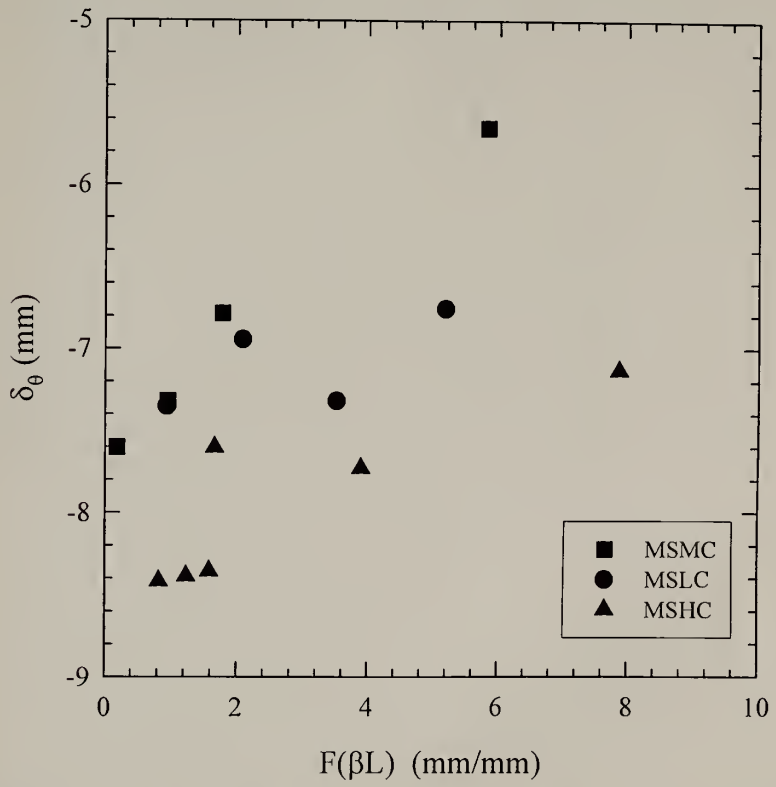

Figure 5.32: Data used in determining the residual stresses imparted to samples processed at different cooling rates. Data plotted as diameter change (δ_θ) versus the geometric function (F(βL)).

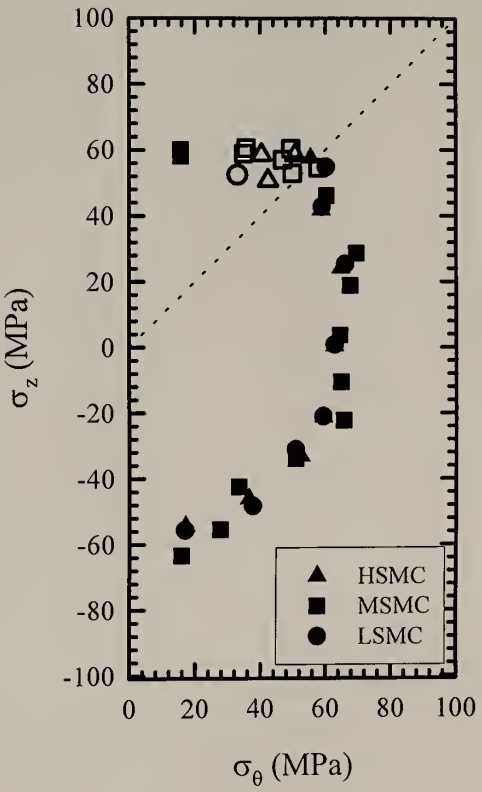

Figure 5.33: Axial stress, σ_a, for samples processed at different shear rates, shifted to account for residual stresses. The dashed line indicates the case of equi-biaxial loading, and solid and hollow symbols represent ductile and brittle failures, respectively.

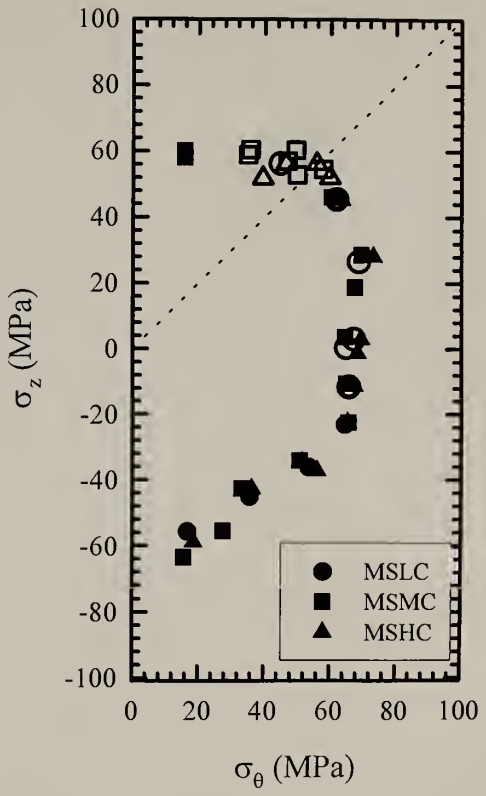

Figure 5.34: Axial stress, σ_a, versus circumferential stress, σ_θ, for samples processed at different cooling rates, shifted to account for residual stresses. The dashed line indicates the case of equi-biaxial loading, and solid and hollow symbols represent ductile and brittle failures, respectively.

CHAPTER 6

EFFECT OF MOLECULAR ARCHITECTURE ON CRYSTALLINE MORPHOLOGY

6.1 Background

The crystalline structure of aliphatic polyketones has been investigated since the early stages of development of this material[73]. Early studies on the copolymer (Figure 1.1, R=ethyl) indicated a relatively dense orthorhombic crystal structure similar to polyethylene. This is termed the α crystal structure and has dimensions indicated in Table 6.1. It is found, however, that substitution of ethyl groups with propyl groups, essentially adding side-groups or defects to the material, forces the lattice into a less dense crystal phase. This is termed the β phase with dimensions indicated in Table 6.1. The d-spacing values for this material, calculated from the cell parameters reported elsewhere[66,73], are listed in Table 6.2.

Besides the change in crystal structure with ethyl substitution, other interesting observations have been made for this material regarding the crystal structure. For example, it has been observed that some of the β-phase is transformed into α-phase upon drawing or orientation[39,66,67,74]. It has been also been observed that, upon heating, the α-phase transforms into β-phase at approximately 100°C[40,41]. Others[23,25,40,41,75] have also observed a drop in the melt temperature with increasing

level of substitution of ethyl groups with either propyl or butyl groups. These and other issues are looked at more closely in this study. They are examined as a function of the size of the substituting group as well as concentration. This is work done in collaboration with Dr. Alan J. Waddon, who is respectfully acknowledged. Not all details of this study are presented here, and the interested reader is referred to previously published work[67,74,76].

6.2 Material

The material examined in this portion of work is provided by BP-Amoco Chemicals. The family of polyketones is marketed under the tradename Ketonex®. The chemical formula is similar to that described in Figure 1.1 with alternating carbonyl and olefin groups. In this case, however, the R-group is varied in terms of composition and concentration. Here, the R-groups are either ethyl, propyl or butyl groups. The concentration of these groups in the materials examined here are indicated in Table 6.3. The mole percent substitution values are base on the percentage of ethyl groups that are effectively replaced by the R group. For example, consider a terpolymer consisting of ethyl, carbonyl and R groups. If the terpolymer has 10 mol% R with respect to the total number of groups, then, relative to the copolymer that contains no R groups, the terpolymer has 20% of the original ethyl groups substituted with propyl groups. Such a material would be reported as having 20% substitution in this thesis. Note that the material with R=CH_2CH_2 is essentially the unsubstituted copolymer, and is referred to as the copolymer within this text. The others are referred to by the substituting group, propyl or butyl, and the mol% of ethyl groups that are essentially replaced by this group.

Table 6.3 also indicates the reported melting temperature and molding temperatures used in producing the samples. The materials are received from the manufacturer in the form of melt pressed films with an approximate thickness of 170μm. Because the copolymer films obtained for this study indicate some level of orientation from the processing[74], they are analyzed for the sake of comparison in terms of the crystallinity and α–β transition only.

6.3 Experimental

6.3.1 Wide Angle X-ray Diffraction

Wide-angle X-ray diffraction is a convenient method for analyzing the crystalline phase of aliphatic polyketones. Experiments are performed on one of two pieces of equipment. The system used for obtaining patterns, rather than data analysis, utilizes a pinhole collimated monochromatic CuK_α radiation. Patterns are collected with a GADDS 2-D detector by Brucker. The second system, more accurate for measurement of spacings, is a Siemens D500. This is operated in normal/transmission mode using CuK_α radiation with a Ni filter. Experiments are performed on both drawn and undrawn films.

6.3.2 Differential Scanning Calorimetry

DSC experiments are carried out in order to determine the crystallinity, melt temperature and to detect the α–β crystal transition upon heating. Experiments are carried out on a Du Pont DSC 2910. Samples of approximately 7 mg are heated at

10°C/minute. Crystallinity calculations are based on a 100% crystalline heat of fusion of ΔH_f=227 J/g[65]. Experiments are performed on both drawn and undrawn films.

6.3.3 Small Angle X-ray Scattering

In order to investigate the lamellar periodicity of the materials, SAXS experiments are carried out. For this, a Rigaku pinhole camera with rotating anode source is used. Again, the radiation is Ni filtered CuK_α. The detector is a Brucker multi-wire Hi-Star 2-D detector. Experiments are performed on undrawn films only.

6.3.4 Film Drawing

The effect of drawing is studied for the propyl substituted series of films. In initial experiments, films are hand-drawn to draw ratios of λ~3-6. Later studies on the effect of draw rate use controlled drawing in an Instron 4411 tensile testing machine. Rates of 5, 50, and 500 mm/min are used on strips of film. The length of film between grips is approximately 25mm. These films are analyzed for the presence of α and β phase by WAXD and the α–β crystal transition by DSC.

6.4 Undrawn Films

6.4.1 Propyl Substituted Films

6.4.1.1. WAXD

The WAXD data for the undrawn films with propyl group substitution are plotted in Figure 6.1. The data is obtained from integration over the entire azimuthal angle of the diffraction patterns, from which all samples appear to be isotropic. Three main reflections are observed for these materials. These are positioned at 2θ~21.6, 25.1,

29.1°. Some of the features, general for aliphatic polyketones, are described here. The most prominent peak is that at ~22°, which corresponds to the mixed peak $110_\alpha/110_\beta/200_\beta$ (Table 6.2). The second peak, at ~26°, corresponds to both 200_α and 111_β. The third peak at ~29° corresponds exclusively to 210_β. Therefore, from these plots, he presence of β-phase is clear. However, for the case of isotropic samples, WAXD cannot unambiguously identify the presence of α-phase. Only upon orientation do the 200_α and 111_β peaks at 25.1° separate, allowing the presence of α-phase to be determined. Since this series of materials is isotropic and contains propyl substitution, it is suggested that the mixed peaks at 21.65° and25.1° are due mainly to the presence of the less dense β-phase.

6.4.1.2. DSC

The DSC scans for the propyl substituted materials are shown in Figure 6.2. For comparison, the usubstituted copolymer data is also included. Crystallinity and heat of fusion data are presented in Table 6.4. A few observations are apparent. Firstly, a decrease in heat of fusion (thus crystallinity) with increasing level of substitution is clear. The decrease in crystallinity can easily be explained. The propyl groups that replace the ethyl groups effectively act as side branches or defects, which the crystal lattice can only accommodate in limited amount. As the level of substitution increases, the amount of material able to crystallize decreases accordingly.

A decrease in melt temperature is also observed and related to the ability of the crystal lattice to accommodate the defects. A plot of melt temperature as a function of substitution level is shown in Figure 6.3. This plot includes data obtained from this

work as well as previously reported data[19,23,40]. Although there is some difference between data sets, a similar trend is observed. It is noticed that T_m decreases linearly up to a substitution level of ~9 mol%. Beyond this point, the linearity ceases. According to the inclusion model described by Sanchez and Eby[77] this point indicates the concentration at which the crystal lattice is saturated and can no longer accommodate the defects. Thus, it appears that the crystal lattice can accommodate approximately 9 mol% of propyl groups before reaching the saturation point.

The materials examined all display a single, broad melting peak. This is consistent with the presence of a single population of lamellae within the material. The sharp peak observed at a slightly higher temperature for some of the samples is probably due to reorganization of the original crystal population. This type of reorganization has been observed previously for the ~6 mol% propyl substituted Carilon® material[67]. The larger lower melting peak is that which is plotted in Figure 6.3 and is considered representative of the original crystal population.

In addition to the main melting peak at 255°C, the copolymer also displays an endotherm at approximately 92°C. This corresponds to the α–β crystal phase transition described previously. This temperature is similar to that reported by others (113°C[40], 100°C[41]) for this transition. A broad, weak endotherm is also observed for the propyl substituted materials in the range of 60-80°C. This may be attributed to the presence of very small, imperfect α-phase crystals.

6.4.1.3. SAXS

The SAXS results are presented in Figure 6.4 in the form of Is^2 versus s, where I is the intensity and $s=2(\sin\theta)/\lambda$. As with WAXD, this data is obtained from integration over the entire azimuthal angle of the SAXS profiles. A single maximum is observed for each material at s~0.0085, corresponding to a long period of ~120Å. It is also observed that with increasing substitution, this peak becomes broader. As a measure of this, the full width at half maximum (FWHM) is plotted as a function of level of substitution in Figure 6.5. It is clear that the width increases up to a limit of ~9 mol% substitution. The sharpness of such a peak is related to electron density fluctuations and is related to the regularity of the lamellar stacking. With the assumption that two phases are present- crystalline and amorphous- a decrease in peak sharpness can be related to increased irregularity in the stacking repeat between the two phases. This can, in turn, be related to either an increasingly rough lamellar surface or a larger distribution of lamellar sizes.

The trend observed in Figure 6.5 appears similar to the trend of decreasing T_m with substitution level in Figure 6.3, with an initial slope that ceases beyond a certain substitution level. The range of substitution levels in which peak broadening is observed in SAXS is about the same as that for which the melt temperature decreases sharply in DSC. Again, this is attributed to the saturation point of the lattice. Beyond this point, the effect of increasing concentration is dramatically reduced in both cases. For the SAXS results, the explanation for this is again quite simple. The broadening of the SAXS peak may be due to problems with folding due to the presence of the side-groups on the chain or locally high fluctuations in defect concentration causing the termination of crystalline order along a chain. The effects of these on the SAXS results can only

increase as long as the increasing side-group levels are altering the crystalline phase. Once the crystal is saturated with the side-groups, additional substitution affects the inter-lamellar regions, not the crystal. Therefore, beyond the saturation limit, there is no additional contribution to SAXS peak broadening.

6.4.2 Butyl Substituted Films

6.4.2.1. WAXD

The WAXD data for the undrawn films with butyl group substitution are plotted in Figure 6.6. The same general features observed for the propyl series are also observed for the butyl series. Three peaks at 2θ~22, 26, 29° correspond to the mixed $110_\alpha/110_\beta/200_\beta$, mixed $200_\alpha/111_\beta$, and 210_β, respectively. Again, only the β-phase can be unambiguously identified for unoriented polyketones, though it is likely that very little α-phase is present..

6.4.2.2. DSC

The DSC scans for the undrawn butyl series of materials are presented in Figure 6.7 with the data listed in Table 6.5. As with the propyl series, decreases in crystallinity and melt temperature are observed. In this case, the linear decrease in melt temperature is apparent up to a substitution level of ~7 mol%, Figure 6.8. Again, this level of concentration is the saturation point of the crystal lattice, beyond which the side-groups are no longer accommodated within the lattice. Since the side-groups due to butyl substitution are larger than those for propyl substitution, it is reasonable that the saturation point is at a lower level than the propyl series.

A significant difference observed for the butyl series relative to the propyl series is the presence of double melting peaks. The peaks are quite distinct and are likely due to a bimodal crystal distribution rather than reorganization, as was described for the propyl series. In order to verify this hypothesis, an additional set of DSC experiments was performed on the material with the highest level of butyl substitution at different heating rates. It is argued that any reorganization should be most apparent in this material. The results are plotted in Figure 6.9. From this it is observed that, while the heat rate has some effect on the sharpness of the melting peaks, the two peaks clearly persist in all cases of the butyl series. Thus, it is suggested that, indeed, a bimodal distribution is present in the butyl series. Why the butyl series would display a bimodal distribution is not clear, but could be the result of varied cooling conditions compared to the propyl series[76].

A weak, broad endotherm is observed in the range of ~50-80°C, similar to that observed for the propyl series. This is again attributed to very small, imperfect α crystals and the transformation of these to β crystals. This endotherm is at a higher temperature for the copolymer since it is able to form larger, more perfect α crystal in the absence of the propyl or butyl "defects".

6.4.2.3.SAXS

The SAXS data for the butyl series are plotted in Figure 6.10. Similar to the propyl series, the butyl materials each show a single, broad maximum corresponding to a long period of ~120Å. The FWHM for these peaks are plotted as a function of substitution level in Figure 6.11. Note that the FWHM in this case is significantly larger

than for the propyl series. This is consistent with the presence of a bimodal distribution of lamellae, and therefore this observation agrees with the DSC results described previously. In addition, it is observed that the width increases with increasing side-group concentration up to a limiting value. This is attributed to the saturation point of the crystal lattice for side-group accommodation, as was described for the propyl series of materials. This saturation point, between 8-10 mol%, agrees with the DSC results.

6.5 Drawn Films – Propyl Substituted

6.5.1 WAXD

Films drawn by hand to draw ratios of λ~3-6 were examined with WAXD in order to determine if the α-phase could be distinguished upon orientation. Patterns obtained for the material with 2.0% propyl substitution are presented in Figure 6.12. Upon orientation, the peak observed at 2θ~26° in the unoriented case separates into different regions of the Debye ring, allowing the unambiguous determination of the presence of the α crystalline phase. The equatorial scans for the propyl substituted films are presented in Figure 6.13 for the beam direction through the thickness of the film and in Figure 6.14 for the beam direction edge-on, or through the width of the film. The peak at ~26° now corresponds to 200_{α} and can be clearly identified for the 2.0% material, indicating a significant level of α-phase. It is also noticed that the reflection is much stronger in the edge-on projection, indicating that the (100_{α}) is oriented within the plane of the film. Since the films are isotropic prior to drawing, this preferred orientation is a result of the drawing process.

With increasing substitution level, the intensity of the 200_α peak decreases. This is consistent with the decreased ability to form the dense α-phase with increased number of side-groups.

6.5.2 DSC

The DSC scans for the drawn films are presented in Figure 6.15. Due to the small amount of material available, not all sample were able to produce enough drawn material for this analysis. Therefore, some materials were not examined in this portion of work. However, the range of substitution levels is considered. A small, broad peak is apparent for all samples in the 40 to 50°C range. This is assigned as the α–β crystal transition. The temperature range for this transition is lower than observed for the copolymer. Interestingly, this endotherm is observed for each material studied, indicating that α-phase is present in each- even at the highest level of substitution. This is in contrast to the WAXD results, for which only materials with low levels of substitution show distinct α-phase reflections. It is expected that as substitution level increases, the average defect-free length will become shorter thus causing the size of a crystallites to become smaller. The observed effect could be a result of size-scale: WAXD may be unable to detect the smaller crystallite regions, while thermal analysis is able.

6.5.3 Effect of Draw Rate

The effect of draw rate on the crystal structure is also studied. Strips cut from the 8.8 mol% propyl group film are drawn at controlled speeds (5, 50, 500 mm/min) in an Instron tensile testing machine. The drawn films are then examined by WAXD, Figure

6.16. While the results are subtle, some trends are observed. With increasing draw rate, the width of the main peak becomes narrower, consistent with increasing degree of orientation. In addition, with increase in draw rate, the presence of the 200_α at ~26° becomes less clear. At 500 mm/min, this peak is not distinguishable, despite the greater degree of orientation. Thus, the formation of α-phase appears to be favored by lower draw speeds. This result could be due to internal heating effects during the drawing process. As shown earlier, a α–β crystal transition is observed at ~100°C in undrawn films of the copolymer. When drawn, this transition region drops to the ~50°C, and is detected in all the materials studied here. It is reasonable to expect that higher draw rates might lead to higher levels of internal heating due to the low thermal conductivity and high internal damping. If the local temperature exceeds the α–β transition temperature, then any α-phase that had been present within the material or formed due to the drawing process will be transformed back to the β-phase. It has previously been shown that significant undercooling is required to reverse this α–β transition[40], and it is therefore expected that high draw rates will ultimately result in the loss of α crystallites beginning with the smallest, least thermally stable crystallites.

6.6 Summary

The effects of substitution group and level of substitution have been examined for the crystalline phases of aliphatic polyketones. It is determined that the β-phase is the most dominant in the unoriented materials. However, upon drawing, some α-phase is observed. The α crystals can be detected by WAXD for low substitution levels, and

by DSC for all levels of substitution examined here. A saturation point of the crystal lattice is determined at ~9 mol% for propyl groups and ~7 mol% for butyl groups. Beyond this point, the lattice can no longer accommodate the side groups. This determination is made from both DSC and SAXS data. It is also observed that the formation of α-phase upon orientation is favored by low draw rates. It is believed that local heating at higher draw rates converts any α-phase to β-phase.

	α[Lommerts[66]]	β[Chatani[73]]
a (Å)	6.91	7.97
b (Å)	5.12	4.76
c (Å)	7.60	7.57

Table 6.1: Unit cell parameters for the α and β crystal structures of aliphatic polyketones.

hkl	α[Lommerts[66]]	β[Chatani[73]]
011_{β}		4.02
110_{α}	4.11	
110_{β}		4.09
200_{β}		3.99
002_{α}	3.80	
002_{β}		3.79
111_{α}	3.62	
111_{β}		3.59
200_{α}	3.46	
210_{α}	2.85	
210_{β}		3.06
211_{β}		2.83
212_{β}		2.38
113_{α}	2.16	
203_{β}		2.13
113_{β}		2.15

Table 6.2: Principal reflections for aliphatic polykeetones. Values are calculated from cell parameters reported elsewhere [Chatani[73]; Lommerts[66]].

R group	R group concentration (mol %)	T_m (°C)	Molding Temp. (°C)
CH_2CH_2	100	252	255
$CHCH_2CH_3$	2.0	248	270
$CHCH_2CH_3$	6.6	223	245
$CHCH_2CH_3$	8.8	215	230
$CHCH_2CH_3$	10.0	209	230
$CHCH_2CH_3$	14.6	198	220
$CHCH_2CH_2CH_3$	4.4	229	250
$CHCH_2CH_2CH_3$	5.8	225	245
$CHCH_2CH_2CH_3$	7.4	214	230
$CHCH_2CH_2CH_3$	10.0	210	230
$CHCH_2CH_2CH_3$	12.0	203	220

Table 6.3: Compositions of aliphatic polyketones studied as films.

Propyl Content (mol%)	ΔH_f (J/g)	Crystallinity (%)	Lower T_m (^oC)	Upper T_m (^oC)
0	121	53	256	-
2.0	114	50	245	247
6.6	97	43	226	231
8.8	85	37	217	223
10.0	86	38	216	220
14.6	63	28	202	206

Table 6.4: Heat of fusion, crystallinity and melt temperature data for undrawn propyl substituted films.

Butyl content (mol %)	ΔH_f (J/g)	Crystallinity (%)	Lower T_m (^oC)	Upper T_m (^oC)
0	121	53	256	-
4.4	89	39	224	234
5.8	88	39	218	229
7.6	76	33	211	221
10.0	68	30	206	217
12.0	61	27	206	210

Table 6.5: Heat of fusion, crystallinity and melt temperature data for undrawn butyl substituted films.

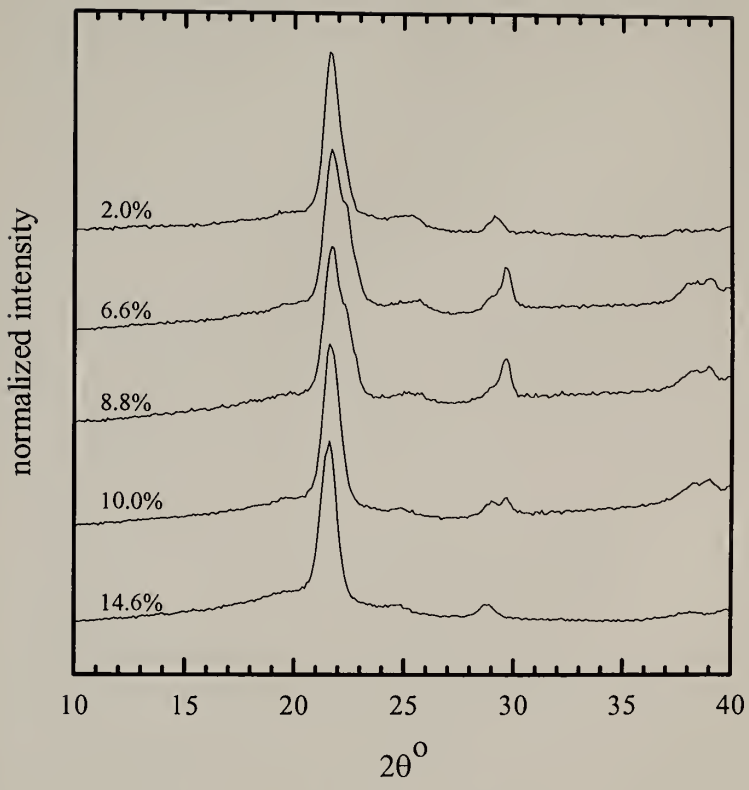

Figure 6.1: WAXD data plotted relative intensity versus 2θ for undrawn propyl substituted films.

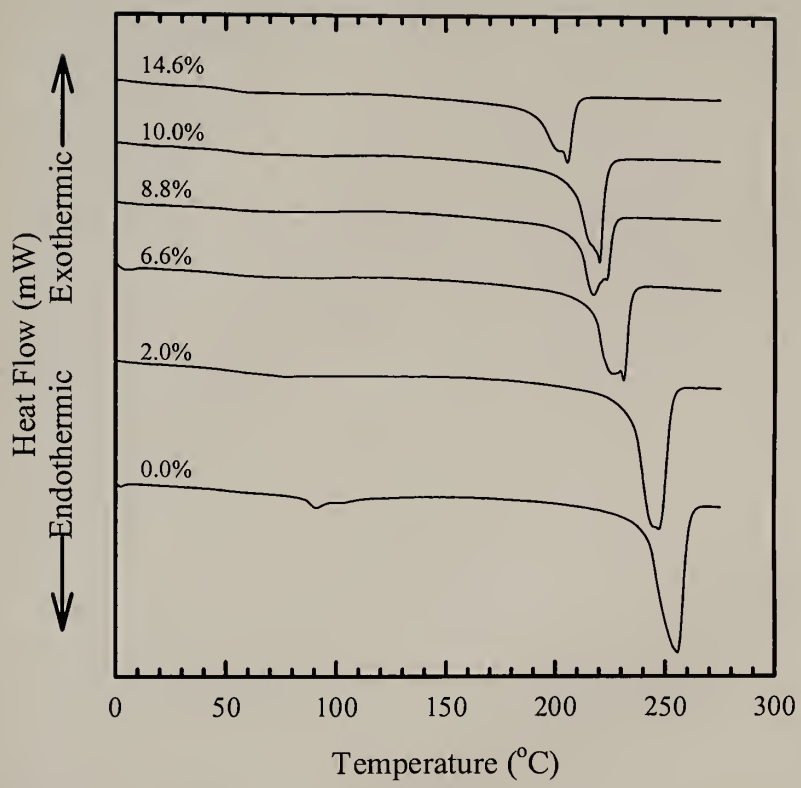

Figure 6.2: DSC scans for undrawn propyl substituted films.

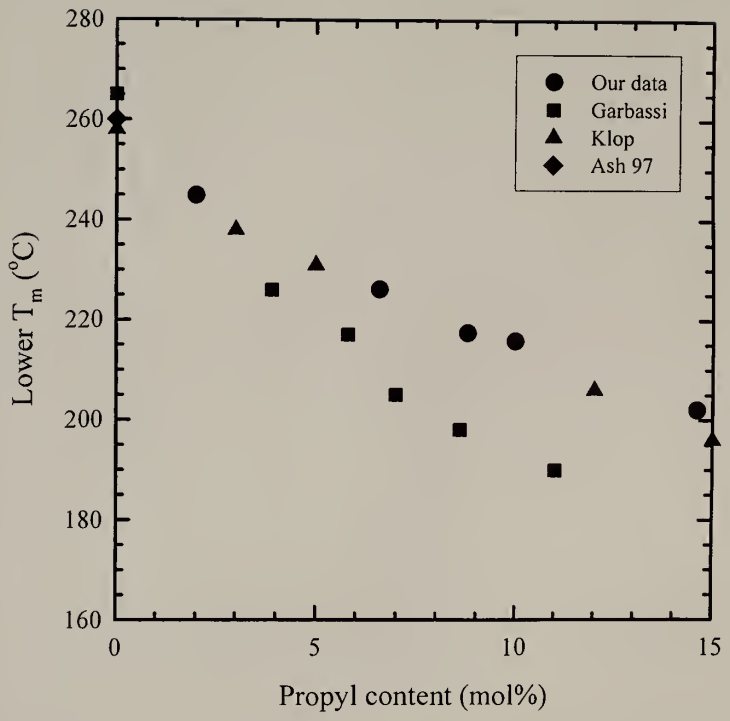

Figure 6.3: Melt temperature as a function of propyl substitution level.

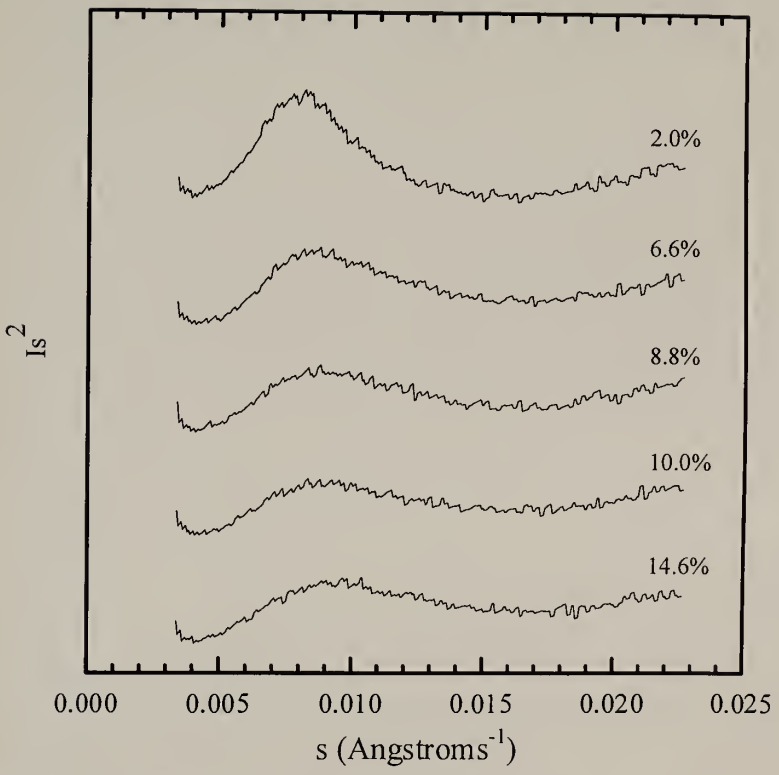

Figure 6.4: SAXS data for propyl series materials.

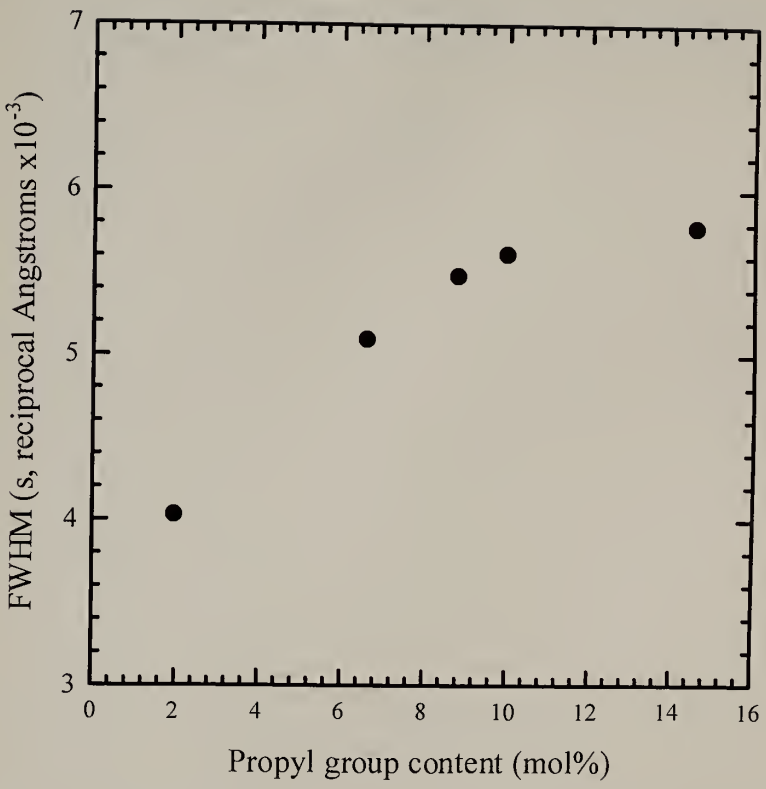

Figure 6.5: Full width at half maximum of SAXS peaks as a function of propyl group concentration.

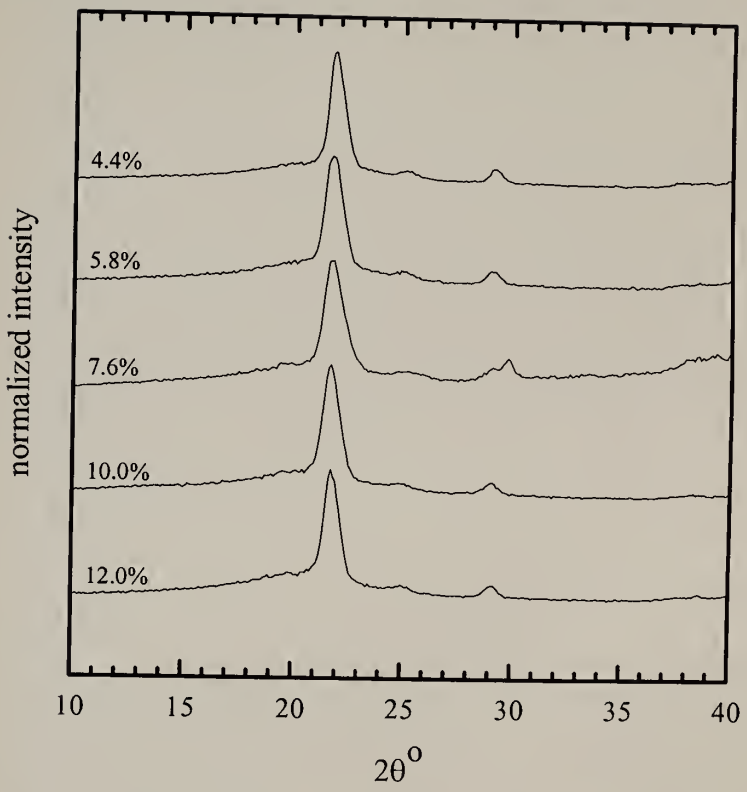

Figure 6.6: WAXD data plotted relative intensity versus 2θ for undrawn butyl substituted films.

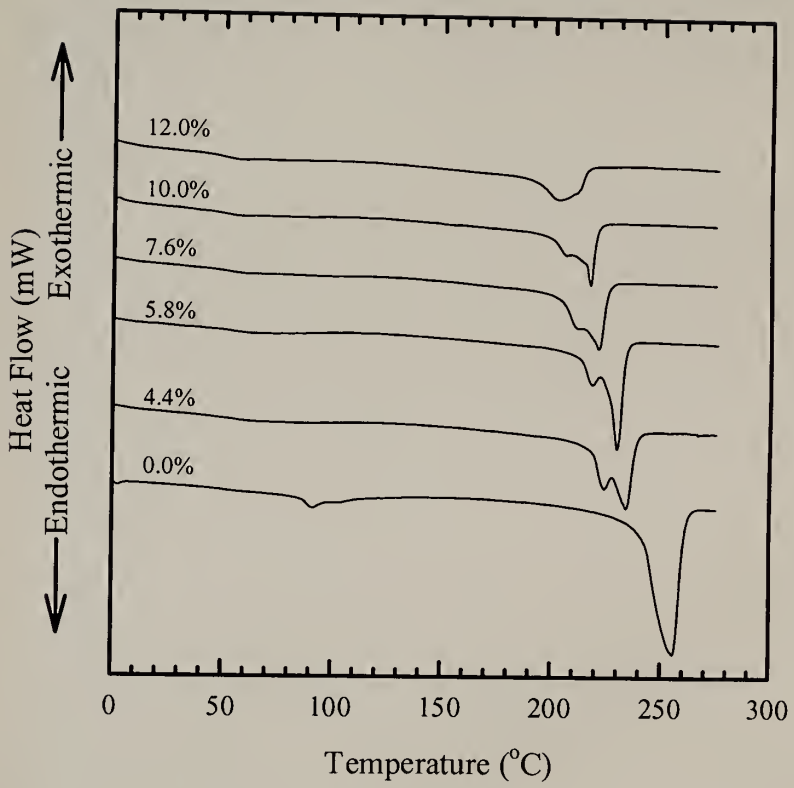

Figure 6.7: DSC scans for undrawn butyl substituted films.

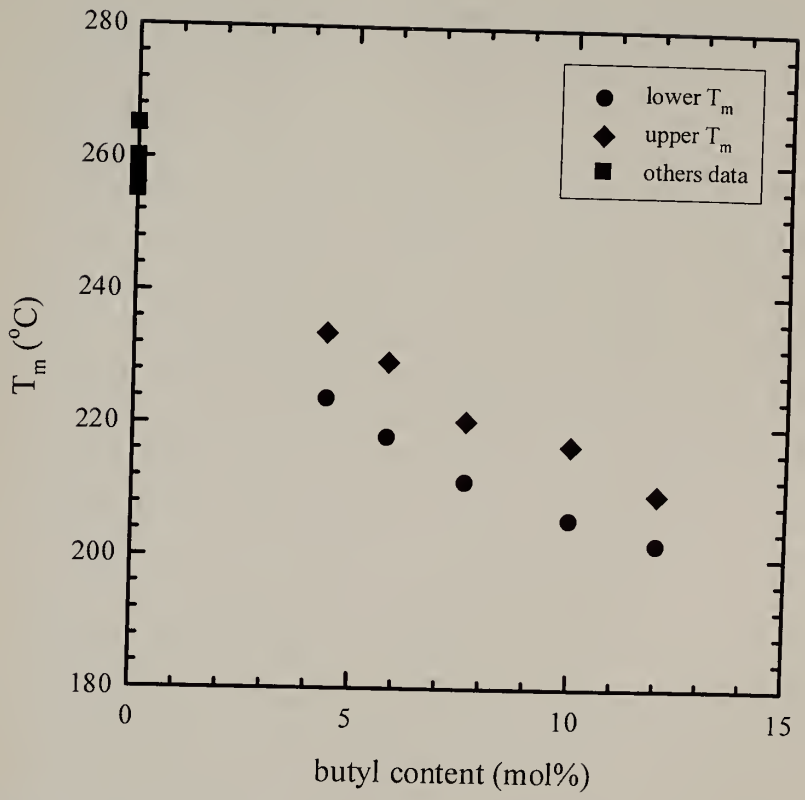

Figure 6.8: Melt temperature as a function of butyl substitution level.

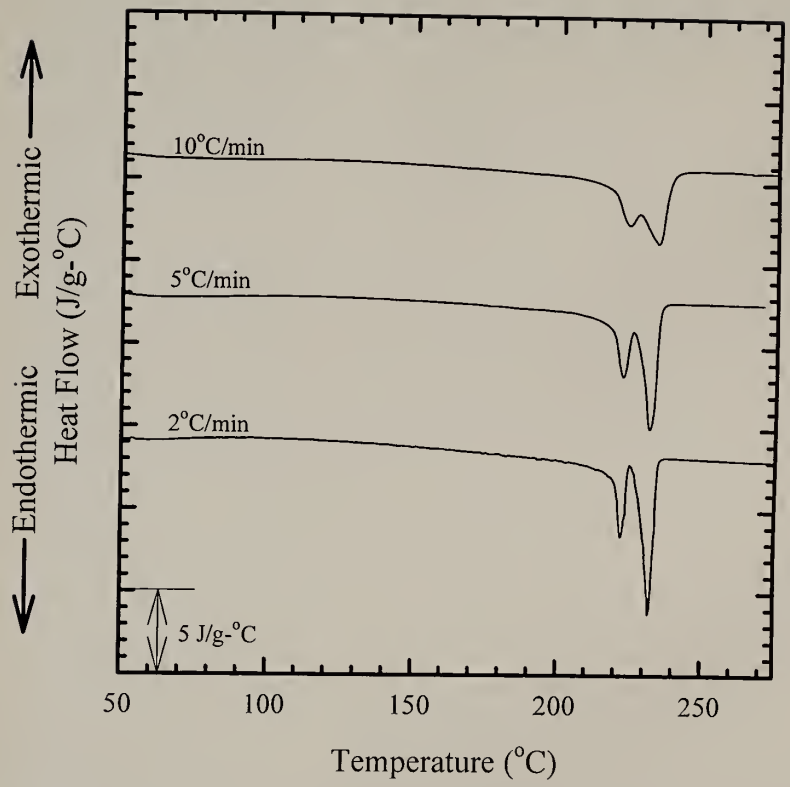

Figure 6.9: DSC scans for undrawn butyl substituted films at various heating rates.

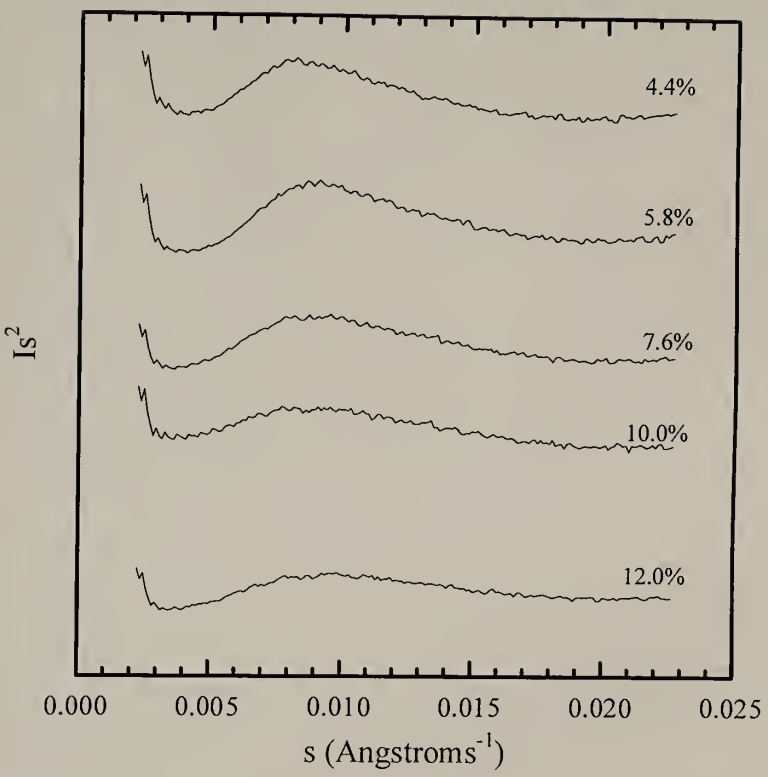

Figure 6.10: SAXS data for butyl series materials.

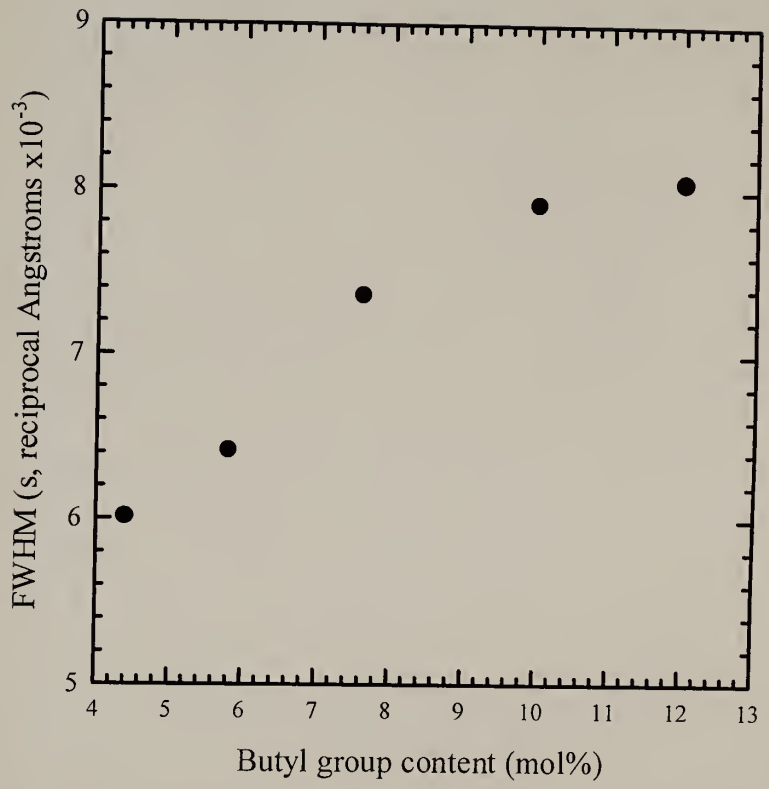

Figure 6.11: Full width at half maximum of SAXS peaks as a function of butyl group concentration.

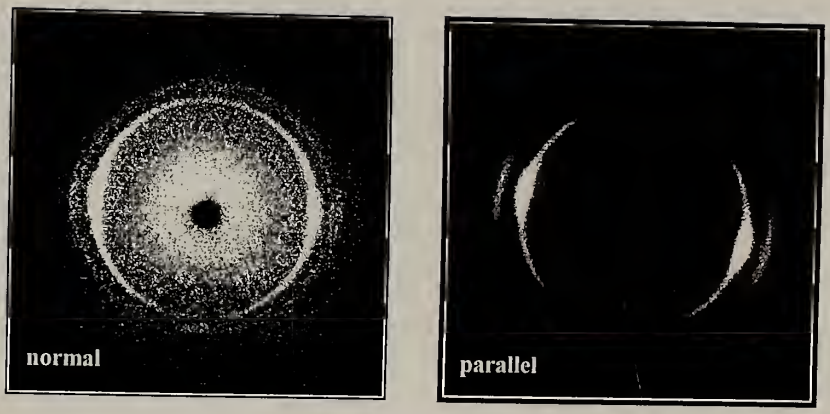

Figure 6.12: WAXD patterns for the 2.0 mol% propyl substituted material. One pattern is with beam direction normal to the plane of the film, the parallel (edge-on).

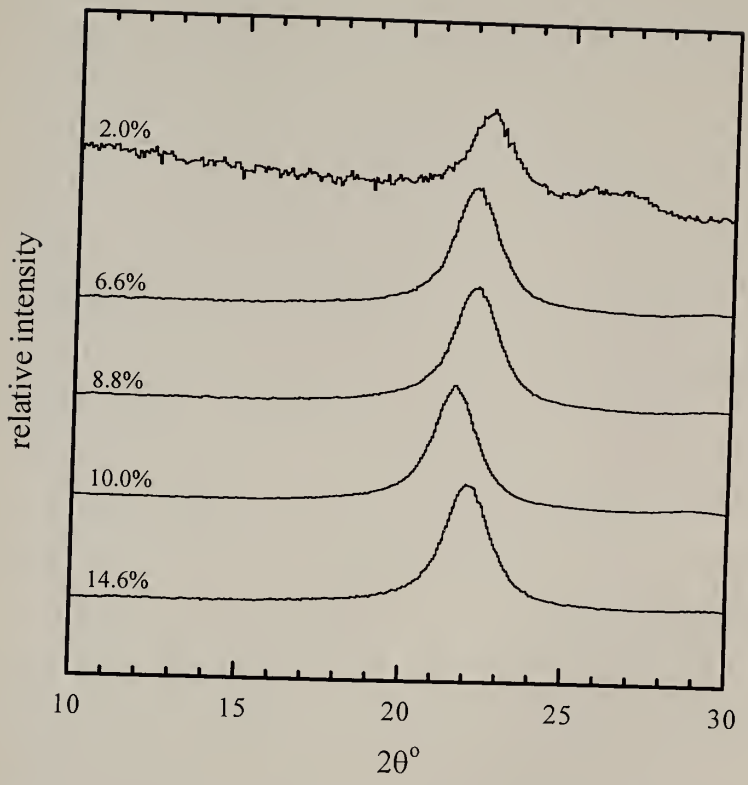

Figure 6.13: WAXD data plotted relative intensity versus 2θ for the drawn propyl substituted films with the beam normal to the plane of the film.

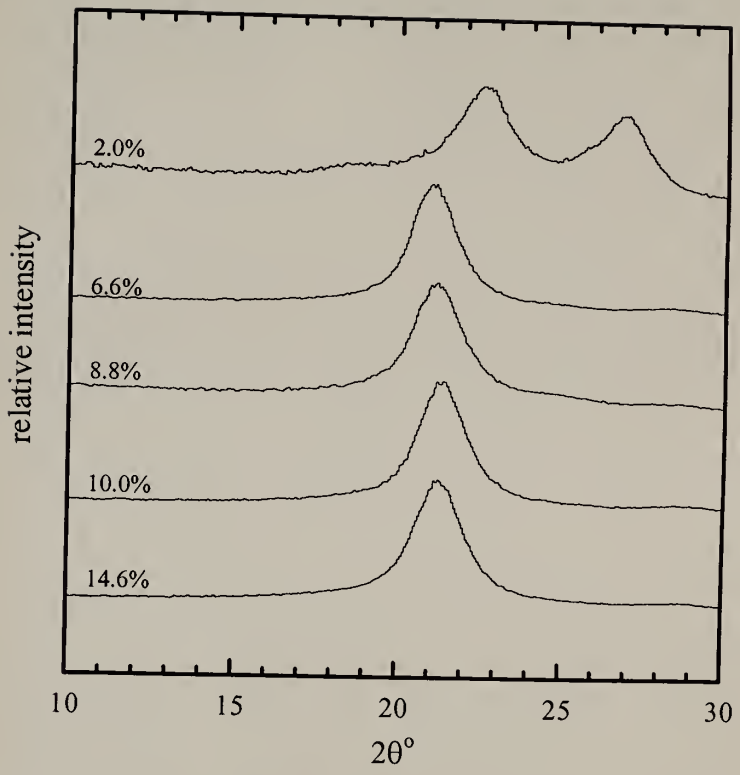

Figure 6.14: WAXD data plotted relative intensity versus 2θ for the drawn propyl substituted films with the beam parallel to the plane of the film.

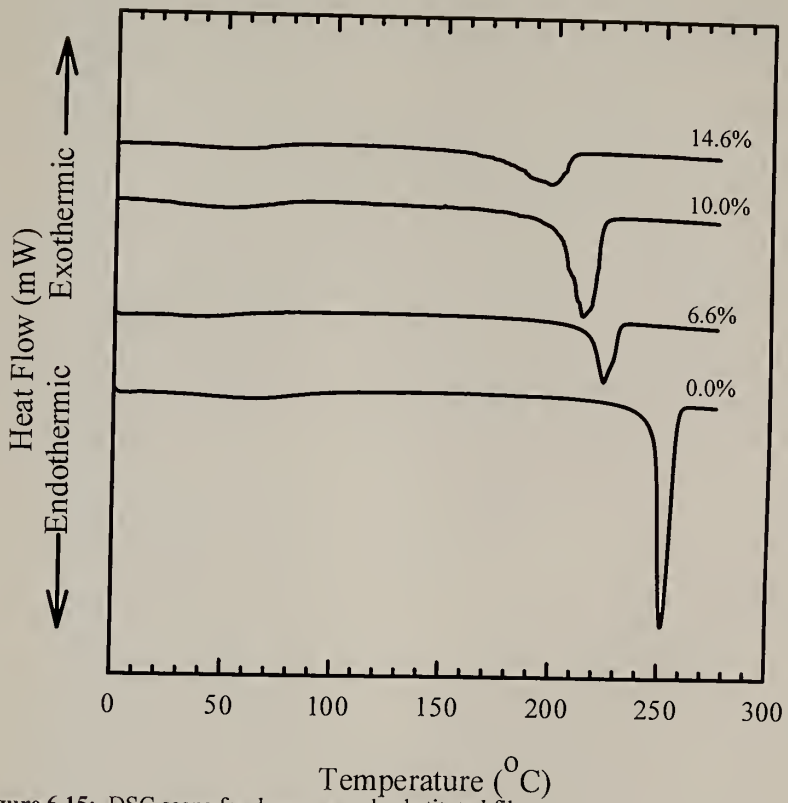

Figure 6.15: DSC scans for drawn propyl substituted films.

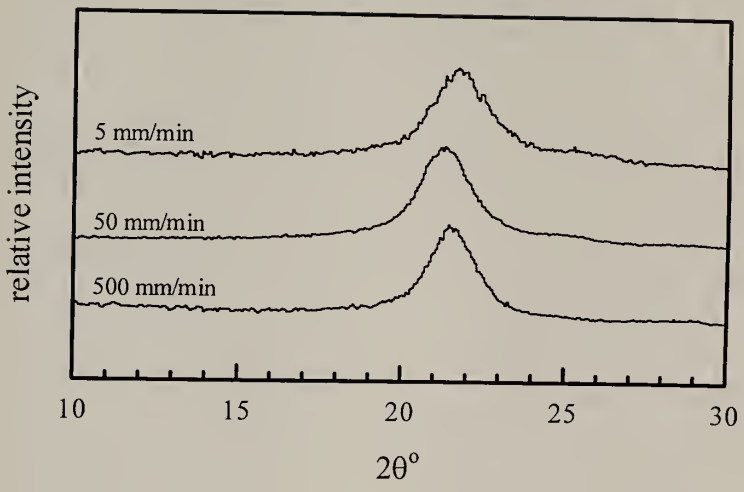

Figure 6.16: WAXD data plotted relative intensity versus 2θ for propyl substituted films drawn at various rates.

BIBLIOGRAPHY

1) Hopkins, I. L.; Baker, W. O.; Howard, J. B. *Journal of Applied Physics* **1950**, *21*, 206-213.

2) Miklowitz, J. *Journal of Colloid Science* **1947**, *2*, 217-222.

3) Miklowitz, J. *Journal of Colloid Science* **1947**, *2*, 193-215.

4) Sabbagh, A. B.; Lesser, A. J. *Journal of Polymer Science: Part B: Polymer Physics* **1999**, *37*, 2651-2663.

5) Bert, C. W.; Mayberry, B. L.; Ray, J. D. *ASTM Special Technical Publication* **1969**, *460*, 362-380.

6) Chen, A. S.; Matthews, F. L. *Composites* **1993**, *4*, 395-406.

7) Thorkildsen, R. L. *Mechanical Behavior*; Baer, E., Ed.; Van Norstrand Reinhold Company: New York, 1964, pp 277-399.

8) Sternstein, S. S.; Ongchin, L. *American Chemical Society, Polymer Preprints* **1969**, *10*, 1117-1124.

9) Carapellucci, L. M.; Yee, A. F. *Polymer Engineering and Science* **1986**, *26*, 920-930.

10) Kody, R. S.; Lesser, A. J. *Journal of Materials Science* **1997**, *32*, 5637-5643.

11) Lesser, A. J.; Kody, R. S. *Journal of Polymer Science: Part B: Polymer Physics* **1997**, *35*, 1611-1619.

12) Mitttal, R. K.; Singh, I. P. *Polymer Engineering and Science* **1982**, *22*, 358-364.

13) Tuttle, M. E.; Semeliss, M.; Wong, R. *Experimental Mechanics* **1992**, *March*, 1-10.

14) Bekhet, N. E.; Barton, D. C.; Craggs, G. *Journal of Materials Science* **1994**, *29*, 4953-4961.

15) Danforth, R. L.; Machado, J. M.; Jordaan, J. C. M. *Plastics Engineering* **1996**, *March*, 77-79.

16) Ash, C. E.; Waters, D. G.; Smaardijk, A. A. "Synthesis and Stability of Aliphatic Polyketones" presented at SPE ANTEC, **1995**, *2*, 2319-2325.

17) Danforth, R. L.; Machado, J. M.; Jordaan, J. C. M. "Development of A New Polymer Family of Thermoplastic Aliphatic Polyketones" presented at SPE ANTEC, **1995**, *2*, 2316-2318.

18) Ash, C. *Intern. J. Polymeric Mater.* **1994**, *30*, 1-13.

19) Ash, C. E.; Flood, J. E. *Polymeric Materials Science and Engineering* **1997**, *76*, 110-111.

20) Kelley, J. W.; Roane, D. R.; Le, D. M. "ETP Performance Ranking Methodology for Prototype-Assembly Testing in Gear Applications" presented at SPE ANTEC, **1995**, *3*, 3819-3825.

21) Waters, D.; van Veelen, A. *Aliphatic polyketones in Automotive Fuel Systems*, 1995; Vol. SC: 2303-95.

22) Del Nobile, M. A.; Mensitieri, G.; Sommazzi, A. *Polymer* **1995**, *36*, 4943-4950.

23) Garbassi, F.; Sommazzi, A. *Polymer News* **1994**, *20*, 201-205.

24) Weinkauf, D. H.; Kinneberg, P. A.; Ash, C. E. "The Chemical Resistance and Barrier Properties of Aliphatic Polyketones" presented at SPE ANTEC, **1995**, *2*, 2340-2344.

25) Sommazzi, A.; Garbassi, F. *Progress in Polymer Science* **1997**, *22*, 1547-1605.

26) Drent, E. : European, 1984; Vol. A2.

27) Drent, E. , 1989.

28) Drent, E.; van Broekhoven, J. A. M.; Doyle, M. J. *Journal of Organometallic Chemistry* **1991**, *417*, 235-251.

29) Drent, E.; Jager, W. W. *Efficient Synthesis of Aliphatic Polyketones by Copolymerization of Olefins and Carbon Monoxide Catalyzed by Cationic Palladium-chelate Ligand Complexes*, 1997; Vol. 76, pp 100-101.

30) Bonner, J. G.; Powell, A. K. *Polymeric Materials Science and Engineering* **1997**, *76*, 108-109.

31) Ashby, M. F. *Materials Selection in Mechanical Design*; Pergamon Press:, 1992.

32) Bekhet, N. E.; Barton, D. C.; Craggs, G. *Polymer Testing* **1993**, *12*, 401-414.

33) *Annual Book of ASTM Standards*, 1987; Vol. V08.01 D638-86.

34) Ting, T. C. T. *Anisotropic Elasticity Theory and Applications*; Oxford University Press: New york, 1996.

35) Caddell, R. M.; Raghava, R. S.; Atkins, A. G. *Journal of Materials Science* **1973**, *8*, 1641-1646.

36) Lindberg, H. E.; Florence, A. L. *Dynamic Pulse Buckling*; Martinus Nijhoff Publishers: Dordrecht, 1987.

37) Jones, N. A.; Lesser, A. J. *Journal of Polymer Science: Part B: Polymer Physics* **1998**, *37*, 3246-3255.

38) Govaert, L. E.; de Vries, P. J.; Fennis, P. J.; Nijenhuis, W. F.; Keustermans, J. P. *Polymer* **2000**, *41*, 1959-1962.

39) Kalay, G.; Bevis, M. J. *Journal of Polymer Science Part B: Polymer Physics* **1997**, *35*, 415-430.

40) Klop, E. A.; Lommerts, B. J.; Veurink, J.; Aerts, J.; Van Puijenbroek, R. R. *Journal of Polymer Science Part B: Polymer Physics* **1995**, *33*, 315-326.

41) Lagaron, J. M.; Vickers, M. E.; Powell, A. K.; Davidson, N. S. *Polymer* **2000**, *41*, 3011-3017.

42) Holt Jr., G. A.; Spruiell, J. E. "The Crystallization and Melting Behavior of Aliphatic Polyketones Using Differential Scanning Calorimetry (DSC)" presented at SPE ANTEC, **1996**, *2*, 1780-1788.

43) Hill, R. *Proceeedings of the Royal Society* **1948**, *A193*, 281-297.

45) Quinson, R.; Perez, J.; Rink, M.; Pavan, A. *Journal of Materials Science* **1997**, *32*, 1371-1379.

46) Hoffman, O. *Journal of Composite Materials* **1967**, *1*, 200-206.

47) Azzi, V. D.; Tsai, S. W. *Experimental Mechanics* **1965**, *September*, 283-288.

48) Tsai, S. W.; Wu, E. M. *Journal of Composite Materials* **1971**, *5*, 58-80.

49) Bridle, C.; Buckley, A.; Scanlan, J. *Journal of Materials Science* **1968**, *3*, 622-628.

50) Stassi-D'Alia, F. *Meccanica* **1969**, *4*, 349-370.

51) Robertson, R. E. *The Journal of Chemical Physics* **1966**, *44*, 3950-3956.

52) Argon, A. S. *Philosophical Magazine* **1973**, *28*, 839-865.

53) McCrum, N. G.; Buckley, C. P.; Bucknall, C. B. *Principles of Polymer Engineering*; Oxford Press:, 1989.

54) Caddell, R. M.; Raghava, R. S.; Atkins, A. G. *Materials Science and Engineering* **1974**, *13*, 113-120.

55) Raghava, R.; Caddell, R. M.; Yeh, G. S. Y. *Journal of Materials Science* **1973**, *8*, 225-232.

56) Mathew, B. A.; Nunn, R. E.; Orroth, S. A. *Polymeric Materials Science and Engineering* **1988**, *59*, 1212-1217.

57) Lagasse, R. R.; Maxwell, B. *Polymer Engineering and Science* **1976**, *16*, 189-199.

58) Greco, R.; Coppola, F. *Plastics and Rubber Processing and Applications* **1986**, *6*, 35-41.

59) Macauley, N. J.; Harkin-Jones, E. M. A.; Murphy, W. R. *Polymer Engineering and Science* **1998**, *38*, 662-673.

60) Ohlberg, S. M.; Roth, J.; Raff, R. A. V. *Journal of Applied Polymer Science* **1959**, *1*, 114-120.

61) Starkweather *Journal of Applied Polymer Science* **1959**, *1*, 236-239.

62) So, P.; Broutman, L. J. *Polymer Engineering and Science* **1976**, *16*, 785-791.

63) Broutman, L. J.; Krishnakumar, S. M. *Polymer Engineering and Science* **1976**, *16*, 74-81.

64) Gerlowski, E. L.; Kastelic, J. R. *Melt-processed Polyketone-based Barrier Polymer Materials*; Shell Oil Company: US, 1990.

65) Flood, J. E.; Weinkauf, D. H.; Londa, M. "Aliphatic Polyketone Thermal Properties and Polymer Morphology" presented at SPE ANTEC, **1995**, *2*, 2326-2334.

66) Lommerts, B. J.; Klop, E. A.; Aerts, J. *Journal of Polymer Science Part B: Polymer Physics* **1993**, *31*, 1319-1330.

67) Waddon, A. J.; Karttunen, N. R.; Lesser, A. J. *Macromolecules* **1999**, *32*, 423-428.

68) Shkrabo, D. M.; Zhizhin, G. N.; Kuzik, L. A.; Garbuzova, I. A. *Vibrational Spectroscopy* **1998**, *17*, 155-162.

69) Koenig, J. L. *Chapter 2*; American Chemical Society: Washington D.C., 1992.

70) Clutton, E. Q.; Wiliams, J. G. *Polymer Engineering and Science* **1995**, *35*, 1381-1386.

71) Holt, J., G.A.; Spruiell, J. E. *Polymeric Materials Science and Engineering* **1997**, *76*, 112-114.

72) Hendra, P. J.; Taylor, M. A.; Willis, H. A. *Journal of Polymer Science: Part C: Polymer Letters* **1986**, *24*, 83-85.

73) Chatani, Y.; Takizawa, T.; Murahashi, S.; Sakata, Y. *Journal of Polymer Science* **1961**, *55*, 811-819.

74) Waddon, A. J.; Karttunen, N. K. *Polymer* **2001**, *42*, 2039-2044.

75) Garbassi, F.; Sommazzi, A.; Meda, L.; Mestroni, G.; Sciutto, A. *Polymer* **1998**, *39*, 1503-1506.

76) Waddon, A. J.; Karttunen, N. R. *Macromolecules* **2000**.

77) Sanchez, I. C.; Eby, R. K. *Journal of Research of the National Bureau of Standards, Physics and Chemistry* **1973**, *77A*, 353-328.